

Dissertation

Universität Bremen

Fachbereich 1 - Physik

Institut für Umweltphysik

Solar Occultation Measurements with SCIAMACHY in the UV-visible-IR Wavelength Region

vorgelegt von Dipl.-Phys. Jérôme Meyer
zur Erlangung des Grades *doctor rerum naturalium*

Gutachter: Prof. Dr. J. Burrows
Prof. Dr. J. Bleck-Neuhaus

Tag des Kolloquiums: 26. Mai 2004

Bremen, Januar 2004

Contents

Introduction	iv
I Measuring the Sunlight	1
1 The Sun	3
1.1 Observing the Sun	3
1.1.1 Extraterrestrial Spectra	3
1.1.2 Measurements from SCIAMACHY	5
1.2 Solar Physics	8
1.3 Fraunhofer Lines	10
1.4 Inhomogeneities	11
1.4.1 Limb Darkening	11
1.4.2 Sun Spots	13
2 SCIAMACHY	15
2.1 About the Instrument	15
2.1.1 Satellite Orbit	15
2.1.2 The Spectrometer	17
2.2 Viewing Geometries	20
2.2.1 Occultation	20
2.2.2 Nadir and Limb	24
2.3 Other Instruments	25
2.3.1 ACE/MAESTRO	25

2.3.2	GOMOS	26
2.3.3	HALOE	27
2.3.4	ILAS	27
2.3.5	ORA	29
2.3.6	POAM	29
2.3.7	SAGE	29
3	Simulation of Measurements	33
3.1	Atmospheric Constitution	33
3.2	Transmission through the Atmosphere	37
3.2.1	Extinction Processes	37
3.2.2	Radiative Transfer Model	41
3.2.3	Modeled Spectra	42
3.3	Scattered Light	45
3.3.1	Background	45
3.3.2	Results	46
3.4	Retrieval Aspects	48
3.4.1	Signal-to-noise Ratio	48
3.4.2	Integration over the Field of View	49
3.4.3	Conclusions	51
II	Retrieval of Information about the Atmosphere	53
4	The Inverse Problem	55
4.1	The Optimal Estimation Method	56
4.2	The Eigenvector Decomposition	57
4.3	Application to Occultation	58
4.3.1	Formulations	58
4.3.2	Regularisation	61
4.3.3	Shift and Squeeze	62

5	Trace Gas Vertical Profiles	65
5.1	Retrieval Process	65
5.2	Ozone	67
5.2.1	Background	67
5.2.2	Retrieval Results	68
5.3	Nitrogen Dioxide	73
5.3.1	Background	73
5.3.2	Retrieval Results	74
5.4	Oxygen	76
5.4.1	Background	76
5.4.2	Retrieval Results	78
5.5	Carbon Dioxide	80
5.5.1	Background	80
5.5.2	Retrieval Results	80
6	Information on Geometry	83
6.1	Tangent Heights	83
6.1.1	First Approach to a Tangent Height Retrieval	84
6.1.2	Results	85
6.2	Pointing on the Solar Disk	86
6.2.1	Refraction	88
6.2.2	Sun Flattening	90
6.2.3	Matching Algorithm	92
6.2.4	Other Methods	94
7	Error Analysis	97
7.1	Spectral Errors	97
7.1.1	Spectral Inhomogeneities	97
7.1.2	Wavelength Shifts	98
7.2	Geolocation	103
7.2.1	Tangent Point Location	103

7.2.2	Line of Sight Geometry	103
7.2.3	Horizontal Inhomogeneities	105
7.3	Retrieval Errors	109
7.3.1	Statistical Errors	109
7.3.2	Validation Results	110
7.3.3	Error Budget	112
8	Conclusion and Outlook	117
8.1	Applications	117
8.2	Open Questions	119
8.2.1	Information from Scanning	119
8.2.2	Accuracy of Profile Retrieval	122
8.2.3	Extreme Tangent Heights	124
8.2.4	Retrieval of Temperature and Pressure	125
8.3	Outlook	126
8.3.1	Scanning or Pointing?	126
8.3.2	Occultation vs. Limb	127
8.4	Summary	128
8.5	Deutsche Zusammenfassung	130
A	Fraunhofer Lines	131
B	Cross Sections	135
C	Orbit Numbers	139
D	Solar Zenith Angle vs. Tangent Height	143
E	Retrieval Algorithm	147
	Glossary	149

Introduction

Motivation

For the first time in my life, I saw the horizon as a curved line. It was accentuated by a thin seam of dark blue light – our atmosphere. Obviously, this was not the ocean of air I had been told it was so many times in my life. I was terrified by its fragile appearance.

Ulf Merbold, German Astronaut

The atmospheric sciences have rapidly grown in the last two decades, partly as a result of an increased awareness of environmental issues as they affect the “air we breathe” and the accompanying increase in public funding. Research advances in the atmospheric sciences have been greatly facilitated by the simultaneous growth in computing power, with PCs becoming a vital tool in the analysis of complex environmental processes. The coverage of “complexity” is an important aspect of the atmospheric sciences per se, especially with regards to environmental monitoring from space.

Atmospheric monitoring from space is a rather young field of research within the atmospheric sciences, which arose out of the development of new remote measurement techniques suitable for spaceborne operation. These spectroscopic methods belong both to the most challenging and most expensive instruments. They deliver very large amounts of data to the satellite ground stations around the clock (an expected 1 Petabyte, i.e. 10^{15} bytes over five years in the case of ENVISAT*). However, these data cannot be expected to resolve but a small piece of the environmental puzzle. Nevertheless, it is the combination of these data with the knowledge of environmental physics and chemistry input into models that is hoped to make it possible to effectively reproduce nature on a computer system.

Spaceborne measurements are unique in their ability to provide global coverage of atmospheric parameters every few days, which makes them interesting for fur-

*ENVISAT stands for Environmental Satellite. It consists out of ten instruments dedicated to investigate atmosphere, oceans, and land surfaces. See also <http://envisat.esa.int>

ther applications. Forecasts, such as the weather forecast, were revolutionised by satellite data, and it is the newest satellite data that make them partially available for environmental issues such as the ozone hole or long-range atmospheric pollution, topics that have been discussed in the political arena for decades. The public is interested in the future living conditions on our planet, and scientists are actively seeking answers to the many open questions regarding atmospheric dynamics and chemistry that will strongly affect those conditions.

It is both daunting and fascinating at the same time to be part of this endeavour. Hopefully, the occultation measurements analysed in this work will contribute to some answers.

Aims of this Thesis

SCIAMACHY (**SC**anning **I**maging **A**bsorption spectro**M**eter for **A**tmospheric **CH**artograph**Y**) was launched in March 2002 onboard ENVISAT and has very extensive capabilities with many of scientific goals [Bovensmann et al., 1999]. Occultation measurements are a small but challenging part of it. The focus of this thesis is on basic solar occultation aspects, retrieval of trace gases, first results after the successful launch of ENVISAT, and the validation.

Spaceborne observations of atmospheric constituents have taken place since the 1970s [Heath et al., 1975, McCormick et al., 1979]. Ozone was the first scientific goal concerning atmospheric chemistry as it is easy to detect spectroscopically. After global observation of the ozone hole a few years later [Farman et al., 1985], stratospheric chemistry concerning the ozone destruction cycle is still a challenging task. Equally, the human impact on the troposphere can now be monitored by satellite instruments. Complexity of scientific questions and measurement capabilities have grown up to now in a breathtaking manner. Nowadays, there are approximately twenty atmospheric species and parameters to be observed by SCIAMACHY. Also occultation measurements have been performed with several spaceborne instruments since that time.

Occultation measurements are characterised by their special observation geometry detecting only the direct irradiation of the Sun or any other celestial body that is bright enough. Throughout this thesis, it will be shown how atmospheric parameters, especially trace gas profiles, can be derived from the spectroscopic data of SCIAMACHY. The final goal is the ability to provide height-resolved profiles of trace gas concentrations for further use in the community of atmospheric sciences.

In the first part of this thesis, the fundamentals for trace gas retrievals are

discussed. An introduction is given about the Sun as a light source in Chapter 1, the spectrometer in Chapter 2, and radiative transfer modeling in Chapter 3. The actual retrieval of trace gas concentrations from spectroscopic data and the underlying theory of inversion are treated in the second part. This partitioning reflects my time at the Institute of Environmental Physics beginning with theoretical studies and later lays the foundations for occultation evaluation after the launch of *SCIAMACHY*.

The theoretical foundations of inversion theory are discussed in Chapter 4. It is kept brief as the basic computer algorithms were already programmed by Alexei Rozanov [Rozanov, 2001]. The focus of my work was to improve the algorithms for real data application and to validate the first results, which can be found in Chapter 5. Since evaluation of occultation measurements is quite sensitive to geometrical issues, the reliability of geometry information was part of the investigations as described in Chapter 6.

Another important issue for any following scientific study is a detailed error analysis. The optimal estimation method used in the retrieval algorithms provides automatically some statistical error analysis. However, there are a lot of error sources that cannot be treated in this simple way. Therefore, a realistic description of precisions is an indispensable and troublesome task. It is discussed in Chapter 7. Chapter 8 gives a summary and some remarks about future work with solar occultation data. Lunar occultations, which are also part of *SCIAMACHY*'s measurement sequences, are left out completely although their evaluation is closely related to solar occultations.

Part I

Measuring the Sunlight

Chapter 1

The Sun

The Sun is not only at the centre of solar occultation measurements and the basis of this thesis. It is in fact the centre of our solar system and our life. The photo in Figure 1.1 was made at the end of the 1980s with a commercially available telescope and a reflex camera. Sun spots and limb darkening effect, which are discussed in this chapter, can easily be identified. So the difficulties of scientific solar measurements can even be understood using a simple piece of equipment. This chapter describes shortly the physical foundations of solar radiation and its appearance through SCIAMACHY's "eyes".

1.1 Observing the Sun

For solar occultation measurements, the Sun is directly used as a light source. One spectrum covering the range from 240–2400 nm is taken every 62.5 msec. Here begins the work after receiving data from ESA...

1.1.1 Extraterrestrial Spectra

In Figure 1.2, the extraterrestrial solar irradiance is plotted vs. wavelength. The underlying data are taken from a solar atlas provided by Kurucz et al. [1984]. It can clearly be seen that the solar spectrum is not a smooth curve as one would expect from the black body approximation. It is well supplied with several absorption lines on very small wavelength scales complicating the evaluation of occultation measurements (see Section 1.3).

In this thesis, irradiance is the main radiative quantity as only the direct sun-

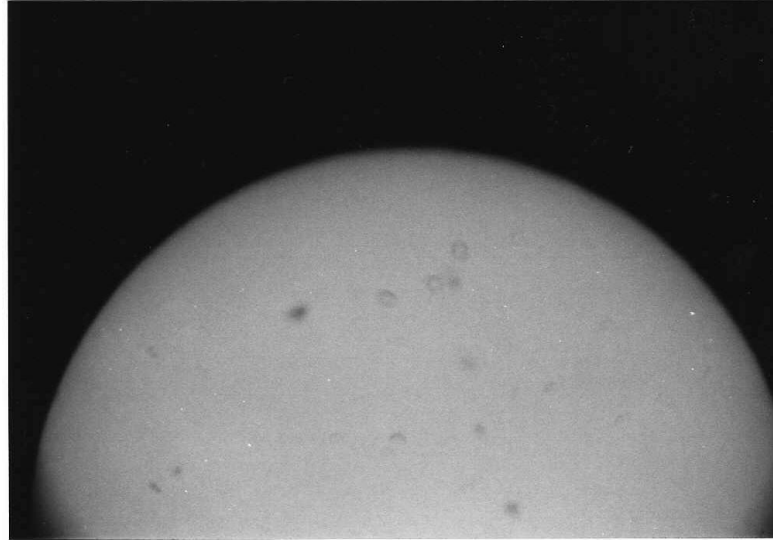


Figure 1.1: The Sun observed with a commercially available telescope.

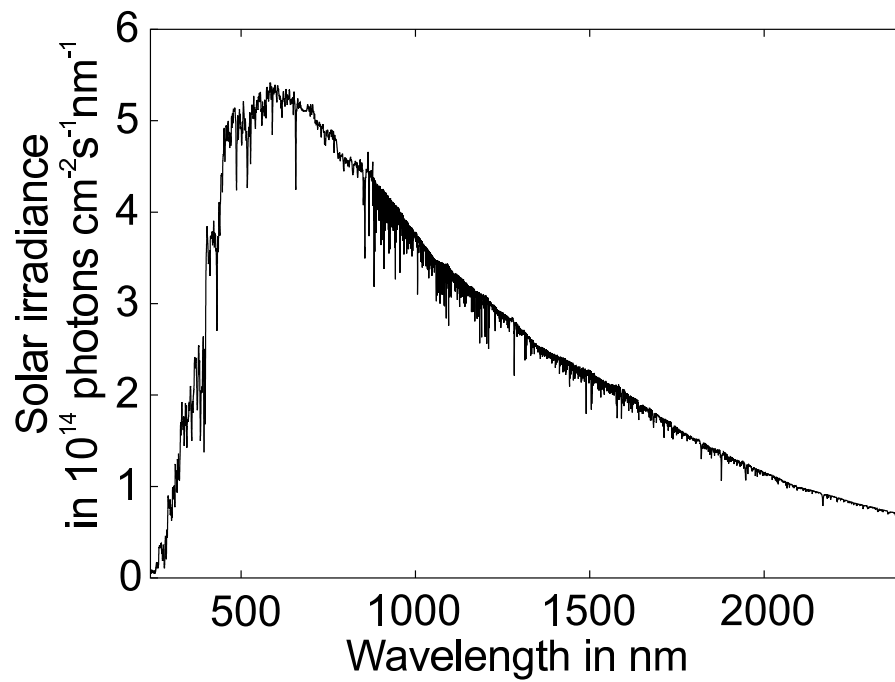


Figure 1.2: Extraterrestrial solar irradiance. Intensities are given in incident photons per cm^2 and per second for wavelength intervals of one nanometer [Kurucz et al., 1984].

light is investigated. In this sense, solid angle characteristics are neglected. Some other useful physical quantities and units for radiometric measurements are

$$\begin{aligned}
 \text{radiant flux or luminous power} & \quad \Phi = \frac{E_R}{t} && (\text{W}), \\
 \text{radiation intensity} & \quad I = \frac{\Phi}{A} && \left(\frac{\text{W}}{\text{cm}^2}\right), \\
 \text{and radiance} & \quad I_R = \frac{I}{\Omega} = \frac{E_R}{A\Omega t} && \left(\frac{\text{W}}{\text{sr}\cdot\text{cm}^2}\right)
 \end{aligned}
 \tag{1.1}$$

with total radiant energy E_R , time interval t , area A , and solid angle Ω . The radiative quantities are turned into specific quantities when their dependence on wavelength λ is considered. Irradiance is physically the same quantity as the radiation intensity. The term irradiance is mainly used for illuminated surface areas whereas other quantities are also applied to the emission of radiation.

It is convenient to use the number of incident photons per time or Watt as a unit for irradiance. In the case of specific irradiation $I(\lambda)$, both units are equivalent, as photons within a small wavelength interval $\Delta\lambda$ have a well defined energy.

1.1.2 Measurements from SCIAMACHY

As will be discussed in Chapter 2, SCIAMACHY occultation measurements are performed permanently during sunrise with a spectral resolution of less than 1 nm. Consecutive measurements produce complete scanning images of the Sun as can be seen in Figure 1.3. In most cases, the measurement sequences continue to regions

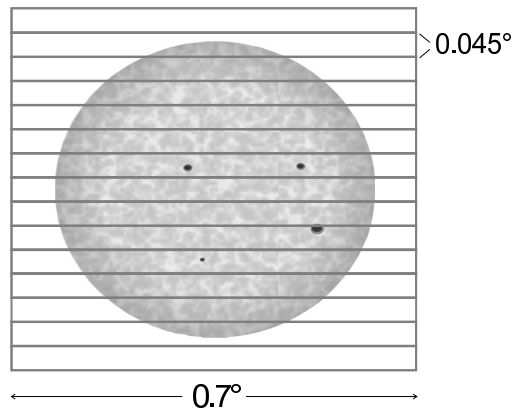


Figure 1.3: Schematic illustration of a typical occultation scan image of the Sun as performed by SCIAMACHY. The rectangular boxes indicate SCIAMACHY's field of view.

far above any atmospheric influence. Such measurements are used as reference

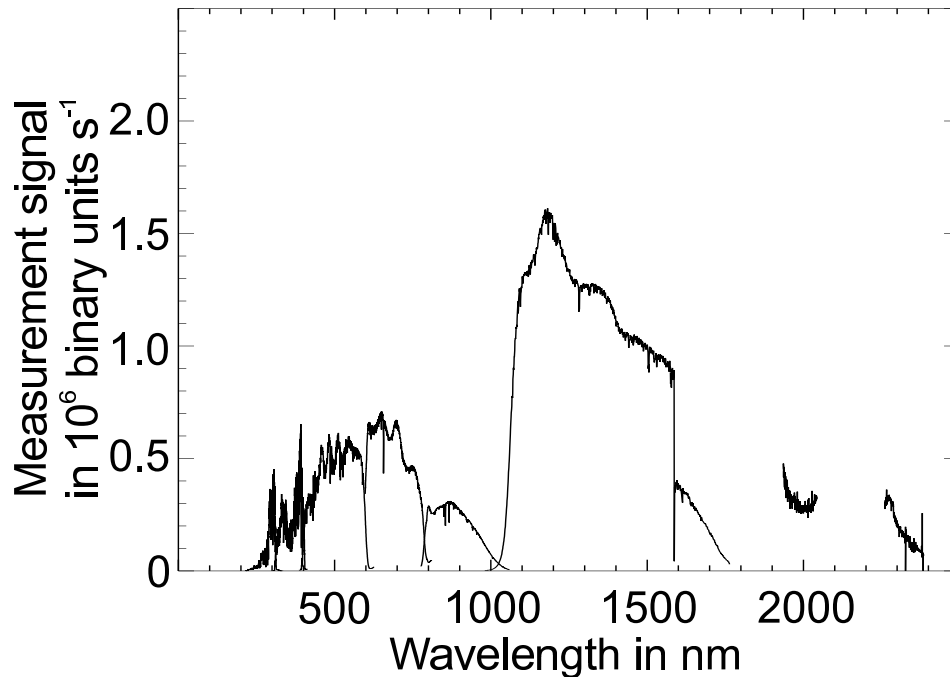


Figure 1.4: SCIAMACHY solar occultation measurement above the atmosphere on September 25, 2002, 16:29 UTC. Intensities are given in binary units.

spectra to calculate transmissions from atmospheric measurements. Figure 1.4 shows a typical extraterrestrial measurement over the whole spectral region of SCIAMACHY. Intensities are given in binary units as the data have been taken from uncalibrated so-called level-0 data products. Level-0 is the first data processing step after data transmission to the ground segments [Lützw-Wentzky and Demuth, 2001]. Binary units reflect directly the engineering data received from SCIAMACHY. Originally, wavelengths are given in pixel* numbers in the uncalibrated level-0 data. Here, they have already been replaced by corresponding wavelengths. The wavelength calibration used for this work was performed before ENVISAT's launch. In flight corrections are still missing. Comparing Figures 1.4 and 1.2, it can clearly be seen that each of the eight spectral channels of SCIAMACHY has different spectral properties (see Section 2.1.2). Absolute differences in binary units can also be explained by different measurement integration times. Integration times can be modified for certain clusters, i.e. wavelength ranges. Furthermore, the channels have some overlap with the exception of infrared channels 7 and 8. In channel 6, two different types of detector materials are used. The boundary can be seen around 1590 nm.

*SCIAMACHY's wavelength range is divided into eight channels, each containing 1024 wavelength pixels. See Section 2.1.2.

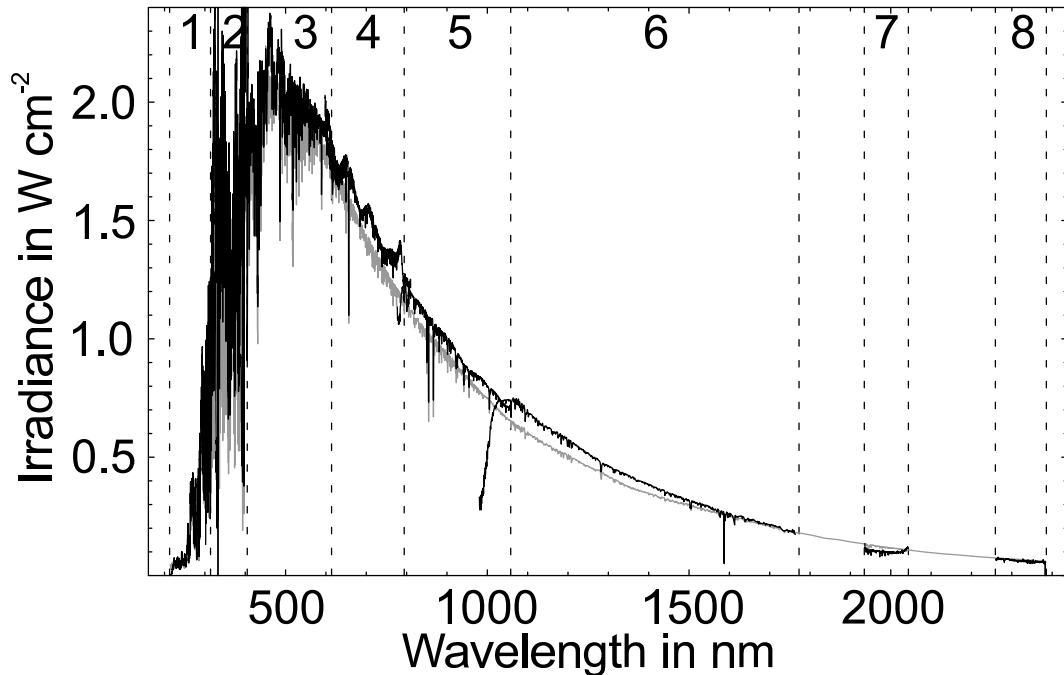


Figure 1.5: Black line: Calibrated solar spectrum obtained from an extraterrestrial SCIAMACHY occultation measurement [Skupin, 2003]. Grey line: Spectrum obtained from high resolution ground based measurements [Kurucz et al., 1984]. SCIAMACHY wavelength channels are indicated by the vertical dotted lines and their numbers.

Calibrated spectra are obtained after the so-called Level-0 to 1c data processing [Slijkhuis and Balzer, 2000], where all kinds of calibration steps are performed (see Section 5.1). In Figure 1.5, a calibrated measurement spectrum from SCIAMACHY (black line) is shown in comparison with the high resolution spectrum measured by Kurucz et al. [1984] (grey line). Although the SCIAMACHY data processing is still to be improved, the general agreement is already quite good. A little offset can be observed, which is 8 % on average [Skupin, 2003]. Channels 7 and 8 show some exceptional behaviour. The infrared detectors have to be cooled. Thus, any water vapour carried within the satellite condenses on the detectors. The measured intensities are reduced complicating the calibration. The slight oscillations – especially in channel 4 – are due to the so-called etalon effect. The etalon effect is caused by interferences on non-perfect or contaminated optical devices. In the UV wavelength range, the deviations between the two spectra are particularly high as there are strong peaks with spatial and temporal dependencies.

So far, an absolute calibration is not necessarily needed in any event. The evaluation of solar occultation measurements introduced in this thesis is based

on the model fit of atmospheric transmissions, which are always relative to an extraterrestrial spectrum.

1.2 Solar Physics

This section gives a short overview of the physical processes that lead to the observed characteristics in the solar spectra. Most background information has been taken from [Demtröder, 1998].

The Sun is a fixed star with an effective surface temperature of 5770 K. It is a result of extremely high temperatures in the sun core and radiative exchange between the surface and the rest of the universe. The Sun is mainly composed of hydrogen ($\sim 90\%$) and helium ($\sim 10\%$). In a first approach, the solar radiation is characterised by a black body radiator. Size, mass, temperature, and luminous power of the Sun are assumed to be roughly constant on large time scales of roughly billions of years, whereas inhomogeneities on small time scales between minutes and decades have significant influence on solar occultation measurements.

Integration of the curve in Figure 1.2 leads to the total extraterrestrial irradiance

$$I_0 = 1.36 \text{ W} \cdot \text{m}^{-2}. \quad (1.2)$$

It is also known as the solar constant, which is used in many applications. The luminous power of the Sun L_\odot is $3.82 \cdot 10^{26} \text{ W}$. It can be calculated from the solar constant I_0 and the distance to the Sun r by

$$L_\odot = 4\pi r^2 I_0. \quad (1.3)$$

r is 149 million kilometers or one astronomical unit. According to the Stefan-Boltzmann Law, the radiation power of a black body with $A = 4\pi R_\odot^2$ denoting the surface and R_\odot the Sun's radius is also given by

$$L_\odot = 4\pi R_\odot^2 \sigma T^4, \quad (1.4)$$

where σ is the Stefan-Boltzmann Constant and T represents the effective black body temperature of approximately 5770 K. By means of simple assumptions about the Sun's gravitational energy, the core temperature is estimated to be $2.5 \cdot 10^6 \text{ K}$. Since there must be a large radial temperature gradient, more sophisticated models predict core temperatures of more than 10^7 K .

Since the Sun has been emitting almost constant huge amounts of energy for billions of years, there must be a very potent source of energy. Chemical reactions are not possible as those temperatures lead to a pure plasma consisting of

electrons and nucleons. Only nuclear power appears to be sufficient. The main process within the Sun is based on fusion of protons p to helium cores ${}^4_2\text{He}$ via the production of heavy hydrogen ${}^2_1\text{D}$, positrons e^+ , and neutrinos ν_e :



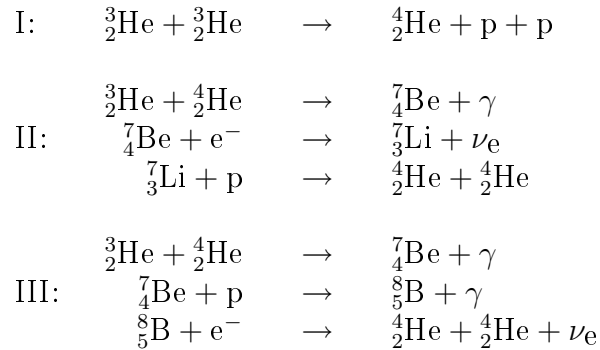
or alternatively as a three-body-reaction with an electron e^- as educt, instead of a positron among the products



The next interim product is ${}^3_2\text{He}$ and high energy photons γ after further reaction with a third proton:



Then, ${}^4_2\text{He}$ can be produced via three different channels:



Other cycles that produce heavier nuclides such as carbon, nitrogen, or oxygen, are not relevant for the Sun. The nuclear fusion takes place within a sphere of radius $r = 0.5R_\odot$. In the range $0.5R_\odot < r < 0.84R_\odot$, the produced energy is transported by radiative transfer. Electrons, γ -rays, and positively charged nuclids are interacting via the Compton Effect, bremsstrahlung, pair production, and annihilation. It is a continuous exchange of energy between photons and electrons. It takes roughly 10^7 years until the energy is transported to the surface. For $0.84R_\odot < r < 0.98R_\odot$, heat convection becomes the relevant process of energy transport. The sunlight observed from outside is produced in a thin layer, the so-called photosphere. It describes the visible sharp boundary of the solar disk. The radiation, which is the basis of occultation measurements, is produced by recombination of electrons with H-atoms to H^- ions and bremsstrahlung by interaction of electrons and protons. Recombination to neutral H-atoms is negligible as the average temperature is roughly 6000 K and thus the fraction of free ionised H-atoms is only around 10^{-4} .

Finally, the Sun is completed by the chromosphere (up to 10,000 km above the surface) and the corona. Though the latter can extend to more than one million kilometers into space and reaches temperatures of up to 10^6 K, both are not relevant for radiative emissions as their density decreases exponentially with height above the photosphere.

1.3 Fraunhofer Lines

As a result of the radiative emissions discussed in Section 1.2, a broad continuous spectrum can be observed (see Section 1.1). Investigating the spectrum with a higher resolution, many dark spots occur at distinct wavelengths. Joseph von Fraunhofer (1787–1826) was the first who registered more than 500 of these absorption lines. In his honour, they are called Fraunhofer lines. They originate from absorption within the photosphere. Since the Sun also contains traces of several elements beside hydrogen and helium, the whole solar spectrum is well supplied with Fraunhofer lines.

In regard to occultation measurements, it is important to know the spatial and temporal behaviour of the Fraunhofer lines. At first sight, all solar absorption lines should vanish in the retrieval process as all measurements are divided by a reference spectrum from above the atmosphere. However, taking into account that the solar disk is not a homogeneous source of light, spatially and temporally variable Fraunhofer lines have a significant impact on transmission spectra as well as on measurement evaluation. The most abundant elements of the Sun are summarised in Table 1.1.

Hydrogen	1.0	Magnesium	$2.3 \cdot 10^{-5}$
Helium	0.1	Iron	$3.0 \cdot 10^{-6}$
Oxygen	$1.0 \cdot 10^{-3}$	Sodium	$2.0 \cdot 10^{-6}$
Carbon	$5.2 \cdot 10^{-4}$	Calcium	$1.4 \cdot 10^{-6}$
Nitrogen	$1.0 \cdot 10^{-4}$	Nickel	$8.3 \cdot 10^{-7}$
Silicon	$2.8 \cdot 10^{-5}$	Chromium	$2.3 \cdot 10^{-7}$

Table 1.1: Solar elements and their relative abundance compared to hydrogen. Values have been taken from [Demtröder, 1998].

The reduction of radiative intensity I_0 at a given wavelength λ by these elements is ruled by the Lambert-Beer Law of extinction:

$$I(\lambda) = I_0(\lambda) \cdot \exp\left(-\int_{s_0}^{s_1} \alpha(\lambda, s) ds\right). \quad (1.8)$$

α is the absorption coefficient and $s_1 - s_0$ the considered path length within the photosphere. This is quite similar to absorption processes in the Earth's atmosphere, which will be discussed in more detail in Section 3.2.

A detailed list of important Fraunhofer lines in the SCIAMACHY wavelength range can be found in Appendix A.

1.4 Inhomogeneities

Many difficulties in the evaluation of solar occultation measurements arise from the Sun itself. It is e.g. not possible to determine the exact scanning position on the solar disk (see Figure 1.3). Therefore, no measurement can be divided by an exact counterpart of the reference scan, resulting in rest structures in transmission spectra. The structures are caused by inhomogeneities of the solar disk. One has to distinguish between spatial and temporal inhomogeneities and between broad band effects and impacts on the differential structure of a spectrum.

1.4.1 Limb Darkening

The limb darkening is a general reduction of intensity at the limb of the solar disk. Shorter wavelengths are more reduced than longer wavelengths. Furthermore, single Fraunhofer lines are affected differently depending on the characteristic height distribution of the corresponding absorber within the photosphere. The limb darkening can be explained by the fact that, as mentioned above, the observable radiation is only produced in the thin photosphere. Thus, radiation emitted from the solar limb passes a geometrically longer way through the photosphere. Due to strong absorption, the light is then reduced and radiation coming from deeper and hotter regions cannot escape. Radiation from the solar disk centre has shorter paths through the photosphere. Here, light rays from deeper regions are more likely to escape and thus total radiation seems to be emitted from a hotter black body radiator.

According to van Rie [1995], a general function describing the limb darkening of intensity $I_\lambda(\theta)$ compared to the centre intensity $I_\lambda(0)$ is given by

$$\frac{I_\lambda(\theta)}{I_\lambda(0)} = 1 - u_\lambda - \nu_\lambda + u_\lambda \cos(\theta) + \nu_\lambda \cos^2(\theta), \quad (1.9)$$

where θ denotes a polar angle within a sun-centred coordinate system and $\theta = 0$ describes the line of sight pointing directly into the Sun's centre. u_λ and ν_λ are wavelength dependent coefficients.

The impact of variable Fraunhofer lines is illustrated in Figure 1.6. Measurements

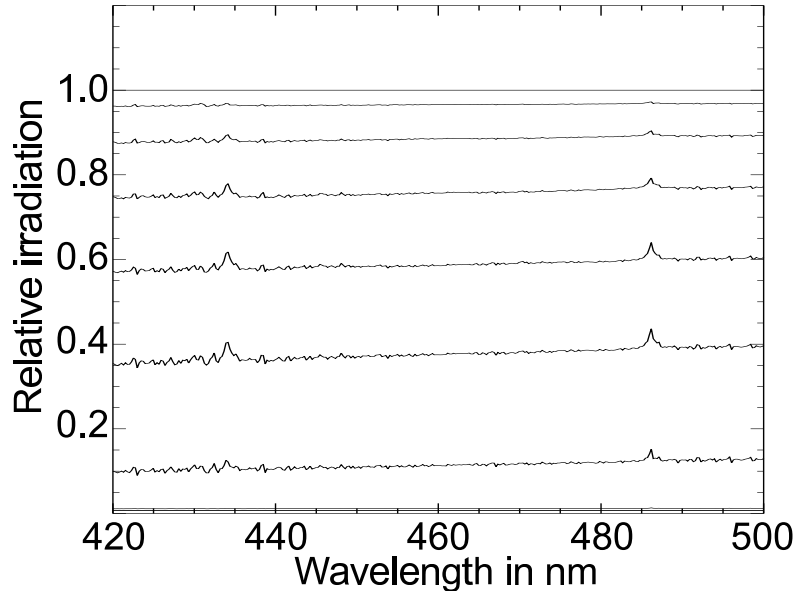


Figure 1.6: Extraterrestrial solar spectra measured by SCIAMACHY divided by a measurement pointing to the solar disk centre. All spectra were taken from the same occultation scan above the atmosphere, which is assumed to be 100 km high.

of an extraterrestrial sun scan are shown in this plot. The measurements have been divided by the brightest measurement of the same sequence, which is close to the centre of the solar disk. Taking only geometrical effects into account, the relative spectra should decrease towards the solar limb, each with a constant factor. Even the general limb darkening explained above has only a weak wavelength dependence, which would result in a smooth curve with a small slope. However, there are certain peaks corresponding to major Fraunhofer lines. Furthermore, the Fraunhofer lines show different behaviour towards the solar limb. This can be explained by the vertical concentration profiles of the different absorbing elements within the photosphere. Taking Equation 1.8 into account, it is clear from the discussion above that the behaviour of Fraunhofer lines is quite complex.

In the solar physics community, the line shape of Fraunhofer lines is even used for calculation of vertical profiles of the corresponding elements. SCIAMACHY measurements can also be interesting for studies on the spectral inhomogeneities as it has already been demonstrated with the HALOE[†] instrument [Spickler et al., 1996], which is also dedicated to occultation measurements. There are only a few instruments that are capable of measuring extraterrestrial solar spectra.

[†]HALOE stands for HALogen Occultation Experiment, see Section 2.3.3 for details

For solar occultation measurements with *SCIAMACHY*, it is important to notice that general limb darkening combined with geometrical effects are important for absolute calibration of irradiation. This is needed e.g. for retrieval of aerosol properties. Single Fraunhofer lines affect additionally the differential structure of measured spectra, which is of significance for trace gas retrieval. In [van Rie, 1995], deviations on the measured irradiance are estimated to an order of approximately 7% for a worst case scenario of a wrong pointing on the solar disk. Of course, single measurements are affected very differently. Measurements close to the solar centre have very similar limb darkening characteristics with relatively small impact whereas measurements close to the solar limb are much more strongly affected with a high sensitivity to the field of view pointing.

1.4.2 Sun Spots

The Sun shows a lot of interesting and sometimes spectacular phenomena, which can even influence the Earth's atmosphere. They are mostly the result of dynamic processes beneath the surface and vary on several time scales. The sun spots can be observed relatively easily e.g. with small telescopes. Hence, they were already observed by Galilei in the 16th century. The spots consist of a very dark central region, the so-called umbra, surrounded by the less dark penumbra, altogether with an average diameter of approximately 10,000 km or roughly one diameter of the Earth. The reason for the dark appearance is a lower temperature of roughly 1,500 K below the temperature of the surrounding photosphere. It is characterised by local radial magnetic fields penetrating the Sun's surface. Therefore, hot plasma convecting to the surface is turned away tangentially, leaving colder plasma at the surface.

Sun spots occur mainly in groups with corresponding spot groups northerly and southerly of the Sun's equator. The probability for their occurrence depends on solar latitude and the solar cycle. Small spots have a life time of a few days, whereas the larger spots live for up to one hundred days corresponding to roughly four rotations of the Sun. So they seem to "walk" around the Sun within some weeks. The total number of sun spots during a minimum of solar activity varies roughly between zero and fifty on a timescale of a few weeks. During a maximum of solar activity, the variation is between 150 and 250 spots. The time constant of the solar cycle is approximately eleven years. The last solar maximum was in the year 2000. The average latitudinal distribution of sun spots is given in Table 1.2 in terms of relative numbers. The sun spots concentrate on small gaps between 5° and 40° latitude on both southern and northern hemisphere.

Occultation measurements are affected by the occurrence of sun spots as *SCIAMACHY*'s field of view (see Section 2.1.2) focusses on small stripes of the apparent

Solar latitude	5°	10°	15°	20°	25°	30°	35°	40°
Weight factor	0	4	8	10	10	8	4	0

Table 1.2: Relative latitudinal distribution of sun spots in 5° intervals for both hemispheres. The values have been taken from [van Rie, 1995].

solar disk. The Sun’s equator plane makes an angle of only 7° with the ecliptic. Therefore, SCIAMACHY’s field of view is nearly parallel to those gaps with high probability of sun spot occurrence throughout the year. As a result, measurements adjacent to the Sun’s centre might show strongly reduced intensities during a solar maximum.

Since reduction of intensity by sun spots is due to smaller black body temperatures, shorter wavelengths are more affected than longer wavelengths, according to Planck’s Law of radiation. However, the wavelength dependence is quite weak on small wavelength scales. Assuming a maximum number of 250 sun spots, deviations in the total irradiance of the whole solar disk are 9.9 % and 3.3 % for wavelength channels 1 and 8, respectively. Due to the special field of view geometry, errors may increase even more for distinct measurements. More details can be found in [van Rie, 1995].

As discussed in this thesis, retrieval of trace gas concentrations are only affected by inhomogeneities with variations on small wavelength scales such as the Fraunhofer lines. Nevertheless, an impact of sun spots and global limb darkening is possible whenever an absolute spectral calibration is required for the evaluation of occultation measurements such as in the case of aerosols.

Chapter 2

SCIAMACHY

SCIAMACHY (**SC**anning **I**maging **A**bsorption spectro**M**eter for **A**tmospheric **CH**artograph**Y**) was proposed by an international team of scientists led by John Burrows [Burrows et al., 1988]. It was launched in Kourou, French Guiana, on March 1, 2002 into a sun-synchronous orbit 800 km above the Earth. It allows combining absorption spectroscopy with a global coverage of measurements in three viewing geometries. SCIAMACHY is one out of ten instruments onboard ENVISAT (Environmental Satellite). Altogether, they cover a spectral range from 200 nm to 10 cm in different spectral windows. The instruments are investigating the oceans, the atmosphere, and land surfaces.

This chapter gives a brief introduction of important spectral and orbital properties of the instrument as well as a discussion of the viewing geometries. Finally, an overview of recent occultation projects comparable to SCIAMACHY will be discussed.

2.1 About the Instrument

2.1.1 Satellite Orbit

Most spaceborne remote sensors are so-called low Earth orbiting satellites (LEO). The distance between sensor and region of interest is significant to the spatial resolution. So there is a need for orbits as low as possible, whereas too small altitudes lead to problems due to friction with the outer atmosphere. In Section 2.3, it can be seen that the height above ground is roughly between 500 and 1000 km for all occultation instruments. SCIAMACHY has a mean altitude of 799.8 km leading to an orbit period of 100.59 min or approximately 14 orbits per day. Main

characteristics are illustrated in Figure 2.1.

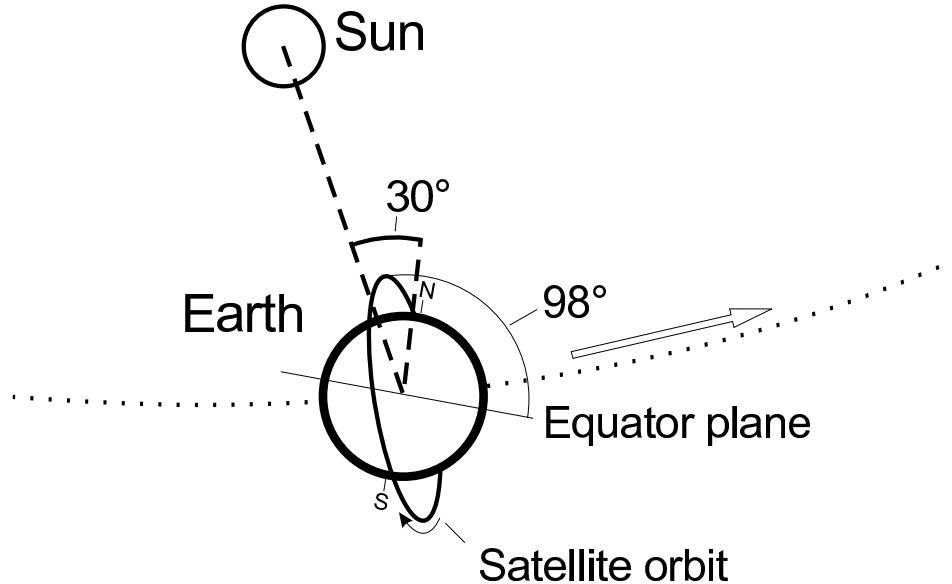


Figure 2.1: ENVISAT's orbit with respect to the Sun and the Earth's orbit.

The orbit is sun-synchronous, i.e. the local time where SCIAMACHY passes the equator is always 10 o'clock. Furthermore, this means that the orbit rotates once a year around a virtual axis perpendicular to the Earth's orbit plane. The driving force behind it is a small deviation of the Earth and its gravitational field from the shape of an ideal globe. Due to its own rotation, the Earth is flattened to an ellipsoid with the smallest diameter at the poles. Correspondingly, the gravitational force has a maximum around the equator and a minimum at the poles. Therefore, it is necessary to find an appropriate inclination angle for the satellite orbit in order to ensure a sun-synchronous orbit. An orbit inclination of 0° means rotation above the equator in the direction of the Earth's rotation, 90° is rotation over the poles with sunrise over the North Pole, and an inclination of 180° is rotation above the equator contrary to the movement of the Earth's surface. The inclination angle for a sun-synchronous orbit is then a trade off with the orbit altitude. SCIAMACHY has an inclination of 98.55° moving always a little bit against the Earth's rotation and passing close to the poles. A polar orbit with inclination angles around 90° or 270° provides good global coverage. In the case of SCIAMACHY measurements, a complete coverage is reached within six days. The orbit has a repeat cycle of 35 days with respect to the position above the Earth's surface. A sun-synchronous orbit is only possible due to the special gravitational field of the Earth. In fact it is a fortunate coincidence that the Earth's flattening allows for a sun-synchronous, polar, and low orbit.

In the context of this thesis, solar occultation events with the rising Sun are of particular interest. They take place whenever *SCIAMACHY* is leaving the Earth's shadow occurring always in the northern hemisphere. Due to the sun-synchronised orbit, the geolocation of the investigated air parcels is limited to a certain latitude region only with some seasonal variation throughout the year (see Section 2.2.1). On the other hand, performing all the measurements under the same conditions with the same local time makes the results more comparable.

2.1.2 The Spectrometer

SCIAMACHY is a passive remote sensing moderate-resolution imaging spectrometer. It covers a wavelength range from the ultraviolet to the near infrared. The spectral range is divided into eight channels each with 1024 wavelength pixels (Table 2.1). The detectors of channels 1–5 are based on silicon diode arrays, whereas the infrared detectors consist of various InGaAs alloys. The detector response to incident photons is a small output charge, which is amplified and converted into binary units by the electronic equipment. Due to the different viewing modes (see

Channel	Wavelength [nm]	Resolution [nm]
1	240–314	0.24
2	309–405	0.26
3	394–620	0.44
4	604–805	0.48
5	785–1050	0.54
6	1000–1750	1.48
7	1940–2040	0.22
8	2265–2380	0.26

Table 2.1: Wavelengths and resolutions for the spectral channels of *SCIAMACHY*.

Section 2.2), the optical bench contains a lot of mirrors, gratings, etc. and of course detectors allowing for several different light paths and measurement modes. A detailed overview of all important spectral properties can be found in [Bovensmann et al., 1999]. In the context of occultation measurements, the pointing mechanism and the effective field of view are the major keys to understanding this challenging measurement mode.

Field of View

SCIAMACHY's field of view (FOV) is determined by the path lengths within the instrument and the dimensions of the optical devices. The instrument design is optimised for limb and nadir measurements where the FOV is 1.8° along the width and 0.045° along the height. Due to the high intensities of the direct sunlight in occultation geometry, the incident radiation is reduced by an aperture stop and a neutral density filter. After all, the instantaneous FOV for solar occultation measurements is reduced to 0.7° along the width and 0.045° along the height. Hence, it is a bit wider than the apparent diameter of the Sun which is 0.53° . Considering simple geometric relations, the spatial resolution in the region of interest can be calculated from the instantaneous FOV and the distance to the spectrometer (see Equation 2.6). At the tangent point, the spatial resolution is approximately 30 km horizontally and 2.5 km vertically assuming only the solar disk to be the decisive source of light. The exact resolution varies a bit with tangent height. The wavelength resolution is also affected by the properties of the entrance slit. A detector pixel corresponds always to a distribution of wavelengths rather than a distinct wavelength. It can be described by a so-called slit function. Different types of functions were tested for approximation of the slit function. Naturally, they have similar gaussian-like appearance. With λ_0 denoting the centre wavelength of a detector pixel and $a(\lambda)$ the detector response at wavelength λ , the gaussian slit function is given by

$$a(\lambda) = c_1 \cdot e^{-\left(\frac{\lambda_0 - \lambda}{c_2}\right)^2} + c_3, \quad (2.1)$$

the simple hyperbolic approximation is

$$a(\lambda) = \frac{c_1^2}{c_2^2 + (\lambda_0 - c_3)^4} + c_4, \quad (2.2)$$

and the compound hyperbolic function can be written as

$$a(\lambda) = \frac{c_1^2}{c_2^2 + (\lambda_0 - c_3)^2} + \frac{c_1^4}{c_2^2 + (\lambda_0 - c_3)^4} + c_5. \quad (2.3)$$

The constants c_i represent free parameters of the specific fit. The additive constant in each equation reflects e.g. electronic offsets such as dark current. It should be removed by a good data processing. Best fitting results were obtained by a simple hyperbolic function. Only the slit functions of channels 6 and 8 are recommended to be fitted by gaussian and compound hyperbolic functions, respectively [Ahlers and Dobber, 2000]. For retrieval purposes, it is important to know the optimal fitting function and its full width half maximum (FWHM). The FWHM is determined by c_2 in Equations 2.2 and 2.3. In the case of the gaussian fit, it is given by $2c_2\sqrt{\ln 2}$. Since the differences between the approximations are small and are assumed to

have no significant influence on trace gas retrieval, the gaussian function was used throughout this work.

Pointing

The FOV pointing is determined by two mirrors for azimuth and elevation movement. They correspond with the horizontal and vertical direction in the region of interest. Since the relevant part of the atmosphere seen from SCIAMACHY has an apparent height of approximately 1.5° and the Sun an apparent diameter of only 0.53° , it is important for a successful measurement sequence to ensure a precise alignment of both mirrors. Usually, the Sun is scanned up and down during the whole sequence performing one measurement every 62.5 ms, the so-called integration time. The integration time corresponds with the pixel exposure time (PET) of the detectors. In channels 6 and 7, the PET is only 31.25 ms. One complete scan (up and down) takes four seconds corresponding to a scanning speed of $0.33^\circ/\text{s}$. A complete scanning sequence is shown in Figure 2.2. During an integration time

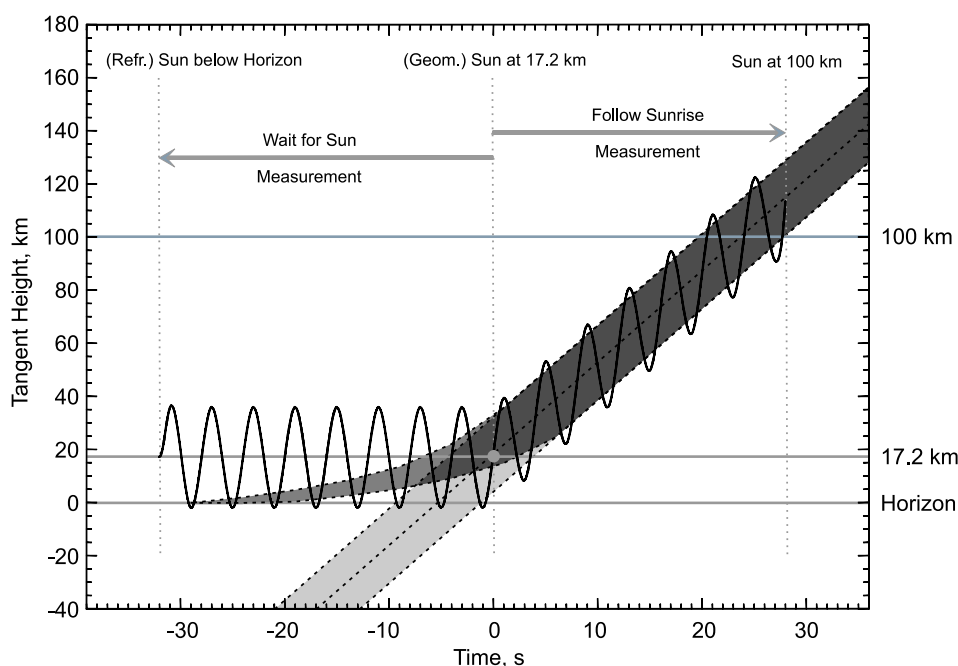


Figure 2.2: Schematic view of a solar occultation measurement sequence (state 47) as performed by SCIAMACHY. Tangent height in km is plotted vs. time in seconds. The solid line represents the movement of SCIAMACHY's FOV, the shaded areas illustrate the refracted and the imaginary true Sun, respectively [Noel, 2003].

of 62.5 ms, the FOV moves by 0.02° or nearly half of its own vertical dimension

reducing the vertical resolution by a factor of 1.46. Since the scanning speed is approximately five times higher than the elevation rate of the rising Sun, the latter one can be neglected in this context.

The scanning sequence can be divided into two parts: waiting for the Sun and following the Sun. On the basis of precalculated orbital parameters, SCIAMACHY begins to scan the estimated sunrise region shortly above the horizon. When the centre of the geometric Sun reaches a tangent height of 17.2 km (at 0 seconds in Figure 2.2), a sun-follower device adjusts the FOV to the apparent Sun in azimuthal (i.e. horizontal) direction. The FOV is then moved with a precalculated elevation rate additionally to the scanning movement. After a total of 16 complete scans or 64 seconds, the tangent height is approximately 100 km. Here, the line of sight is adjusted also vertically to the brightest point of the solar disk. Now there are two different endings of the occultation sequence that are regularly performed. One ends at a tangent height of 100 km pointing on the Sun's centre. In engineering nomenclature, this sequence is referred to as 'state 47'. The second one, 'state 49', is continued with the scanning sequence up to a tangent height of 300 km performing 24 additional complete scans. It takes roughly one and a half minutes of extra time. A third possibility, which was also performed successfully during the testing phase in orbit, is an extended pointing mode, where the pointing on the brightest area of the solar disk starts already after the adjustment at 17.2 km and continues to 100 km without any scanning movement. It does not belong to the so-called 'nominal states' that are performed regularly.

2.2 Viewing Geometries

SCIAMACHY is the first spaceborne instrument that is capable of performing three different viewing geometries: nadir, limb, and occultation. In this thesis, the focus is on occultation measurements. Therefore, limb and nadir geometry are treated very briefly.

2.2.1 Occultation

The idea of occultation* measurements originates from astronomic investigations. The most impressive example is the observation of the Sun's corona during a solar eclipse. Beside spaceborne occultation measurements, the occultation technique has been used with many other objects as well: Moons eclipsed by their planet, stars eclipsed by their counterpart and so on. One special case is the investigation

*Originating from latin *occultatio*: concealment, hiding

of objects hidden by a celestial body with an atmosphere. Refractive effects can be observed and analysed with respect to density and extension of the atmosphere. All occultation measurements use the radiation of a rising or setting celestial body. In the case of spaceborne observations of the Earth's atmosphere, radiation of the Sun, the Moon, and of bright stars are used for occultation measurements whenever they shine directly through the atmosphere as illustrated in Figure 2.3. With

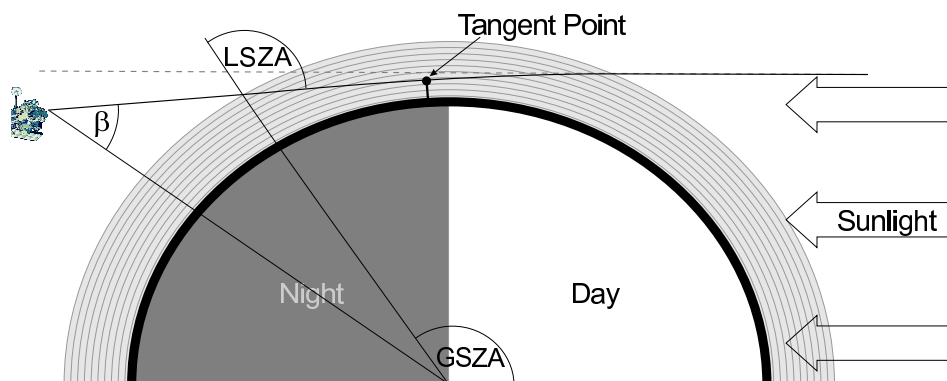


Figure 2.3: Occultation geometry. For computational issues, the atmosphere is assumed to extend to 100 km height.

experience from on-ground laboratory experiments and retrievals, it is possible to retrieve vertical profiles of trace gases, temperature, pressure, and information about aerosols. The technique of occultation measurements is wide-spread. Within the community of atmospheric sciences, on-ground measurements which use the direct light of the Sun, the Moon, or stars are also called occultation measurements differing a little bit from the original idea of occultation events. The reason for it is the close relationship using the direct irradiation of celestial bodies. Many other measurement techniques focus on indirect light scattered by the atmosphere or on artificial light sources.

Figure 2.3 shows also the basic concept of the numerical approach to occultation geometry. The atmosphere is divided into several layers. The height grid used throughout this study consists of a variable number of layers. Also the spacing of the height layers can be varied. In this thesis, the number of height layers is always set to one hundred with a constant step size of one kilometer. The actual light path through the atmosphere is called line of sight. Its closest point to the Earth's surface is defined as tangent point. The altitude of this point is the tangent height. Another important quantity is the solar zenith angle (SZA). Its geometric definition can be seen in Figure 2.3. It is a measure of relative position of an investigated air parcel with respect to the Sun and, in the case of solar occultation, it defines the line of sight. Within this thesis, SZAs are always given for the first intersection

of the line of sight with the top of atmosphere seen from the satellite. The top of atmosphere is defined to be at 100 km height throughout this thesis. Since the line of sight is directly related to the solar irradiation in occultation geometry, tangent height and SZA can be uniquely calculated from each other. Small deviations of this rule arise from viewing directions that do not match the centre of the Sun. In terms of SZA definitions used in this thesis, these cases are handled as if the true position of the Sun followed the scanning movement (see Section 2.1.2). Such calculations are performed with and without refractive effects within the atmosphere. In the case of a refractive atmosphere, the line of sight is bent towards the Earth's surface (solid line in Figure 2.3). Therefore, the SZA can be defined locally with respect to the line of sight (LSZA) differing a bit from the global solar zenith angle (GSZA). Unless stated otherwise, the GSZA is used throughout this work. Note that also the tangent height depends on the refraction model.

Some simple geometric relations can be deduced from these considerations. For the case of a non-refractive atmosphere, the tangent height h_g and the solar zenith angle ψ at the top of atmosphere are related by

$$h_g = (R_E + h_t) \sin \psi - R_E \quad (2.4)$$

and

$$\psi = \arcsin \left(\frac{h_g + R_E}{h_t + R_E} \right). \quad (2.5)$$

h_t is the defined height of the atmosphere above the surface and R_E is the radius of the Earth. In the context of real occultation spectrometers, the instrument elevation angle β is an important quantity (see Section 2.1.2). It has to be transformed into more convenient variables. The conversion from elevation angle β to tangent height h_g for an orbit altitude h_{orb} is the same as in Equation 2.4:

$$h_g = (R_E + h_{orb}) \sin \beta - R_E. \quad (2.6)$$

Difficulties may arise from different definitions of elevation angle β with respect to its zero-point. In Figure 2.3, $\beta = 0$ means observation of the nadir directly below the satellite. Sometimes, it is useful to define $\beta = 0$ as exact alignment with the solar centre. Definitions with respect to the flight direction are also used.

The main disadvantage of occultation measurements is the limited spatial coverage. Occultations can only take place at the terminator between day and night and in the case of SCIAMACHY only in the northern hemisphere, as SCIAMACHY is limited to sunrises in flight direction rather than sunsets in the opposite direction. Due to the sun-synchronous orbit, solar measurements are performed always at the same geographic latitude. The latitude varies throughout the year. In Figure 2.4, latitude at tangent point is plotted versus the days of the year 2003. For solar occultations, changes in the seasonal dependence can be neglected, i.e. the plot is

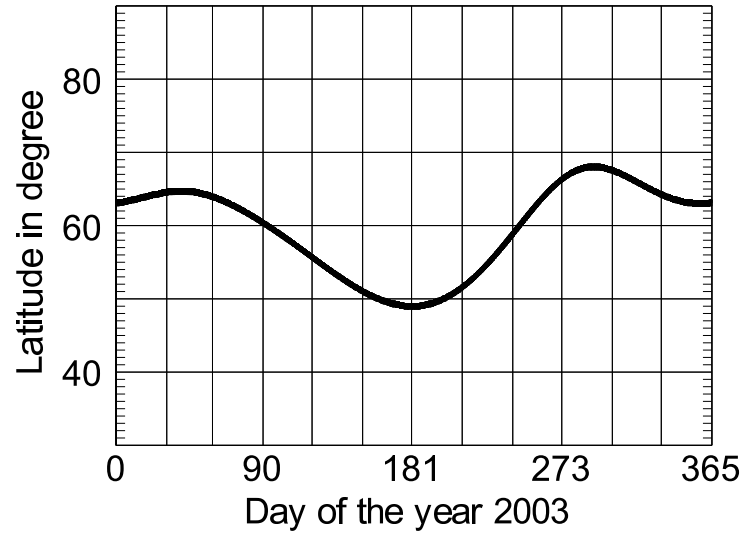


Figure 2.4: Geographic latitude of tangent points for SCIAMACHY solar occultation events in the year 2003.

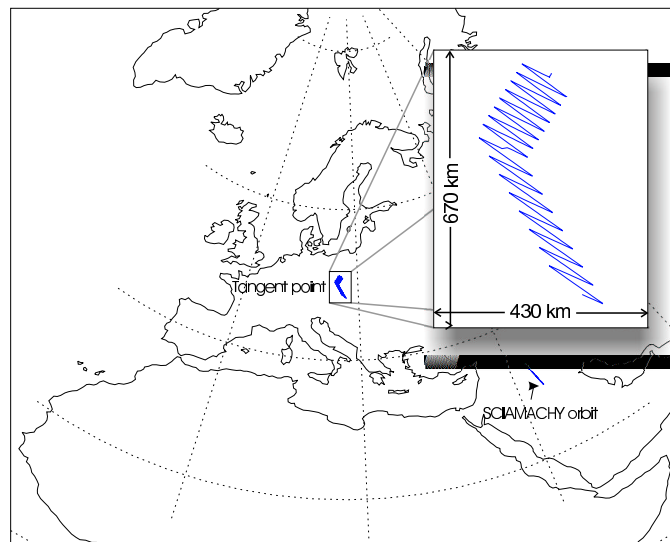


Figure 2.5: Geolocation of tangent point and sub satellite point during the solar occultation measurement sequence of orbit 2056 on July 22, 2002, 18:48 UTC.

valid for every year. Figure 2.5 shows sub satellite point and tangent point of a measurement sequence over Europe on July 22, 2002. It can easily be seen where the sun-follower tracks the rising Sun with a little azimuthal shift. One can also see that it is reasonable to assume one trace gas profile to be valid for a measurement sequence. In extreme cases of large horizontal gradients in the trace gas concentrations, small errors are obtained by this assumption. This will be discussed in more detail in Section 3.2.

2.2.2 Nadir and Limb

Only one to two minutes per orbit are used for occultation measurements. During the remaining 98 minutes, SCIAMACHY performs nadir and limb measurements on the day side and calibration measurements on the night side. Occasionally, there is the additional opportunity for lunar occultation depending on the lunar phase. Nadir designates the point directly under the satellite in opposite to the zenith. Limb means the Earth's limb, i.e. only the atmosphere without the Earth's surface is in the instrument FOV. The main difference to the occultation geometry is that no direct light is observed as can be seen in Figure 2.6.

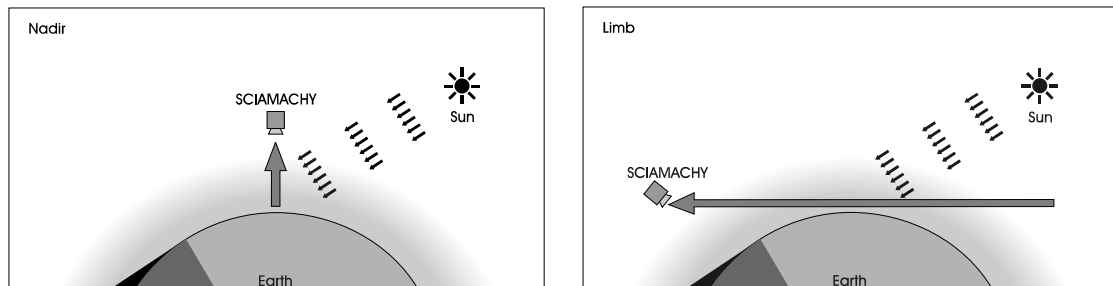


Figure 2.6: Nadir and limb geometry. Both techniques use scattered and reflected light in contrast to occultation geometry.

On the one hand, nadir and limb measurements are more or less feasible on the whole day side even under twilight conditions bearing a very good spatial coverage. On the other hand, the radiative transfer modeling needed for retrieval is much more complex than for occultation geometry, especially for limb. A clear improvement compared to previous nadir and limb spectrometers is the possibility of combined limb/nadir evaluation. The same air parcels are first measured in limb and seven minutes later in nadir geometry. Therefore, it will be easier to distinguish between tropospheric and stratospheric contributions.

2.3 Other Instruments

Since the 1970s, many satellite projects have been created. All of them would be worthwhile to be reviewed in a special paper or thesis. This section focusses only on the major occultation projects and their important characteristics.

The instrument characteristics are separated into orbital parameters and spectroscopic properties. A spectrometer is always a result of scientific goals and the estimated costs. Nevertheless there is a trend towards more wavelength channels and higher spectral resolutions. Besides a general progress in technology, this is possibly due to the success of recent satellite instruments and the increased computing power to evaluate the data.

The orbital parameters are significant to the spatial and temporal coverage of the occultation measurements. A detailed discussion of this impact can be found in Section 2.1.1. Fixing of orbital parameters has to be coupled closely with the scientific goals of the project. Therefore, the orbital parameters of the considered satellites differ a lot whereas the successor satellites show often only improvements in the spectrometer itself.

The field of view of an occultation instrument and the scanning mode are an important factor for the overall retrieval algorithm. As discussed in Section 1.1, the solar disk is quite inhomogeneous. So, different FOV shapes and scanning modes lead obviously to completely different measurement spectra. Also the different spectral designs of the instruments make it more difficult to compare the inversion algorithms used in the retrieval of trace gas profiles.

2.3.1 ACE/MAESTRO

ACE (Atmospheric Chemistry Experiment) and MAESTRO (Measurement of Aerosol Extinction in the Stratosphere and Troposphere Retrieved by Occultation) were successfully launched onboard SCISAT-1 on August 12, 2003. ACE is a high-resolution (0.02 cm^{-1}) Fourier Transform Spectrometer based on a sweeping Michelson interferometer operating from 2 to 13 microns over two spectral bands. MAESTRO is a dual optical spectrograph that covers the UV-vis-NIR spectral region with a spectral resolution of 1–2 nm. More details can be found in [Walkty et al., 2000].

	ACE/MAESTRO
Vertical FOV	0.072°
Orbit	650 km non sun-synchronous 74° inclination
Spatial Coverage	Full coverage
Wavelength (ACE)	2–5.5 μm 5.5–13 μm
Wavelength (MAESTRO)	280–550 nm 500–1030 nm
Main targets	CO ₂ , CO, H ₂ O, O ₃ , N ₂ O, N ₂ O ₅ , CH ₄ , nitrogen species, halo- gen compounds, sulfur oxides, aerosols

Table 2.2: Characteristics of ACE/MAESTRO.

2.3.2 GOMOS

GOMOS (Global Ozone Monitoring by Occultation of Stars) is one out of ten instruments onboard ENVISAT. For the first time, it performs atmospheric measurements using the occultation technique with stars. There are roughly 25 stars which are bright enough for appropriate measurements resulting in a very good spatial coverage on the Earth's night side.

GOMOS is a moderate resolution spectrometer covering the UV and visible spectral range. The main scientific goals are height-resolved profile retrievals of ozone, NO_x and some halogen compounds that are relevant in the stratospheric chemistry. As a matter of course, orbital parameters are the same as for SCIAMACHY (see Section 2.1.1). The design of the spectral channels is given in Table 2.3. The first introduction to the GOMOS instrument was given by Bertaux et al. [1991].

Wavelength [nm]	Resolution [nm]	Targets
250–675	0.9	O ₃ , NO ₂ , NO ₃ , ClO, BrO, OClO
756–773	0.12	O ₂ (temperature)
926–952	0.16	H ₂ O
470–520	–	Photometers for
650–700	–	monitoring purposes

Table 2.3: Characteristics of GOMOS.

2.3.3 HALOE

The Halogen Occultation Experiment (HALOE) was launched on the Upper Atmosphere Research Satellite (UARS) spacecraft in September 1991 as part of the Earth Science Enterprise (ESE) Program. HALOE consists of different infrared detectors covering a spectral range from 2.45 to 10.04 μm . Broadband and gas filter channels are used in the instrument. The results are used for the validation campaigns of SCIAMACHY, especially for occultation measurements. A detailed description of the instrument, scientific goals, and first results can be found in [Russel et al., 1993].

		HALOE
IFOV	vertical	0.033°
	horizontal	0.1°
Orbit		585 km
		non sun-synchronous, polar 57° inclination
Spatial Coverage		80° North to 80° South
Wavelength range		2.45–10.04 μm
Main targets		O ₃ , HCl, HF, CH ₄ , H ₂ O, NO, NO ₂ , aerosols, pressure, temperature

Table 2.4: Characteristics of HALOE.

2.3.4 ILAS

ILAS stands for Improved Limb Atmospheric Spectrometer. The instrument was launched in August 1996 onboard ADEOS (ADvanced Earth Observing Satellite). It is a Fourier-transform spectrometer performing solar occultation measurements in the IR wavelength range. ILAS-II on ADEOS-II was launched on December 14 in 2002. It has similar characteristics with an extended spectral range. The ILAS-II instruments consist of grating spectrometers covering mainly the near far infrared wavelength range. The conceptual design and the data retrieval algorithms are discussed in [Sasano et al., 1995, Kuze et al., 1998].

		ILAS	ILAS-II
IFOV	vertical	2 km	1 km
	horizontal	13 km (visible: 2 km)	21 km
Orbit		800 km	800 km
		sun-synchronous, polar	sun-synchronous, polar
Spatial Coverage		55°–70° North (sunrise)	55°–70° North (sunrise)
		63°–87° South (sunset)	63°–87° South (sunset)
Wavelength ^a		753–784 nm (0.1 nm)	753–784 nm
		6.21–11.77 μm	3.0–5.7 μm
		(0.129 μm)	6.21–11.76 μm
			12.78 - 12.85 μm
Main targets		O ₃ , HNO ₃ , NO ₂ , N ₂ O, CH ₄ , H ₂ O, CFC-11, aerosols, temperature, pressure	O ₃ , HNO ₃ , NO ₂ , N ₂ O, CH ₄ , H ₂ O, CFC-11, CFC-12, ClONO ₂ , aerosols, temperature, pressure

Table 2.5: Characteristics of ILAS instruments.

^aSpectral Resolution is given in parentheses

		ORA
IFOV	vertical	2°
	horizontal	2°
Orbit		508 km
		28° inclination
Spatial Coverage		40° North to 40° South
Wavelength channels		1: 442 nm
		2: 435 nm
		3: 1013 nm
		4: 943 nm
		5: 600 nm
		6: 340 nm
		7: 259 nm
		8: 385 nm
Main targets		O ₃ , NO ₂ , H ₂ O, aerosols

Table 2.6: Characteristics of ORA.

2.3.5 ORA

The Occultation Radiometer (ORA) was launched in 1992 onboard EURECA (European Retrievable Carrier). It was planned as a small one-year mission. Its focus is on the UV-vis wavelength range. The instrument consists of eight broadband channels. An instrument description can be found in [Arijs et al., 1995]. A final discussion of results and the inversion algorithm is given by Fussen et al. [1997].

2.3.6 POAM

The polar ozone and aerosol measurement instrument (POAM) was a three-channel spectrometer mainly dedicated to ozone measurements. It failed immediately after launch in 1985. The successors POAM-II and POAM-III were launched in 1993 and 1998 onboard SPOT-3 and SPOT-4 (Satellite Pour l'Observation de la Terre), respectively. Both consist of nine channels equipped with photometers covering the UV-vis-NIRwavelength range. Measurements of POAM-III are extensively used for the validation of SCIAMACHY occultation measurements. POAM-III itself has already been validated in several campaigns [Randall et al., 2003, Lucke et al., 1999]. POAM-II is described in [Glaccum et al., 1996], whereas the POAM-III instrument is described by Lucke et al. [1999].

2.3.7 SAGE

SAGE (Stratospheric Gas and Aerosol Experiment) stands for a series of spaceborne occultation instruments. It started in the 1970s with the SAM experiments (Stratospheric Aerosol Measurement) and continued with SAGE onboard "Applications Explorer Mission B" (1979–1981), SAGE-II on ERBS (Earth Radiation Budget Satellite launched in 1984), and SAGE-III on Meteor-3M (launched in December 2001). SAGE-III is a multi-channel grating spectrometer covering the UV-vis-NIRwavelength range similar to SCIAMACHY. All other instruments up to SAGE-II were broadband instruments.

SAGE-III is the first instrument that performed also lunar occultation measurements. SAGE-III is planned to be extended by an instrument on the international space station in 2004. Results of SAGE-III are also used for SCIAMACHY validation. A detailed description of retrieval algorithms and the instrumental design can be found in [McCormick et al., 2002]. Results of the SAGE-III instrument are compared with SCIAMACHY occultation results in Chapter 5. The SAGE-II instrument is described in [Mauldin et al., 1985].

		POAM-II	POAM-III
IFOV	vertical	0.01°	0.013°
	horizontal	1°	0.81°
Orbit		833 km	833 km
		sun-synchronous, polar 98.7° inclination	sun-synchronous, polar 98.7° inclination
Spatial Coverage		54°–71° North (sunrise)	54°–71° North (sunrise)
		63°–88° South (sunset)	63°–88° South (sunset)
Wavelength channels ^a		1: 252.3 nm (4.4 nm)	1: 354 nm (9.7 nm)
		2: 441.6 nm (2.0 nm)	2: 439.6 nm (2.1 nm)
		3: 448.1 nm (2.1 nm)	3: 442.2 nm (2.1 nm)
		4: 601.4 nm (14.3 nm)	4: 603 nm (17.7 nm)
		5: 761.2 nm (2.2 nm)	5: 761.3 nm (2.3 nm)
		6: 781 nm (16.7 nm)	6: 779 nm (10.2 nm)
		7: 921 nm (2.1 nm)	7: 922.4 nm (2.6 nm)
		8: 936.4 nm (2.3 nm)	8: 935.9 nm (2.6 nm)
		9: 1060.3 nm (11.1 nm)	9: 1018 nm (11.6 nm)
Main targets	O ₃ , NO ₂ , H ₂ O, aerosols, temperature	O ₃ , NO ₂ , H ₂ O, aerosols, temperature	

^aEach channel has one detector for a specific wavelength with a spectral width given in parentheses.

Table 2.7: Characteristics of recent POAM instruments.

		SAGE-II	SAGE-III
IFOV	vertical	0.00833°	0.00833°
	horizontal	0.04167°	0.04167° (lunar: 0.0833°)
Orbit		650 km	1020 km
		non sun-synchronous 57° inclination	sun-synchronous, polar 97.5° inclination
Spatial Coverage ^a		80° North to 80° South	48°–80° North (sunrise) 34°–58° South (sunset)
Wavelength channels ^b		385 nm	287–293 nm
		448 nm	382–386 nm
		453 nm	432–450 nm
		525 nm	518–522 nm
		600 nm	560–596 nm
		940 nm	753–771 nm
		1020 nm	867–871 nm
			933–960 nm 1019–1025 nm 1530–1560 nm
Main targets		O ₃ , NO ₂ , H ₂ O, aerosols	O ₃ , NO ₂ , NO ₃ , OClO, H ₂ O, aerosols, clouds, pressure, temperature

^aLunar occultation of SAGE-III is highly variable and covers almost all latitudes.

^bIn SAGE-II, each channel has one detector for a specific wavelength with a spectral bandwidth of 10–20 nm. At 448 nm and 453 nm the width is 3 nm and 2 nm, respectively. SAGE-III has various detector systems with a spectral resolution of approximately 0.7 nm and 10 nm beyond 1000 nm.

Table 2.8: Characteristics of recent SAGE instruments.

Chapter 3

Simulation of Measurements

Basic part of each trace gas retrieval is the so-called forward model. The forward model maps the concentration profiles into the wavelength space with the spectroscopic data. It is needed by every retrieval method. Furthermore, it reflects the knowledge about the radiative transfer through the atmosphere. In this chapter, the radiative transfer model for occultation geometry will be introduced. Finally, some studies concerning the theoretical sensitivity of `SCIAMACHY` will be discussed.

3.1 Atmospheric Constitution

For a sophisticated radiative transfer model that can be used for complex retrievals, a broad understanding of atmospheric properties is required. Every retrieval method needs an a priori knowledge about trace gas mixing and aerosol loading.

Atmospheric Layers

It is useful to divide the atmosphere into different layers. This is commonly done by the characteristic behaviour of the vertical temperature gradient. Temperature is plotted versus altitude in Figure 3.1. The values are averaged globally. Since pressure, which decreases exponentially with height, is an important quantity to many applications, it is sometimes convenient as an alternative height scale. The atmospheric layers can be divided into two main different classes, characterised by temperature increase and decrease with height, respectively:

Troposphere The lowest layer of the atmosphere extending from the surface up

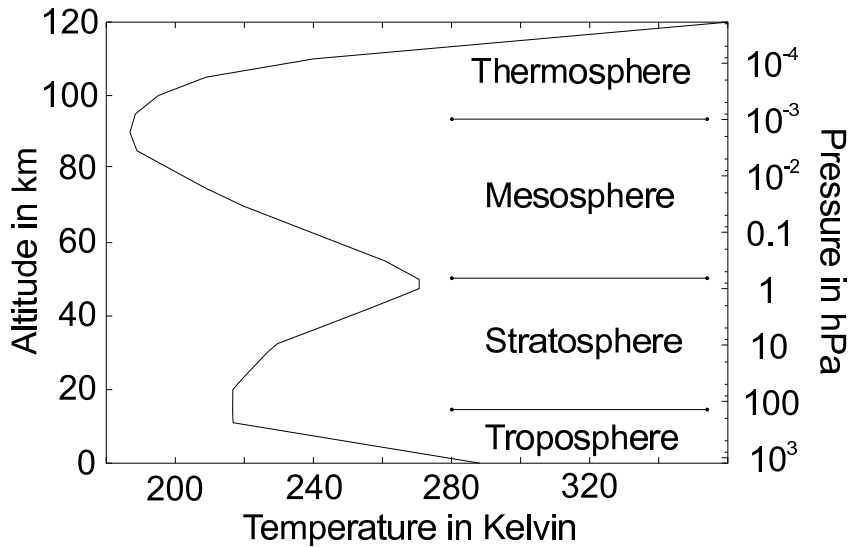


Figure 3.1: Temperature vs. altitude. It is the basis of a commonly used classification into layers. The logarithmic pressure scale on the right is often used as height scale. Data are taken from [NASA, 1976].

to 10–15 km is characterised by decreasing temperature with height and rapid vertical mixing due to solar irradiance and heating of the surface. All weather phenomena we observe every day take place within the troposphere.

Stratosphere The next layer extends up to approximately 50 km. Temperature increases with height as a result of the strong absorption in the ozone layer. Therefore, vertical mixing is slow.

Mesosphere It extends up to circa 90 km and is characterised by decreasing temperature and rapid vertical mixing. It ends with the coldest point in the atmosphere.

Thermosphere Here the temperature increases extremely due to absorption of short wavelength radiation by N_2 and O_2 . Nevertheless, vertical mixing is rapid.

Exosphere The outermost region beginning roughly at 500 km is the Exosphere from which molecules with high translational energies can escape into space.

The boundaries between the layers are called tropopause, stratopause, and mesopause, respectively. They are defined by the points of inflection in Figure 3.1. Sometimes, the upper mesosphere and the lower thermosphere are called ionosphere indicating a huge amount of ionised particles. The upper region dominated

by the Earth's magnetic field is also called magnetosphere. It is our protection against the solar wind.

Atmospheric Gases

At a global average, the dry Earth's atmosphere is mainly composed of the following gases:

Constituent	Mixing ratio [ppm]
Nitrogen (N ₂)	780,840
Oxygen (O ₂)	209,460
Argon	9,340
Carbondioxid (CO ₂)	355
Neon	18
Helium	5.2
Methan (CH ₄)	1.72
Krypton	1.1
Ozone (O ₃)	0.01–0.1
Nitrogenoxides (NO _x)	10 ⁻⁶ –10 ⁻²

Most of them are well mixed, i.e. their mixing ratios are almost constant throughout the atmosphere, as they are chemically inert. Other gases that are more active such as ozone show a certain height distribution. Nitrogenoxides are also locally related to combustion on the Earth's surface.

The calculation of vertical concentration profiles is the major task of occultation measurements. To obtain them properly, a priori knowledge about the height distribution is required. Throughout this thesis, the U.S. standard climatology from 1976 is used [NASA, 1976] as well as information provided by Anderson et al. [1986] and model calculations from the Max-Planck-Institute, Mainz [Brühl and Crutzen, 1991]. They contain global averages and estimations of pressure, temperature, and trace gas profiles. Standard profiles for O₃ and NO₂ are shown in Figure 3.2. Here, they are given in volume mixing ratios as well as in absolute concentrations. Considering trace gases to be approximately ideal gases, the volume mixing ratio is also the mixing ratio in terms of molecule numbers. It is a common unit within atmospheric sciences. In the case of spectroscopic measurements, absolute concentrations are needed for calculation of optical thicknesses, as will be discussed in Section 3.2. Particle number density N can be calculated from volume mixing ratio VMR, pressure p , and temperature T via the ideal gas law:

$$N = \text{VMR} \cdot \frac{p}{RT} \cdot N_A, \quad (3.1)$$

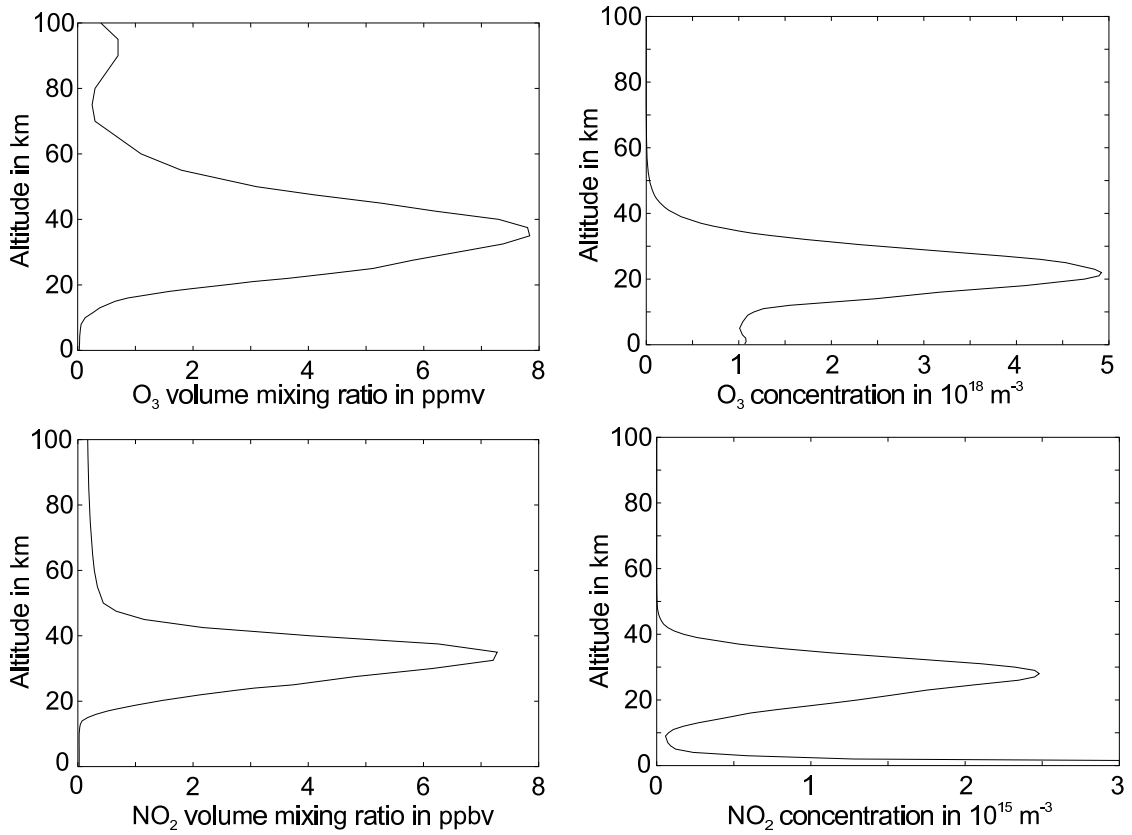


Figure 3.2: Globally averaged vertical profiles of O₃ and NO₂ [NASA, 1976] given in volume mixing ratio and absolute concentrations.

where $R = 8.31441 \frac{\text{J}}{\text{mol}\cdot\text{K}}$ is the molar gas constant and $N_A = 6.022 \cdot 10^{23} \text{mol}^{-1}$ the Avogadro constant.

Aerosols

Aerosols are generally considered to be particles in the range from a few nanometers to tens of micrometers. They can be liquid or solid. The technical definition of aerosols contains a suspension of particles in a gas. In atmospheric sciences, the expression focusses only on the particles. For occultation measurements, mainly the region of the upper troposphere and the lower stratosphere is of interest. The aerosol background in this region is mainly provided by carbonyl sulfide (OCS). Its life time is long enough to diffuse from onground sources into the stratosphere. There it is dissociated by UV-radiation and forms sulfuric acid solutions. Occasionally, large volcanic eruptions inject considerable amounts of SO₂ into the stratosphere, resulting also in sulfuric acid aerosols. In the lower troposphere, one

can find any imaginable kind of aerosol: dust, smoke, soot, smog, and of course water and ice. The main natural sources are windborne dust, sea spray, and volcanoes. But nowadays, a significant part is of anthropogenic origin, especially close to the urban centers.

Details of this short introduction can be found in [Seinfeld and Pandis, 1998]. The outer atmosphere is discussed in [Hargreaves, 1992].

3.2 Transmission through the Atmosphere

For simulation of atmospheric transmission, it is necessary to know extinction properties of atmospheric constituents and their spatial distribution as introduced in Section 3.1. This section describes the theoretical approach to radiative transfer modeling as it is needed for occultation geometry. It is also a basic part of the retrieval algorithm described in Chapter 4, where it is referred to as the forward model. It has been developed during the last years at the Institute of Environmental Physics in Bremen. The adaptation to occultation geometry was mainly introduced by Alexei Rozanov [Rozanov, 2001].

3.2.1 Extinction Processes

Every atmospheric constituent has characteristic spectral absorption and scattering properties. There are certain absorption maxima at those wavelengths with corresponding energy gaps of allowed transitions in the molecule. There are rotational, vibrational, and electronic transitions possible. Incident radiation can either be absorbed or scattered. As will be shown in Section 3.4, only extinction processes are interesting in occultation geometry. This means that multiple scattered light and molecular emissions can be neglected. It is only the reduction of intensity by the extinction processes mentioned above that can be detected. All processes lead to a wavelength dependent probability for interaction with incident photons. The probability can be normed to a virtual area which has to be hit by a photon for interaction with one molecule. This area per molecule is called cross-section σ . For a given molecule, it depends on wavelength λ or wavenumber ν whereas the average cross-section of all molecules in a gas also depends on pressure p , and temperature T . Multiplying cross-section and number density N of a species leads to the absorption coefficient α . Furthermore, cross-sections and extinction/absorption coefficients can be superposed to an overall extinction coefficient:

$$\alpha(\nu, p, T) = \alpha_a(\nu) + \alpha_r(\nu) + \sum_{i=1}^M \sigma_i(\nu, p, T)N_i. \quad (3.2)$$

It is a sum of trace gas contributions, aerosol extinction coefficient α_a , and Rayleigh scattering α_r , where M is the number of relevant trace gases. An introduction to the basic theory of photon-particle interactions can be found in [Demtröder, 1995].

Absorption

Cross sections of trace gases are either calculated with the so-called line-by-line method or taken from measured moderate resolution cross section spectra such as presented in [Bogumil et al., 1999] and [Burrows et al., 1998]. Measured cross sections are commonly used in the UV-vis wavelength range. The fine spectral structures of O₂, H₂O, and typical infrared absorbers need to be simulated with the line-by-line method, which is discussed in this section. Spectroscopic data for the line-by-line calculations are taken from the HITRAN* database [Rothman et al., 1998]. A collection of different absorption cross sections can be found in Appendix B.

The general dependence of spectral absorption on wavenumber ν , pressure p , and temperature T can be described by

$$\sigma(\nu, p, T) = \sum_i S(\nu_i, T) F(\nu, \nu_i, p, T). \quad (3.3)$$

It is the sum over all absorption lines subscribed with i . The line intensity is given by the function $S(\nu_i, T)$ and $F(\nu, \nu_i, p, T)$ is the line shape function. According to Goody [1964], $S(\nu_i, T)$ can be obtained from one intensity S_0 at a distinct temperature T_0 :

$$S(\nu_i, T) = S_0(\nu_i, T_0) \frac{n(T) \left(1 - e^{-\frac{hc\nu_i}{kT}}\right)}{n(T_0) \left(1 - e^{-\frac{hc\nu_i}{kT_0}}\right)}. \quad (3.4)$$

n is the population of the lower energy level of the considered transition, k is the Boltzmann constant, c the speed of light, h the Planck constant. The population n_i of an energy level i is described by the Maxwell-Boltzmann distribution:

$$n_i(T) = \frac{N g_i e^{-\frac{E_i}{kT}}}{\sum_i g_i e^{-\frac{E_i}{kT}}}. \quad (3.5)$$

g_i is the degeneracy of level i with energy E_i and N is the total number of electrons sharing the energy levels. $\sum_i g_i e^{-\frac{E_i}{kT}}$ is the so-called partition function. It becomes

*High resolution TRANsmission molecular absorption

a combination of rotational and vibrational partition functions in the case of atmospheric absorption. According to Gamache et al. [1990], the combined partition function $Q^{v,r}$ can be approximated by a polynomial of temperature T ,

$$Q^{v,r} = a_0 + a_1T + a_2T^2 + a_3T^3, \quad (3.6)$$

which is also used in the HITRAN data base.

The line shape function $F(\nu_i, \nu, p, T)$ reflects two broadening mechanisms, Doppler broadening and pressure broadening. In the troposphere and the lower stratosphere, the pressure broadening is dominant. Lifetimes of excited molecular states are reduced due to collisions between molecules. Since the absorption line width is reciprocal to the life time of its excited state, the line appears broadened, which is described by

$$F_L(\nu_i, \nu, p, T) = \frac{\alpha_L}{\pi((\nu - \nu_i)^2 + \alpha_L^2)}. \quad (3.7)$$

Here, α_L is the Lorentz line width. It follows from kinetic theory that α_L is proportional to pressure [Goody, 1964]. Starting with a known Lorentz line width at temperature T_0 and pressure p_0 , α_L becomes

$$\alpha_L(p, T) = \alpha_L(p_0, T_0) \frac{p}{p_0} \left(\frac{T_0}{T} \right)^\gamma, \quad (3.8)$$

where γ is a coefficient also provided by the HITRAN database. Furthermore, spectral lines are not only broadened but also shifted. This effect is proportional to pressure p and can be described with another coefficient η supplied by the HITRAN database:

$$\nu_i^* = \nu_i + \eta \frac{p}{p_0}. \quad (3.9)$$

Additionally, there is shift due to the Doppler effect. It can be expressed by

$$\nu - \nu_i = \frac{\nu_i u}{c} \quad (3.10)$$

if molecule velocities u are small compared to the speed of light c . The Doppler shift becomes relevant in the upper stratosphere and mesosphere. Averaging over the Maxwell distribution

$$P(u) = \sqrt{\frac{m}{2\pi kT}} \cdot e^{-\frac{mu^2}{2kT}} \quad (3.11)$$

with molecular mass m , temperature T , and Boltzmann constant k , the line shape function due to the Doppler broadening becomes

$$F_D(\nu_i, \nu, T) = \frac{e^{-\left(\frac{\nu - \nu_i}{\alpha_D}\right)^2}}{\alpha_D \sqrt{\pi}}, \quad (3.12)$$

where α_D is the Doppler line width:

$$\alpha_D = \frac{\nu_i}{c} \sqrt{\frac{2kT}{m}}. \quad (3.13)$$

In the middle atmosphere, both broadening mechanisms have to be taken into account. Combining all shift and broadening effects, leads to the Voigt line shape function

$$F_V(\nu_i, \nu, p, T) = \int_{-\infty}^{\infty} \frac{\alpha_L}{\pi} \sqrt{\frac{m}{2\pi kT}} \frac{e^{-\frac{mu^2}{2kT}}}{(\nu - \nu_i^* - \frac{u\nu_i}{c})^2 + \alpha_L^2} du, \quad (3.14)$$

which is used in the forward model.

Scattering

There are two relevant types of scattering in the atmosphere. Rayleigh scattering means elastic interactions between photons and molecules. Aerosol scattering is described by the Mie theory [Mie, 1908]. The scattering coefficient per molecule ϵ is basically a function of wavelength λ . For the case of the Earth's atmosphere gas mix, ϵ is given by Chandrasekhar [1960]:

$$\epsilon(\lambda) = \frac{32\pi^3(n_s - 1)^2}{3\lambda^4 N_A^2} \cdot \frac{6 + 3\rho}{6 - 7\rho}, \quad (3.15)$$

where n_s is the refractive index of air under standard conditions and N_A is the Avogadro constant. ρ is the depolarisation factor of air according to King [1923]. Equation 3.15 is already an approximation for refractive indices n_s close to one. It is impossible to obtain exact values for n_s as the atmosphere is a highly variable mix of different gases. A common approximation is given by Edlen [1966]:

$$(n_s - 1) \cdot 10^8 = 8342.13 + \frac{2,406,030}{130 - \lambda^{-2}} + \frac{15,997}{38.9 - \lambda^{-2}}. \quad (3.16)$$

The extinction coefficient due to Rayleigh scattering $\alpha_r(\nu)$ in Equation 3.2 is then

$$\alpha_r(\nu) = N\epsilon(\nu) \quad (3.17)$$

after conversion from wavelengths to wavenumbers ($\nu = 1/\lambda$). N is the total molecular number density of air.

According to the Mie theory [Mie, 1908, Deirmendjian, 1969], the extinction coefficient due to aerosol scattering $\alpha_a(\nu)$ is

$$\alpha_a(\nu) = N_a \int_0^{\infty} \pi r^2 k_{ext}(r, n, \lambda) f_a(r) dr, \quad (3.18)$$

where N_a is the aerosol particle number density, r is the particle radius, k_{ext} the extinction coefficient for one particle, and $f_a(r)$ the particle size distribution function. k_{ext} depends naturally on wavelength λ and radius r but also on the relative refractive index n . It is the ratio of particle refractive index and the index of the surrounding medium. Aerosol profiles and optical properties are taken from the LOWTRAN-7[†] aerosol model [Kneizys et al., 1988].

3.2.2 Radiative Transfer Model

In [Rozanov, 2001], occultation geometry is treated as a particular case of a more general atmospheric geometry, where a point in the atmosphere is described by three spherical coordinates, solar zenith angle ψ , solar azimuth angle ϕ , and radius r . Since atmospheric transmission is simple compared to complete 3-dimensional descriptions of radiative transfer, this section is kept brief and focusses only on important quantities. In Section 2.2.1, foundations of occultation geometry were introduced. It was mentioned that the line of sight is uniquely defined by the solar zenith angle ψ at the top of the atmosphere, i.e. r is a function of ψ and ϕ is always zero. The central formula is based on the Lambert-Beer Law of extinction:

$$I(\psi, \lambda) = I_0(\lambda) \cdot e^{-\tau(\psi, \lambda)}. \quad (3.19)$$

I is the intensity after passing the atmosphere, I_0 the extraterrestrial intensity, λ the wavelength, and τ the full optical depth along the line of sight given by

$$\tau(\psi, \lambda) = \int_0^{s_o} \alpha(\tilde{\psi}(s), \lambda) ds, \quad (3.20)$$

where s denotes the path length within the atmosphere, s_o the total path length, $\tilde{\psi}$ the local solar zenith angle for each path element and α the extinction coefficient introduced in Section 3.2.1. In terms of a real computer algorithm, the path length elements ds refer to the height layer grid of Figure 2.3. They can be calculated with and without refraction. The applied ray-tracing algorithm was developed by Johannes Kaiser [Kaiser, 2001]. It is based on Snell's law. A light ray hitting the boundary of two height layers i and j with angle θ_i to the perpendicular will leave with angle θ_j obtained by

$$\sin \theta_j = \frac{n_j}{n_i} \sin \theta_i. \quad (3.21)$$

$n_{i,j}$ are the refractive indices, which are calculated with Equation 3.16. Furthermore, ds can be substituted by corresponding height steps dh :

$$ds = \frac{dh}{\cos \tilde{\psi}(h)}. \quad (3.22)$$

[†]LOWTRAN stands for LOW resolution atmospheric TRANsmission

Introducing a new function χ which is similar to the Heaviside function, the integration in Equation 3.20 can be written as

$$\tau(\psi, \lambda) = \int_{h_b}^{h_t} \frac{\chi(\psi, h')}{\cos \tilde{\psi}(h')} \alpha(\tilde{\psi}(h'), \lambda) dh'. \quad (3.23)$$

Since the line of sight geometry is symmetric to the tangent point and α is assumed to be independent of the solar zenith angle ψ , it is sufficient to integrate only once from the bottom h_b to the top h_t of atmosphere with

$$\chi(\psi, h') = \begin{cases} 2 & \forall h' > h_g \\ 0 & \forall h' \leq h_g \end{cases}, \quad (3.24)$$

where h_g is the tangent height, which is either calculated by the ray-tracing routines or geometrically by Equation 2.4.

Taking more details into account, Equation 3.19 has to be revised. Since real spectrometers cover a finite solid angle Ω and single detector pixels correspond always to a finite wavelength interval $\Delta\lambda$, the radiance Υ measured by a real instrument can be written as

$$\Upsilon(\psi, \lambda, \beta) = \int_{\Omega} d\omega \int_{\Delta\lambda} d\lambda' I_0(\lambda', \beta) f(\omega) a(\lambda, \lambda') e^{-\tau(\psi, \lambda, \omega)} \quad (3.25)$$

with ω as solid angle. $a(\lambda, \lambda')$ is the slit function given by one of the Equations 2.1–2.3. $f(\omega)$ describes the field of view characteristics, also introduced in Section 2.1.2. Theoretically, it must be integrated over the whole field of view. In practice, only those parts have to be considered that are illuminated by the solar disk, i.e. $f(\omega) = 1$ if $d\omega$ is illuminated otherwise $f(\omega) = 0$. Note, that Υ and I_0 depend now also on the scanning angle β of the instrument. Definitions of β depend on the context. In Figure 2.3, β is defined with respect to the nadir direction. Here, it is useful to define $\beta = 0$ to be exactly centred on the solar disk with maximum intensity. I_0 is reduced by the limb darkening effect described in Section 1.2 in combination with the geometrical effect of a decreasing solar disk area within the FOV. The effect is governed by Equation 1.9. Its adaptation to SCIAMACHY was already described in detail by van Rie [1995] and is part of the forward model. Additionally, the sun flattening (see Section 6.2.2) affects significantly the radiation Υ , especially the dependence on β . This has not yet been implemented in the forward model as this effect is quite complex and hard to simulate.

3.2.3 Modeled Spectra

A typical on-ground atmospheric spectrum is shown in Figure 3.3. It is given for

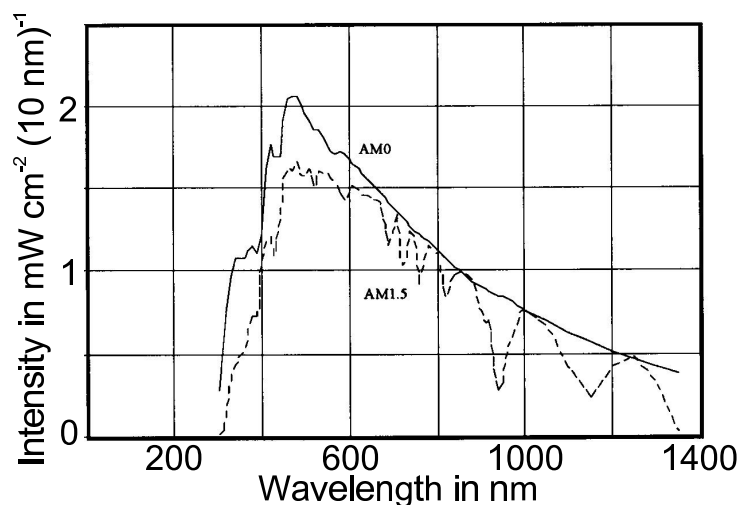


Figure 3.3: On-ground solar spectrum (AM 1.5, dotted line) compared to an extraterrestrial spectrum (AM 0, solid line) [Roche, 1997].

an air mass factor[‡] of 1.5 compared to an extraterrestrial spectrum with AM 0. It gives an overview of different atmospheric absorption features, especially the ozone-bands in the UV and visible wavelength range and water absorption in the IR range. The forward model introduced in the previous sections can be used for accurate modeling of atmospheric transmission in occultation geometry. Assuming only direct light to be measured, modeled transmissions can easily be identified with measured spectra. On the top of Figure 3.4, atmospheric transmission obtained from SCIAMACHY measurements is plotted as function of wavelength with a tangent height of approximately 30 km. Here it is even clearer how strong absorption is in the UV-vis range. On the bottom of Figure 3.4, the same transmission was simulated with the forward model discussed in Section 3.2.2. Though wavelength range is quite large in both cases, it is obvious that the differential structure of the transmission spectra can be modeled quite accurately. Admittedly, there is some difference in the absolute transmission values. It can be explained by an incorrect calculation of the measured transmission. For absolute transmission values, it is necessary to assign correct references to the atmospheric measurements with respect to the solar disk geometry. As will be discussed in Section 6.2, it is difficult to find an appropriate reference measurement without further efforts. Here, the reference was just one of the measurements near the solar disk centre.

[‡]Air mass factors denote the total amount of air passed by radiation or a single light ray. A simple definition is given by $AM = \frac{p}{p_0 \sin \theta}$, with pressure p at observation point, pressure at ground level p_0 , and viewing angle θ above the horizon.

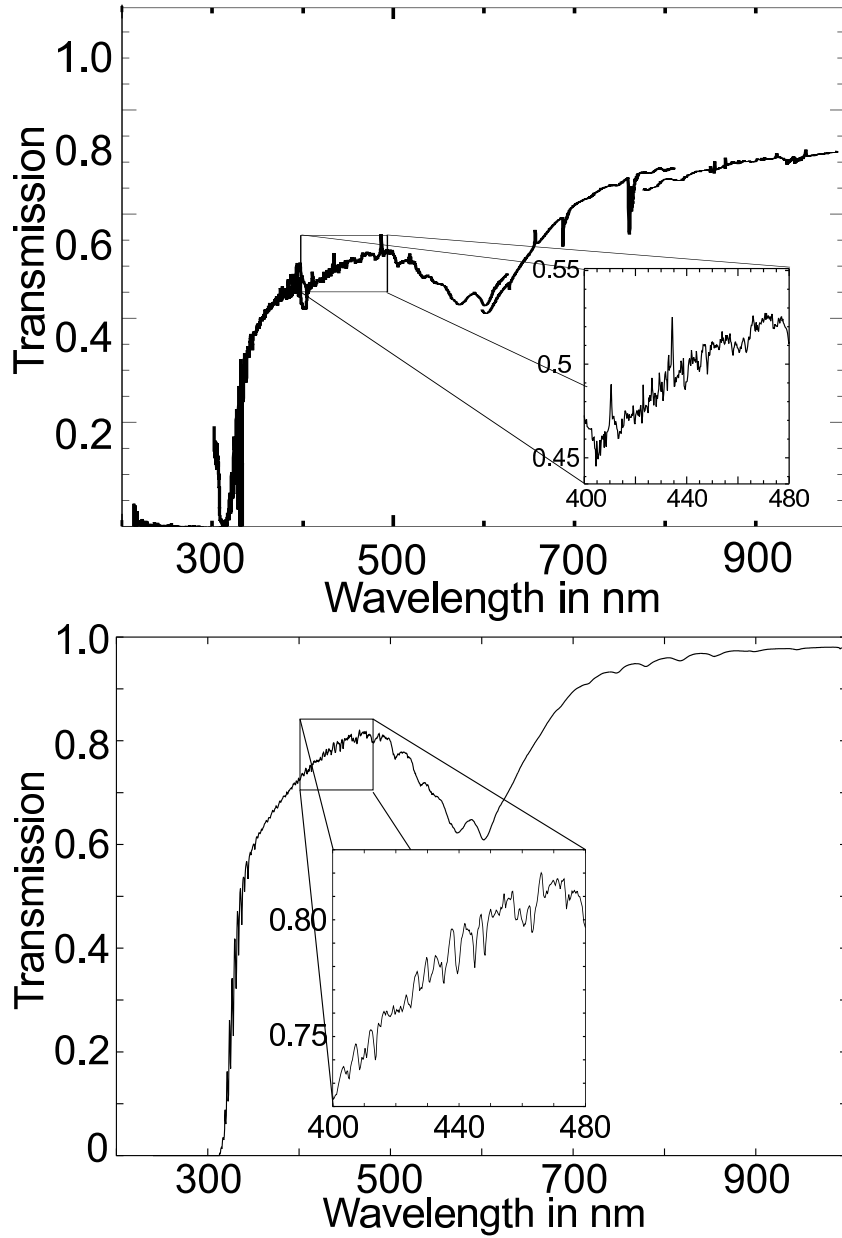


Figure 3.4: Top: Atmospheric transmissions obtained from SCIAMACHY solar occultation measurements. Bottom: Modeled transmissions. Both plots correspond to a tangent height of approximately 30 km.

3.3 Scattered Light

3.3.1 Background

Throughout this thesis, radiance measured in occultation geometry is assumed to consist only of direct radiation. In this section, it is shown that the neglect of contributions by scattered light is not true for every imaginable case, especially in the UV region. For evaluation of occultation measurements, it is interesting to find out at which tangent heights and in which spectral regions the assumption of pure direct radiation can be maintained. For simulation of scattered light, two spherical radiative transfer models were developed at the Institute of Environmental Physics by Alexei Rozanov [Rozanov et al., 2000, 2001] and Johannes Kaiser [Kaiser et al., 2002]. Detailed descriptions can be found in [Rozanov, 2001] and [Kaiser, 2001].

For the following studies, the combined differential-integral approach for the solution of the radiative transfer equation has been used [Rozanov et al., 2000]. It includes single and multiple scattering in the atmosphere. Occultation radiative transfer is only a special case of a general full spherical radiative transfer. Irradiation I treated in Section 3.2.2 can be rewritten as

$$I = I_{dir} + I_{dif} \quad (3.26)$$

in a more general form. I_{dir} is the direct radiation from Equation 3.19 and I_{dif} is the diffuse radiation, which can be written in terms of single and multiple scattering source functions J_{ss} and J_{ms} , respectively:

$$\frac{dI_{dif}(\mathbf{r}, \mathbf{e}_s)}{ds} = -\alpha \left(I_{dif}(\mathbf{r}, \mathbf{e}_s) - J_{ms}(\mathbf{r}, \mathbf{e}_s) - J_{ss}(\mathbf{r}, \mathbf{e}_s) \right). \quad (3.27)$$

Note the dependencies on the general space vector \mathbf{r} and the unity vector \mathbf{e}_s indicating the direction of radiation. α is the extinction coefficient introduced in Section 3.2.1. J_{ss} is directly related to the incident direct irradiation I_0 . Introducing the phase function $p(\gamma)$, which denotes the probability that a photon is scattered forming an angle γ with the incident radiation, J_{ss} becomes

$$J_{ss}(\mathbf{r}, \mathbf{e}_s) = \frac{\varpi}{4\pi} p(\mathbf{r}, \gamma) I_{dir}. \quad (3.28)$$

ϖ is the single scattering albedo representing the probability that a photon is scattered rather than absorbed. J_{ms} is defined recursively as it depends on the amount of radiation that has already been scattered once or several times:

$$J_{ms}(\mathbf{r}, \mathbf{e}_s) = \frac{\varpi}{4\pi} \int_{\Omega} d\omega p(\mathbf{r}, \gamma) I_{dif}, \quad (3.29)$$

integrated over all directions in space.

3.3.2 Results

Taking the FOV properties of SCIAMACHY into account, it is possible to assign correlated amounts of scattered light virtually to each occultation measurement. Combining simulation of directly transmitted light (see Section 3.2) and scattered light, Figure 3.5 shows the relative fraction of diffuse light as a function of wavelength for several tangent heights and background aerosol conditions. Two cases are

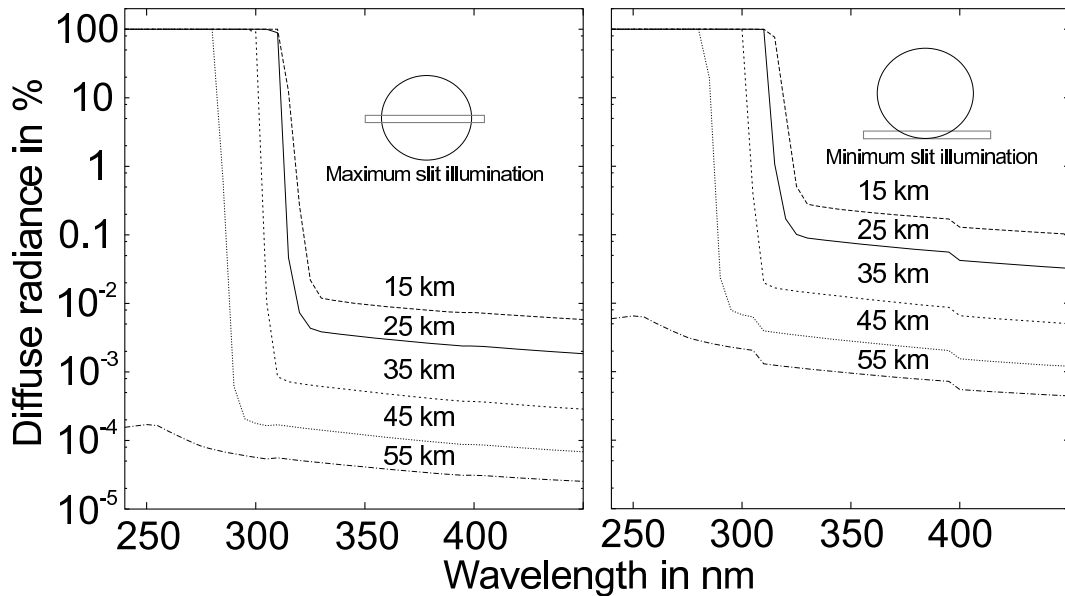


Figure 3.5: Relative fraction of diffuse light in SCIAMACHY occultation measurements in percent vs. wavelength for several tangent heights and background aerosol conditions. To the left, a centred position of SCIAMACHY's FOV is assumed. To the right, the FOV is less illuminated.

distinguished: a maximum illumination of SCIAMACHY's FOV and some minimum illumination according to the discussion in [van Rie, 1995]. Minimum illumination of course would mean no illumination. Here, it was intended to investigate an appropriate extreme case. It is conspicuous that there is a very sharp cut off depending on tangent height. This can mainly be explained by the strong ozone absorption of the Hartley-Huggins band. Therefore, the relative fraction of diffuse radiation is strongly reduced at tangent heights beyond the ozone layer. For low tangent heights, aerosol extinction becomes significant as well. This can be seen in comparison to Figure 3.6. The plots are of the same kind, except that moderate aerosol contamination was chosen for calculation of direct and diffuse radiation.

As can clearly be seen in all cases, diffuse radiation becomes the major part of occultation measurement signal in the UV spectral range throughout the tropo-

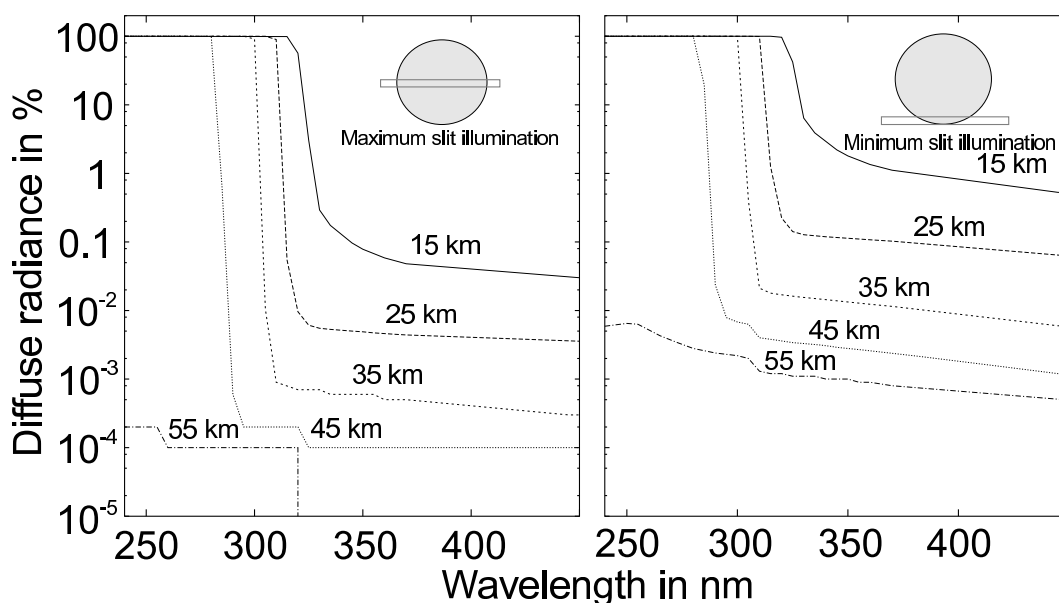


Figure 3.6: Relative fraction of diffuse light in SCIAMACHY occultation measurements in percent vs. wavelength for several tangent heights and moderate aerosol loading. To the left, a centred position of SCIAMACHY’s FOV is assumed. To the right, the FOV is less illuminated.

sphere and the stratosphere. The atmosphere is opaque in this wavelength region. In the visible and IR range, differences in the fraction of diffuse light vary by up to two orders of magnitude depending on the FOV illumination and aerosol loading. Variations due to the FOV pointing are caused by two phenomena. In the first place, direct irradiation is obviously reduced by pure geometric effects of the solar disk whereas diffuse radiation depends only on atmospheric conditions. Secondly, the limb darkening effect (see Section 1.4.1) causes a stronger reduction at the solar limb than expected from geometric calculations. The implementation of the limb darkening effect is discussed in Section 3.2.2. Since averaged values of limb darkening calculations were used for each spectral channel of SCIAMACHY, a small jump can be observed around 390 nm, where the channels 2 and 3 have an overlap. In Figure 3.6, the jump is missing. Here, the limb darkening effect was neglected as it plays only a minor role.

For trace gas retrieval, occultation measurement signals are assumed to be only composed of direct irradiation. Tests with simulated data showed that a diffuse fraction of a few percent does not affect the retrieval result. As a result of this study, one can say that occultation measurements can be evaluated with the relatively simple Lambert-Beer Law of extinction for wavelengths beyond the sharp cut off. This is still true for moderate aerosol loading and measurements at

the solar limb. As will be shown in Section 3.4.1, it is not meaningful to evaluate those cut off regions in any event as the signal-to-noise ratio breaks down in this region.

3.4 Retrieval Aspects

The forward model introduced in this chapter is a central part of the retrieval algorithm, which is described in Chapter 4. As shown before, intensities measured by SCIAMACHY can be simulated. In this section, results of spectral and instrumental simulations are discussed with respect to further application within the retrieval of atmospheric parameters as discussed in the second part of this thesis.

3.4.1 Signal-to-noise Ratio

The signal-to-noise ratio (SNR) is a limiting factor for measurement accuracy. Since the differential structure of atmospheric transmission is used for trace gas retrieval, the reciprocal of the SNR must be smaller than the trace gas extinction signal. A simulation tool has been programmed for modeling SCIAMACHY measurement noises[§]. The Instrument Simulation Software (ISS) was developed at SRON[¶] [de Vries et al., 1997]. It includes the following effects.

- Dark current noise
- Thermal background noise
- Photon shot noise
- Johnson diode noise
- Electronic noise
- 1/f noise
- Popcorn noise

Details of dark current and noise, especially in the IR, can be found in [Hoogeveen et al., 2001]. ISS input data are modeled or real spectra (radiances or irradiances) as

[§]Details of the Instrument Simulation Software can be found on the internet at <http://www.sron.nl/divisions/eos/atmos/sciasim/sciasim.html>

[¶]Space Research Organisation Netherlands

they are calculated by the forward model or measured by *SCIAMACHY*, respectively. In a so-called travelling spectrum approach, an instrument throughput is calculated and applied to the input spectrum. All known characteristics of optical devices within the instrument are taken into account. It is a complete simulation of the detector signal, which the SNR can be calculated from.

The SNR has been calculated for the wavelength range of *SCIAMACHY* and for all interesting cases of occultation geometry. Figure 3.7 shows an overview of SNRs at several tangent heights for background aerosol conditions. It can be seen that the SNR is fairly high in most cases. Only for small tangent heights, the SNR breaks down in the UV and shortwave visible range. Similar to Figure 1.4, the different detector materials of channel 6 show different SNR characteristics as well.

Taking a closer look at the UV-vis spectral range, Figure 3.8 shows a comparison between the diffuse light study of Section 3.3 and the SNR at 10 km tangent height. Here, the two cases of maximum (solid line) and extremely low (dotted line) illumination are also distinguished. Aerosol loading corresponds to background conditions. It can be concluded that the direct irradiation is virtually vanished in the UV spectral range by ozone absorption resulting in a correspondingly low SNR. The qualitative behaviour appears at all relevant tangent heights and for different aerosol conditions. It is mainly the cut off wavelength which shifts a little bit under different conditions, as discussed in Section 3.3.

3.4.2 Integration over the Field of View

The integration over the FOV takes into account that a real spectrometer has always finite extensions. The integration is described by Equation 3.25. The horizontal extension of *SCIAMACHY*'s FOV is approximately 40 km at the tangent point. Since trace gas concentrations are much more homogeneous in the horizontal direction than in the vertical direction, the horizontal FOV extension is neglected throughout this thesis. A more detailed discussion about horizontal inhomogeneities can be found in Section 7.2.3. Although the vertical extension is relatively small, errors may arise due to the strong vertical gradients of trace gas concentrations.

The occultation forward model implies the possibility to integrate vertically over the FOV. The FOV is separated into several height steps. For the investigations discussed in this section, the number of height steps was 20. The forward model results of all height steps are summarised and divided by the number of height steps. In Figure 3.9, deviations between forward modeling with and without integration over the FOV are presented as a function of tangent height for different wavelengths. It can be seen that the error due to the vertical FOV extension becomes relevant only for the troposphere and short wavelengths. The

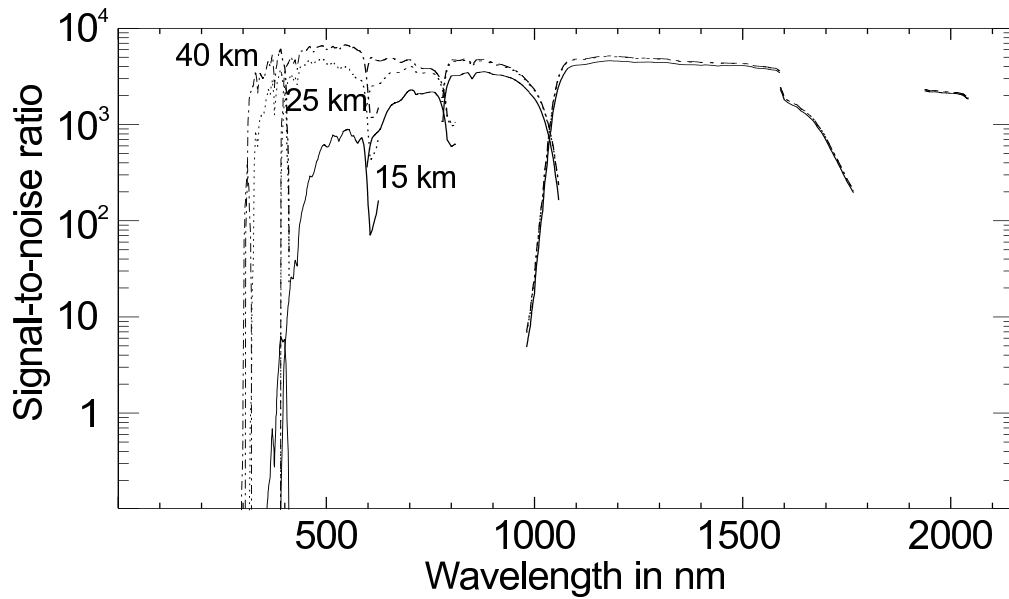


Figure 3.7: Signal-to-noise ratio in the SCIAMACHY wavelength range for several tangent heights and background aerosol conditions as estimated with the instrument simulator software.

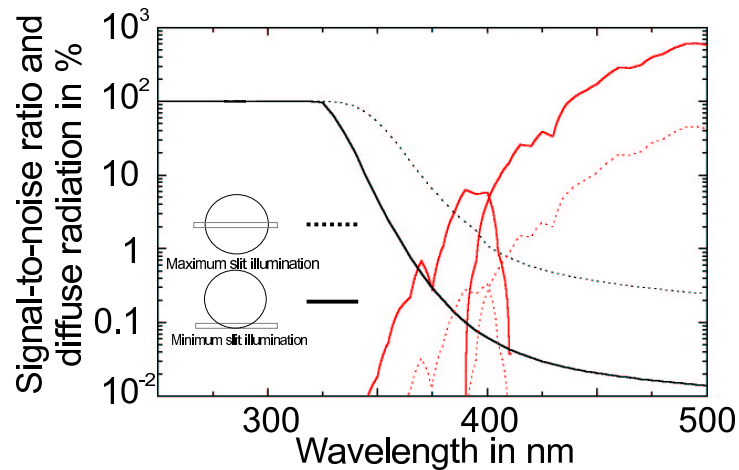


Figure 3.8: Signal-to-noise ratio of SCIAMACHY channel 2 and 3 (grey curves) and fraction of diffuse light (black curves) in the UV-vis spectral range for 10 km tangent height and moderate aerosol loading. Solid lines represent the case of maximum slit illumination and dashed lines an extremely low illumination.

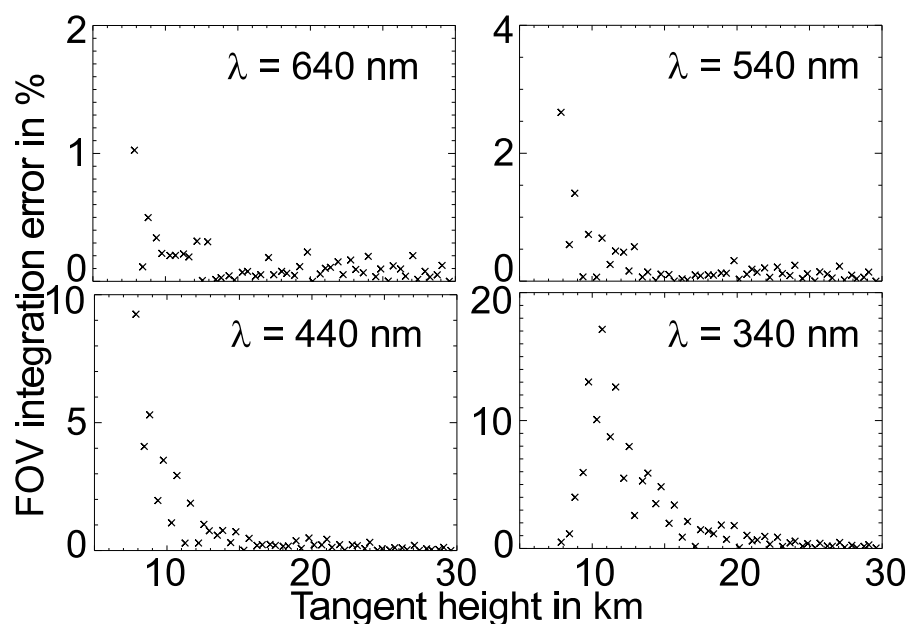


Figure 3.9: Errors due to the neglect of the vertical FOV extension for different wavelengths. Integrations over the FOV height are compared with a single model run.

clear increase can be explained by the strong ozone extinction. The values are not representing a smooth line. Single peaks and variations can be explained by the discrete nature of radiative transfer modeling.

So far, the retrieval results discussed in Chapter 5 are not affected by the neglect of the vertical FOV extension.

3.4.3 Conclusions

In this chapter, an introduction was given to the radiative transfer model used in the solar occultation retrieval. It was shown that the forward model is suitable for the complex requirements of trace gas profile retrieval. Furthermore, the forward model has been used for sensitivity studies. Section 3.4 highlights important limitations for profile retrieval in occultation geometry.

It was shown that the atmosphere becomes opaque in the UV wavelength region and for small tangent heights. The fraction of scattered light becomes nearly 100%, the signal-to-noise ratio breaks down, and atmospheric variability within the height extension of SCIAMACHY's field of view becomes significant. However, if occultation measurements have a sufficient signal-to-noise ratio, the assumption

of pure transmission will be true and the vertical field of view extension will be negligible in the context of radiative transfer modeling. Therefore, the integration over the FOV in Equation 3.25 can be simplified to an integration over the solar disk as it is already implemented.

Part II

Retrieval of Information about the Atmosphere

Chapter 4

The Inverse Problem

It is the central task of the inverse problem to solve the following equation for vector \mathbf{x} denoting trace gas vertical profiles or any other ensemble of parameters to be retrieved:

$$\mathbf{y} = \mathbf{A}(\mathbf{x}) + \boldsymbol{\epsilon}, \quad (4.1)$$

where \mathbf{y} contains the intensities, e.g. measured by SCIAMACHY, and operator \mathbf{A} stands for the non-linear forward model. $\boldsymbol{\epsilon}$ comprises all possible errors of measurement and radiative transfer calculation. In this formulation, Equation 4.1 describes the forward model introduced in Chapter 3. It is the way physical descriptions usually follow: assume a set of physical parameters and calculate other quantities with more or less sophisticated formulas. The forward calculation of radiative transfer is a simple job as well: Assuming an appropriate vertical profile \mathbf{x} , one can easily calculate the measurement vector \mathbf{y} . Matrix \mathbf{A} contains all the well-known information about radiative transfer for every wavelength λ and every height layer of the atmosphere.

The inverse calculation of vertical profiles from the radiance would be of the same simplicity if measurements were perfect and their information content sufficient. But in reality, all measurements come along with inaccuracies and the inverse problem is often ill conditioned, i.e. the information content is too small to find a definite solution. According to the information theory developed by Shannon [1949] and Yaglom and Yaglom [1983] the information content H of a measurement can be defined as

$$H = \frac{1}{2} \ln(\det(\mathbf{S}_a)) - \frac{1}{2} \ln(\det(\hat{\mathbf{S}})) \quad (4.2)$$

assuming a priori state vector \mathbf{x}_0 and measurement vector \mathbf{y} to be described by Gaussian probability density functions. \mathbf{S}_a and $\hat{\mathbf{S}}$ denote the corresponding covariance matrices of a priori and result vector, respectively. One task of trace

gas retrieval is to ensure that a measurement is capable of improving the a priori knowledge significantly. It is automatically implied by the eigenvector decomposition.

In any event, Equation 4.1 has to be approximated linearly by the first term of the Taylor series expansion:

$$\mathbf{y} = \mathbf{A}(\mathbf{x}) + \boldsymbol{\epsilon} \approx \mathbf{y}_0 + \mathbf{K}_0(\mathbf{x} - \mathbf{x}_0). \quad (4.3)$$

\mathbf{x}_0 is an a priori state vector as it is already discussed in Chapter 3 and \mathbf{y}_0 the corresponding measurement vector. \mathbf{K}_0 is a linearised forward model operator. Just inverting the matrix \mathbf{K}_0 is not useful due to uncertainties of measurement and forward model. Thus, there is a need of a priori knowledge \mathbf{x}_0 about the atmosphere from which it is possible to find the most likely solution iteratively.

A more detailed description of theoretical foundations of the occultation retrieval algorithm, which will be introduced in this chapter, was provided by Alexei Rozanov [Rozanov, 2001].

4.1 The Optimal Estimation Method

Most investigations described in this thesis were based on the optimal estimation method. It was first described in the context of remote sensing by Rodgers [1976, 1990]. Rodgers wrote also a book about the theoretical foundations [Rodgers, 1999]. The important results are presented here.

Starting point of the optimal estimation is Equation 4.3. Additionally, uncertainties of a priori knowledge and measurement errors have to be taken into account, to solve the inverse problem. They are introduced in the form of covariance matrices \mathbf{S}_a and \mathbf{S}_y , respectively. Minimisation of

$$\|(\mathbf{y} - \mathbf{y}_0) - \mathbf{K}_0(\mathbf{x} - \mathbf{x}_0)\|_{\mathbf{S}_y^{-1}}^2 + \|\mathbf{x} - \mathbf{x}_0\|_{\mathbf{S}_a^{-1}}^2 \quad (4.4)$$

leads then to an optimal estimation for the state vector \mathbf{x} :

$$\mathbf{x} = \mathbf{x}_0 + (\mathbf{K}_0^T \mathbf{S}_y^{-1} \mathbf{K}_0 + \mathbf{S}_a^{-1})^{-1} \mathbf{K}_0^T \mathbf{S}_y^{-1} (\mathbf{y} - \mathbf{y}_0). \quad (4.5)$$

Since the solution is based on a linear approximation, it might be necessary to repeat the calculation of \mathbf{x} iteratively. Iteration step $i + 1$ is given by

$$\mathbf{x}_{i+1} = \mathbf{x}_0 + (\mathbf{K}_i^T \mathbf{S}_y^{-1} \mathbf{K}_i + \mathbf{S}_a^{-1})^{-1} \mathbf{K}_i^T \mathbf{S}_y^{-1} (\mathbf{y} - \mathbf{y}_i + \mathbf{K}_i(\mathbf{x}_i - \mathbf{x}_0)). \quad (4.6)$$

After convergence, $\hat{\mathbf{x}}$ is the final retrieval result. The theoretical precisions s_j of the result are represented by the diagonal elements of covariance matrix $\hat{\mathbf{S}}$:

$$\hat{\mathbf{S}} = (\hat{\mathbf{K}}^T \mathbf{S}_y^{-1} \hat{\mathbf{K}} + \mathbf{S}_a^{-1})^{-1}. \quad (4.7)$$

With σ_j denoting the square root of the j -th diagonal element of $\hat{\mathbf{S}}$ and x_0^j as the a priori value of the j -th parameter to be retrieved, precisions are obtained by

$$s_j = \frac{\sigma_j}{x_0^j}. \quad (4.8)$$

Another frequently used quantity is the so-called averaging kernel matrix $\hat{\mathbf{A}}_k$. It is defined as

$$\hat{\mathbf{A}}_k = \frac{\partial \hat{\mathbf{x}}}{\partial \mathbf{x}_t}, \quad (4.9)$$

where \mathbf{x}_t is the unknown true state vector. The averaging kernels are a measure of the impact of \mathbf{x}_t on the retrieved state $\hat{\mathbf{x}}$. Each row of the kernel matrix represents one height layer of the retrieved state, the columns indicate the influence of each height layer of the true state. $\hat{\mathbf{A}}_k$ is also deduced in the framework of the optimal estimation method, where it is expressed by

$$\hat{\mathbf{A}}_k = \underbrace{(\hat{\mathbf{K}}^T \mathbf{S}_y^{-1} \hat{\mathbf{K}} + \mathbf{S}_a^{-1})^{-1}}_{=\hat{\mathbf{S}}} \hat{\mathbf{K}}^T \mathbf{S}_y^{-1} \hat{\mathbf{K}}. \quad (4.10)$$

In an ideal case, the averaging kernel matrix is expected to be a unit matrix. However for real experimental setups, the rows of $\hat{\mathbf{A}}_k$ are peaked with a finite width. The width of the peaks are a measure for the vertical resolution of the retrieval.

4.2 The Eigenvector Decomposition

A solution obtained by the eigenvector decomposition is characterised by a set of eigenvectors $\boldsymbol{\psi}_{i,k}$ which span the state space:

$$\mathbf{x}_{i+1} - \mathbf{x}_0 = \sum_{k=1}^{N_i} \beta_{i,k} \boldsymbol{\psi}_{i,k}. \quad (4.11)$$

It is the solution of iteration step $i + 1$, where $\beta_{i,k}$ denotes the eigenvalues of all fit parameters and \mathbf{x}_0 the a priori model state vector. It is an important feature of this method that N_i is the number of only those parameters about which the measurement contains significant information. The number of relevant fit parameters can be obtained as already described by Hoogen et al. [1999]. According to Equation 4.2, the information content H can be expressed by a so-called information operator \mathbf{P} and its eigenvalues λ_k , respectively:

$$H = \frac{1}{2} \ln(\det(\mathbf{P} + \mathbf{I})) = \frac{1}{2} \sum_k \ln(\lambda_k + 1) \quad (4.12)$$

where \mathbf{I} is the unity operator and \mathbf{P} is defined by

$$\mathbf{P} = \mathbf{S}_a \hat{\mathbf{K}}^T \mathbf{S}_y^{-1} \hat{\mathbf{K}}. \quad (4.13)$$

Its eigenvalues λ_k are given by

$$\mathbf{P}\boldsymbol{\psi}_k = \lambda_k \boldsymbol{\psi}_k. \quad (4.14)$$

In the scalar case of one parameter, Equation 4.13 could be read as the scalar fraction of measurement error and a priori error. If the quotient was smaller than one, the measurement would not improve the information on the state vector. Thus, eigenvalues λ_k larger than one indicate significant measurement information about parameter k . Only these are used in the further fit process. For the next step it is necessary to introduce a new basis for the state space

$$\boldsymbol{\phi}_k = \hat{\mathbf{K}}^T \mathbf{S}_y \hat{\mathbf{K}} \boldsymbol{\psi}_k \quad (4.15)$$

with biorthogonal properties of $\boldsymbol{\psi}_k$ and $\boldsymbol{\phi}_k$:

$$\langle \boldsymbol{\phi}_k, \boldsymbol{\psi}_l \rangle = \delta_{kl} n_k. \quad (4.16)$$

It can now be shown that $\beta_{i,k}$ is given in the least squares sense of the optimal estimation by

$$\beta_{i,k} = \frac{\lambda_{i,k}}{n_{i,k}(1 + \lambda_{i,k})} \boldsymbol{\psi}_{i,k}^T \mathbf{K}_i^T \mathbf{S}_y^{-1} (\mathbf{y} - \mathbf{y}_i + \mathbf{K}_i(\mathbf{x}_i - \mathbf{x}_0)). \quad (4.17)$$

4.3 Application to Occultation

4.3.1 Formulations

For spectroscopic measurements of atmospheric constituents in occultation geometry, the retrieval is based on the linearised iterative approach of Equations 4.6 and 4.11, respectively. In Appendix E, the retrieval algorithm is illustrated by a flowchart.

Elements of the state vectors \mathbf{x}_0 and \mathbf{x} are defined as concentrations N_j for each height layer h_i and each considered trace gas j :

$$\mathbf{x}_0 = \begin{pmatrix} N_1(h_1) \\ \vdots \\ N_1(h_L) \\ \vdots \\ N_J(h_1) \\ \vdots \\ N_J(h_L) \end{pmatrix} \quad \text{and} \quad \mathbf{x} = \begin{pmatrix} \delta N_1(h_1) + N_1(h_1) \\ \vdots \\ \delta N_1(h_L) + N_1(h_L) \\ \vdots \\ \delta N_J(h_1) + N_J(h_1) \\ \vdots \\ \delta N_J(h_L) + N_J(h_L) \end{pmatrix} \quad (4.18)$$

with J as the total number of considered trace gases and L the total number of height layers. For computational reasons, a parameter vector \mathbf{p} is defined containing the relative deviations from the a priori concentrations $N_j(h_i)$:

$$\mathbf{p} = \begin{pmatrix} N_1(h_1)/\delta N_1(h_1) \\ \vdots \\ N_1(h_L)/\delta N_1(h_L) \\ \vdots \\ N_J(h_1)/\delta N_J(h_1) \\ \vdots \\ N_J(h_L)/\delta N_J(h_L) \end{pmatrix}. \quad (4.19)$$

The measurement vectors \mathbf{y} and \mathbf{y}_0 are conceived in the same way:

$$\mathbf{y}_0 = \begin{pmatrix} \Upsilon(\psi_1, \lambda_1) \\ \vdots \\ \Upsilon(\psi_1, \lambda_\Lambda) \\ \vdots \\ \Upsilon(\psi_K, \lambda_1) \\ \vdots \\ \Upsilon(\psi_K, \lambda_\Lambda) \end{pmatrix} \quad \text{and} \quad \mathbf{y} = \begin{pmatrix} \Upsilon(\psi_1, \lambda_1) + \delta\Upsilon(\psi_1, \lambda_1) \\ \vdots \\ \Upsilon(\psi_1, \lambda_\Lambda) + \delta\Upsilon(\psi_1, \lambda_\Lambda) \\ \vdots \\ \Upsilon(\psi_K, \lambda_1) + \delta\Upsilon(\psi_K, \lambda_1) \\ \vdots \\ \Upsilon(\psi_K, \lambda_\Lambda) + \delta\Upsilon(\psi_K, \lambda_\Lambda) \end{pmatrix}. \quad (4.20)$$

Λ is the total number of wavelengths λ and K is the total number of tangent heights or solar zenith angles ψ . Intensity Υ is given by Equation 3.25. Throughout this thesis, only transmissions are used in the retrieval algorithm. In most cases, weakly wavelength dependent features such as Rayleigh scattering are removed by subtraction of a low order polynomial.

Formally, the intensity variation $\delta\Upsilon$ can be related to the variation of atmospheric parameters δp_j by

$$\delta\Upsilon(\psi, \lambda_i, \mathbf{p}) = \sum_{j=1}^J \int_{h_b}^{h_t} W_j(\psi, \lambda, \bar{\mathbf{p}}) \delta p_j(h') dh', \quad (4.21)$$

where $\bar{\mathbf{p}}$ denotes the parameter vector under a priori conditions. The integration over height h is performed from the bottom h_b to the top h_t of atmosphere. W_j are the so-called weighting functions. They are the elements of matrix \mathbf{K}_0 in Equation 4.3 describing the intensity variation $\delta\Upsilon$ with respect to variations of atmospheric parameters δp_j :

$$W_j(\psi, \lambda, \bar{\mathbf{p}}) = \left. \frac{\delta\Upsilon(\mathbf{p})}{\delta p_j} \right|_{\bar{\mathbf{p}}}. \quad (4.22)$$

For trace gas retrieval, the weighting functions W_j are the derivatives of measured intensity Υ with respect to relative trace gas concentrations p_j . From Equations 3.2, 3.23, and 3.25, it can be seen how $\delta\Upsilon$ is obtained. The derivation of Equation 3.25 with respect to trace gas number densities N_j leads to

$$\delta\Upsilon(\psi, \lambda, \beta) = - \int_{h_b}^{h_t} dh' \delta N_j \int_{\Omega} d\omega \frac{f(\omega)}{\cos \tilde{\psi}(h', \omega)} \chi(\psi, h', \omega) \int_{\Delta\lambda} d\lambda' a(\lambda, \lambda') I_0(\lambda', \beta) e^{-\tau_j(\psi, \omega, \lambda')} \sigma_j(\lambda'), \quad (4.23)$$

changing the order of integration and pulling down the integration over the path length, which was only performed for calculation of optical depth τ before (Equation 3.23). Comparing Equations 4.21 and 4.23, the following expression is obtained for the weighting function of trace gas j :

$$W_j(\psi, \lambda, \mathbf{p}(h')) = - \int_{\Omega} d\omega \frac{f(\omega) \chi(\psi, h', \omega)}{\cos \psi(\tilde{h}', \omega)} \int_{\Delta\lambda} d\lambda' a(\lambda, \lambda') I_0(\lambda') e^{-\tau_j(\psi, \omega, \lambda')} \sigma_j(\lambda', h'). \quad (4.24)$$

For numerical reasons, it is necessary to make the variable h' discrete in the equations above. Hence, Equation 4.21 becomes

$$\delta\Upsilon(\psi, \lambda, \bar{\mathbf{p}}) = \sum_{j=1}^J \sum_{i=1}^L \tilde{W}_{ji}(\psi, \lambda, \bar{\mathbf{p}}) \frac{\delta N_j(h_i)}{N_j(h_i)} q_i \quad (4.25)$$

with q_i as discrete values of $\delta h'$, which depends on the integration rule. Note, that \tilde{W}_{ji} is now appropriate to relative variations of parameters \mathbf{p} .

The linearised forward model operator \mathbf{K}_0 from Equation 4.3 can now be written for occultation trace gas retrieval:

$$\mathbf{K}_0 = \begin{pmatrix} \tilde{W}_{11}(\psi_1, \lambda_1) q_1 & \dots & \tilde{W}_{ji}(\psi_1, \lambda_1) q_i & \dots & \tilde{W}_{JL}(\psi_1, \lambda_1) q_L \\ \vdots & & \vdots & & \vdots \\ \tilde{W}_{11}(\psi_1, \lambda_\Lambda) q_1 & \dots & \tilde{W}_{ji}(\psi_1, \lambda_\Lambda) q_i & \dots & \tilde{W}_{JL}(\psi_1, \lambda_\Lambda) q_L \\ \vdots & & \vdots & & \vdots \\ \tilde{W}_{11}(\psi_K, \lambda_1) q_1 & \dots & \tilde{W}_{ji}(\psi_K, \lambda_1) q_i & \dots & \tilde{W}_{JL}(\psi_K, \lambda_1) q_L \\ \vdots & & \vdots & & \vdots \\ \tilde{W}_{11}(\psi_K, \lambda_\Lambda) q_1 & \dots & \tilde{W}_{ji}(\psi_K, \lambda_\Lambda) q_i & \dots & \tilde{W}_{JL}(\psi_K, \lambda_\Lambda) q_L \end{pmatrix} \quad (4.26)$$

Measurement errors are taken into account by covariance matrix \mathbf{S}_y representing the measurement noise for each measurement and wavelength. Usually, it is a diagonal matrix, i.e. the errors are assumed to be uncorrelated. The a priori

covariance matrix \mathbf{S}_a reflects the uncertainties of the a priori height profiles. It is a block diagonal matrix, where correlations are assumed to be found only between adjacent height layers of the same species. The off-diagonal elements within each block are approximated by

$$\mathbf{S}_{a,j} = \sigma_{j,i'}\sigma_{j,i''}e^{-\frac{|h_{i'}-h_{i''}|}{h_c}} \quad (4.27)$$

Index j denotes trace gas number or number of diagonal block, h_c is the correlation length, and $\sigma_{j,i'}/i''$ are the variances of trace gas concentrations at height levels $h_{i'}$ and $h_{i''}$, respectively. An appropriate value for h_c is for example 5 km in the case of ozone [Hoogen et al., 1999].

4.3.2 Regularisation

Real retrieval solutions of atmospheric parameters are often characterised by strong variabilities, which cannot be explained by real atmospheric features. A “first order” regularisation is automatically involved by including the a priori information, as described in Section 4.1. The relative strength of the regularisation is weighted by the covariance matrices \mathbf{S}_a and \mathbf{S}_y . However, even if the matrices contain reasonable estimations of errors and uncertainties, instable solutions will not be avoided in all cases.

The retrieval algorithms introduce more sophisticated constraints on the solution. They are based on considerations that were first published in [Tikhonov, 1963] and [Twomey, 1963]. The method is known as Twomey-Tikhonov regularisation. The aim is to modify the inverse of the a priori covariance matrix \mathbf{S}_a such that the estimated solution is forced into a more “realistic” shape. Of course, the constraints should be as weak as possible and as strong as necessary. Otherwise, the solution will suffer from unrealistic features or will lose measurement information, respectively. In the case of occultation retrievals, the optimal regularisation parameters result in stable retrieval run at least for ozone and NO₂.

Looking at Equations 4.4 and 4.5, it can be shown that the diagonal elements of \mathbf{S}_a^{-1} are a direct weighting of the a priori parameter values. The off-diagonal elements can be used to take first and higher order derivatives of the a priori values into account. A nice introduction to this idea is also given in [Rodgers, 1999]. In the case of the occultation retrieval algorithms, two “Tikhonov parameters” T_1^j and T_2^j are used for each trace gas j . The first one enhances the direct influence of the a priori parameters replacing the diagonal elements of \mathbf{S}_a^{-1} by the chosen parameter T_1^j . The second parameter is intended for the first derivatives of the a priori parameter values, i.e. the smoothness of the estimated profiles. A matrix \mathbf{R}_j , which accounts for the deviation of the a priori state vector \mathbf{x}_0 with respect

One of the three wavelength scales is kept fixed. The others are fitted out with new wavelengths λ^* defined on the basis of the old wavelengths λ and two fit parameters a and b :

$$\lambda^* = \lambda - a - (\lambda - \bar{\lambda})(b - 1). \quad (4.31)$$

a is the “shift” parameter and b is the “squeeze” parameter. $\bar{\lambda}$ is the centre of the wavelength interval. The shift and squeeze can be performed individually for each wavelength window. Furthermore, there is the possibility of shifting the whole window or only individual components.

Chapter 5

Trace Gas Vertical Profiles

The driving force behind most of the projects investigating the atmosphere is the increasing anthropogeneous impact and observed changes such as global warming and the ozone hole. Dozens of artificial compounds are emitted into the atmosphere and disturb the natural chemical equilibrium. Ozone and its destruction cycles play a key role in the troposphere as well as in the stratosphere. Nitrogen dioxide concentrations are mainly caused by combustion processes. Nitrogen compounds are important for ozone chemistry. In this chapter, retrieval results of trace gas concentrations are presented. Most of the background information has been taken from much more detailed discussions in [Brasseur et al., 1999, Seinfeld and Pandis, 1998]. A review focussing on stratospheric ozone depletion can be found in [Solomon, 1999].

5.1 Retrieval Process

Retrieval of vertical concentration profiles is a very complex and sophisticated task. It is a long process chain transforming the SCIAMACHY occultation measurements to trace gas profiles provided for further use in the scientific community. An overview of the data processing is depicted as a flowchart in Figure 5.1. The data evaluation starts in the ESA ground segment after data reception from ENVISAT. The uncalibrated data are separated orbit-wise and written to level 0 data files [Lützow-Wentzky and Demuth, 2001]. The first important data processing step is the level 0 to 1b conversion [Balzer et al., 2000]. It is primarily a reorganisation of the measurement data as well as a calculation of all required calibration parameters [Slijkhuis et al., 1997]. Actual data calibrations such as pixel-to-wavelength mapping, polarisation correction, dark current correction etc. are performed in the next processing step from level 1b to 1c [Slijkhuis and Balzer, 2000]. The conver-

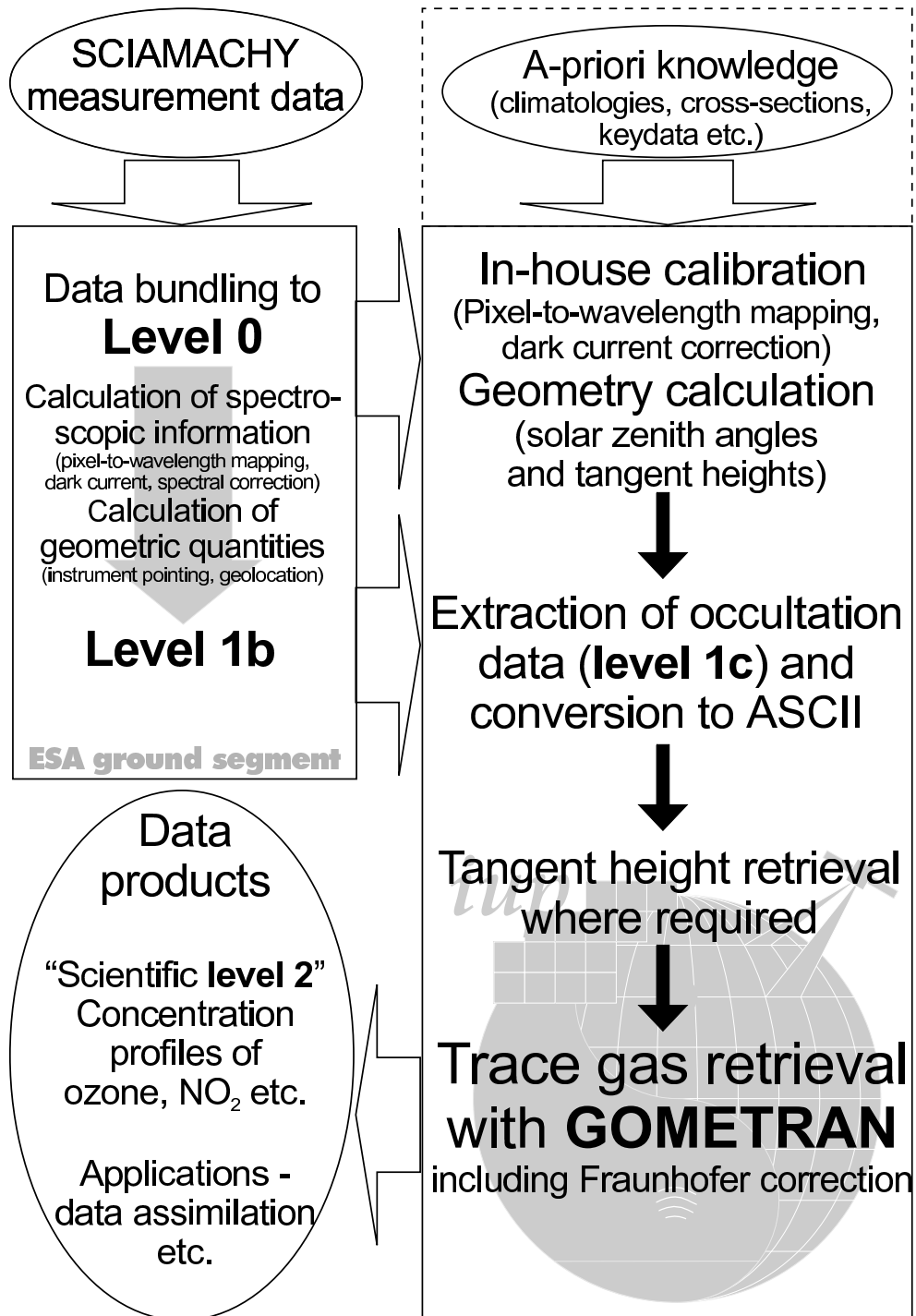


Figure 5.1: SCIAMACHY occultation data processing. The GOMETRAN retrieval algorithm is introduced in Chapter 3 and Chapter 4. A schematic view can be found in Appendix E.

sion to level 1c is usually applied by the data user. At the same time, the desired sub-data structures, e.g. the occultation data sets, are extracted. The level 0 to 1b processing can partly be performed at the Institute of Environmental Physics. The in-house processing has been a very helpful alternative to the official data supply.

At this point, the data are ready for scientific processing, i.e. the actual retrieval process as introduced in Chapter 3 and Chapter 4. Since the geometry calculations (solar zenith angle, tangent height etc.) have been unreliable as shown in Chapter 6, it is sometimes necessary to perform a tangent height retrieval. This issue is part of this work and will be discussed in Section 6.1. Another important problem is the improvement of information about the pointing on the solar disk, which is also referred to as Fraunhofer correction in this thesis. The theoretical foundations of the retrieval are discussed in Chapter 3 (forward model) and Chapter 4 (retrieval) as well as in [Rozanov et al., 1997, 2002].

A priori vertical concentration profiles as well as information on pressure and temperature are taken from the US-standard profiles [NASA, 1976] and model calculations from the Max-Planck-Institut, Mainz [Brühl and Crutzen, 1991]. Cross sections of trace gases are either calculated with the so-called line-by-line method or taken from measured moderate resolution cross section spectra such as [Bogumil et al., 1999] and [Burrows et al., 1998]. Measured cross sections are commonly used in the UV-vis wavelength range. The fine spectral structures of O₂, H₂O, and typical infrared absorbers need to be simulated with the line-by-line method. Optical properties for the line-by-line calculations are taken from the HITRAN database [Rothman et al., 1998].

5.2 Ozone

5.2.1 Background

In 1930, Sidney Chapman described the foundations of the stratospheric ozone chemistry in a theoretical work [Chapman, 1930]. In his honour, the four basic ozone reactions are called the Chapman cycle. They describe formation and destruction of ozone (O₃) due to UV irradiation. High energy photons with wavelengths less than 242nm dissociate molecular oxygen O₂:



The produced oxygen atoms O are highly reactive and form ozone rapidly with surrounding oxygen molecules:



An additional molecule M , e.g. N_2 , is needed to conserve energy and momentum at the same time. O_3 can be decomposed by incident radiation with wavelengths smaller than 320 nm:



Another destruction channel is given by



The ozone profile illustrated in Figure 3.2 is mainly formed by the equilibrium of these reactions. Catalytic destruction cycles also play an important role. One example is the so-called NO_x -cycle discussed in Section 5.3. The resulting ozone peak in the stratosphere is also known as the ozone layer, which protects the biosphere against severe UV radiation. Therefore, it is understood that one focus of spaceborne spectroscopy is the generation of global ozone maps. Due to its relatively high abundance and cross sections, ozone is easy to detect and height-resolved profiles can be seen as standard retrieval product. After ratification of the Montreal protocol from 1987 and 1996, emissions of CFCs dropped significantly. Since CFCs are suspected to cause the observed increase of the ozone hole events, they are completely prohibited in industrial countries and will be abolished worldwide in 2006. However, it is still a challenging question how the ozone layer will develop in the next decades as anthropogenic emissions of CFCs take roughly one decade to climb into the stratosphere. Furthermore, it is not clear if the global warming due to green house gases will lead to a stratospheric cooling, which would result in stronger ozone destruction.

Ozone also plays a key role in the complex chemistry of the troposphere. In particular, it is interesting in local events such as urban pollution etc. However, the abundance in the troposphere is only 10% of the total ozone loading. Hence, it is much more difficult to quantify tropospheric ozone accurately through the ozone layer from space as it resides below the ozone layer.

5.2.2 Retrieval Results

Ozone is one of the strongest absorbers in the UV-vis wavelength range. The cross sections of ozone (see Appendix B) are comparable to most of the other trace gases. However due to its relatively high abundance especially in the stratosphere, O_3 is one of the strongest absorbers in the atmosphere. It is so strong that the Hartley-Huggins absorption bands make the atmosphere opaque for UV radiation. Since the occultation measurement strategy is based on transmitted radiation, it is impossible to choose a spectral fitting window in the UV range (see also the discussions in Chapter 3). Only at high altitudes above the ozone layer, it becomes

meaningful to consider the Hartley-Huggins absorption bands. Throughout the studies of this section, the Chappuis bands in the visible wavelength region have been used in the retrieval process. The fitting window used in this study covers the spectral range from 520 to 595 nm. This window includes the strongest regions of the Chappuis bands and matches the sensitive range of SCIAMACHY channel 3, which ends at 620 nm.

There is also a clear differential structure in the cross sections, which is very important due to the subtraction of a low order polynomial. One of the major reasons for the need of a polynomial subtraction is explained in some detail in Section 6.2. In the case of ozone retrievals, a polynomial of the order of 3 is fitted to the transmission data. In order to obtain smooth vertical concentration profiles, the Twomey-Tikhonov regularisation (see Section 4.3.2) is usually applied. Appropriate Tikhonov parameters are $T_1 = 10^3$ and $T_2 = 10^4$.

In Figure 5.2, a retrieved ozone profile is plotted in comparison with indepen-

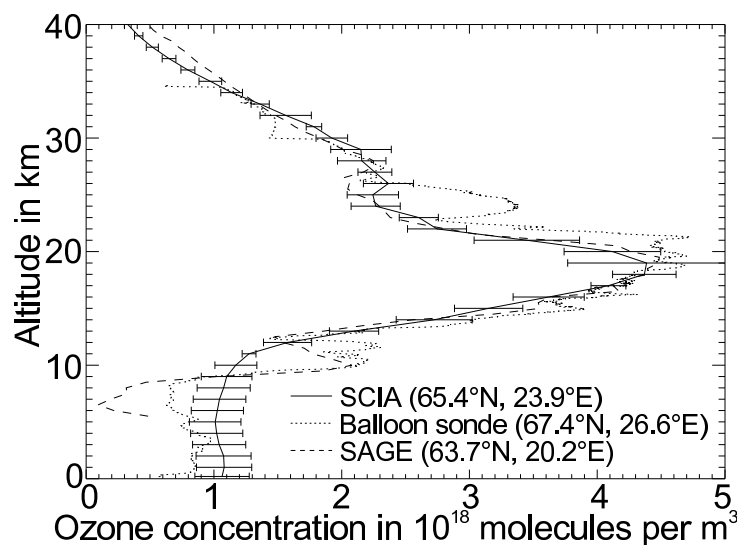


Figure 5.2: Solid line: Vertical concentration profile of ozone retrieved from SCIAMACHY solar occultation measurements on September 22, 2002. The dashed line is a corresponding retrieval result from SAGE-II. The dotted line represents a balloon measurement over Sodankylä, Finland.

dent results from SAGE-II occultation measurements (dashed line) and balloon-borne measurements over Sodankylä (dotted line). Statistical errors obtained by Equation 4.7 are indicated by the error bars. The balloon sonde measurements were performed by Kyrö [2002]. The SAGE results have been downloaded from the

internet*. The overall agreement is quite good though some of the profile features are not matched by the retrieval results. Since ozone sondes perform direct in-situ measurements, their vertical resolution of approximately 10 m is much higher than that of spaceborne instruments. Furthermore, balloons encounter all local variabilities in horizontal direction, whereas spaceborne measurements have to be considered as an average over a relatively large atmospheric volume. The small ozone peak between 10 and 12 km has not been retrieved from the SCIAMACHY measurements as the considered height range ends here. Therefore, the information content was too small to have a significant influence on the result. All values below 10 km that are shown here are only based on the a priori knowledge of the applied climatologies. Similarly, the values above 40 km make towards the a priori ozone profile as the information content of the corresponding measurements decreases rapidly with height. An appropriate height range for trace gas retrievals can be estimated from the averaging kernels, which have been introduced in Section 4.1. In Figure 5.3, five selected averaging kernels are plotted as a function of

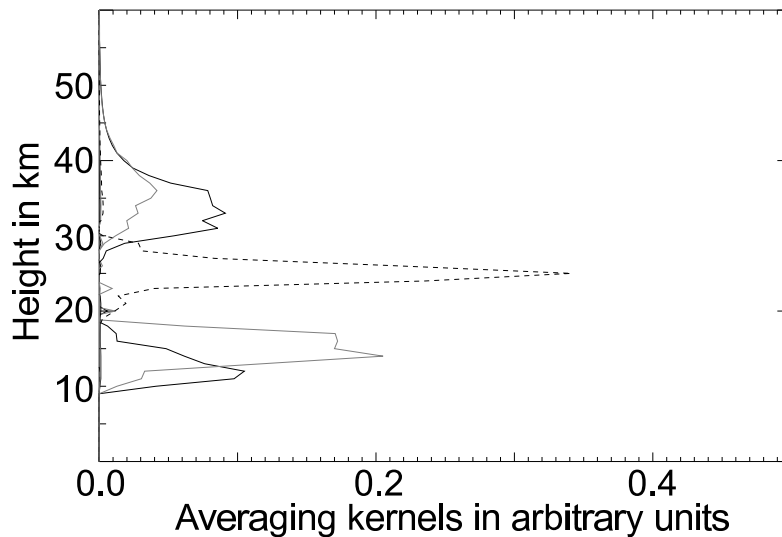


Figure 5.3: Averaging kernels for ozone at 10, 15, 25, 35, and 40 km covering the region of interest. The spectral range corresponds to the combined ozone/ NO_2 retrieval with fitting windows from 420 to 460 nm and 520 to 595 nm.

height. The kernels are automatically calculated within the retrieval process. Of course, there are values in the kernel matrix for each height layer. Here, the focus is on the layers at 10, 15, 25, 35, and 40 km as it gives a clear overview of the

*SAGE-II provides the longest record of satellite high-resolution profile measurements (see also Section 2.3.7). Recently, the SAGE-II data version 6.2 was released. Data can be downloaded at <http://www-sage2.larc.nasa.gov/data/>

retrieval characteristics. They are indicated by solid grey and black lines as well as by a dashed black line, respectively. The peak values of the averaging kernels indicate the height layer of the true state with the most significant impact on the retrieved concentration. The peak width is a measure for the vertical resolution of the retrieval result. It can be seen that there are clear peaks throughout the height range between 10 and 40 km. Around the ozone maximum, the peaks of the averaging kernels become more significant, i.e. the theoretical height resolution increases to approximately 3 km and the retrieval results are more strongly related to the true concentration values. Furthermore, it means that the influence of the a priori profile has a minimum in this region. Towards 40 km, the impact of the measurement on the result begins to decrease again with a corresponding decrease of the height resolution.

The information cut off at 10 km during standard retrievals is due to the need of a stable fitting range for the evaluation of long time series, where occasional atmospheric events such as cloud coverage and a problematic solar pointing might impede a reliable retrieval at low tangent heights. Nevertheless, considering single ozone retrievals, it will certainly be possible to perform ozone fits also in the troposphere as the spectral signal is strong enough. A detailed study about the capabilities of ozone retrievals at extremely low tangent heights is still missing. A detailed error analysis can be found in Chapter 7.

Results of the spectral fit within the same retrieval process are exemplarily shown in Figure 5.4. The transmission as obtained from the occultation measurements are plotted with a solid line vs. wavelength in the ozone fitting window mentioned above. The dotted line represents the results of the forward modeling after the last retrieval iteration. Figure 5.4 presents the evaluation of the measurement at one of the lowermost tangent heights at 13 km. It can clearly be seen that the differential structure of ozone absorption is accurately fitted.

The difference between model and measurement spectra is called residual. The residual of the spectral fit in Figure 5.4 is plotted in Figure 5.5. The physical unit of the spectral fit and its residual is given on the same scale as the transmission. The residual represents all those components of the spectral structure that are not addressed properly by the forward model. In an ideal case of a perfect forward model, the residual should reflect the signal-to-noise ratio of the instrument. It can be seen that the residual is by one order of magnitude smaller than the corresponding spectral structure, which is quite a good fitting result. On the transmission scale ranging from 0 to 1, the residual corresponds to an error of less than one percent. This is still a bit higher than one would expect from the signal-to-noise ratio (see Section 3.4.1) though the residual plot already looks quite noisy. Other sources of signals in the residual as well as results of first ozone validations are discussed in Chapter 7.

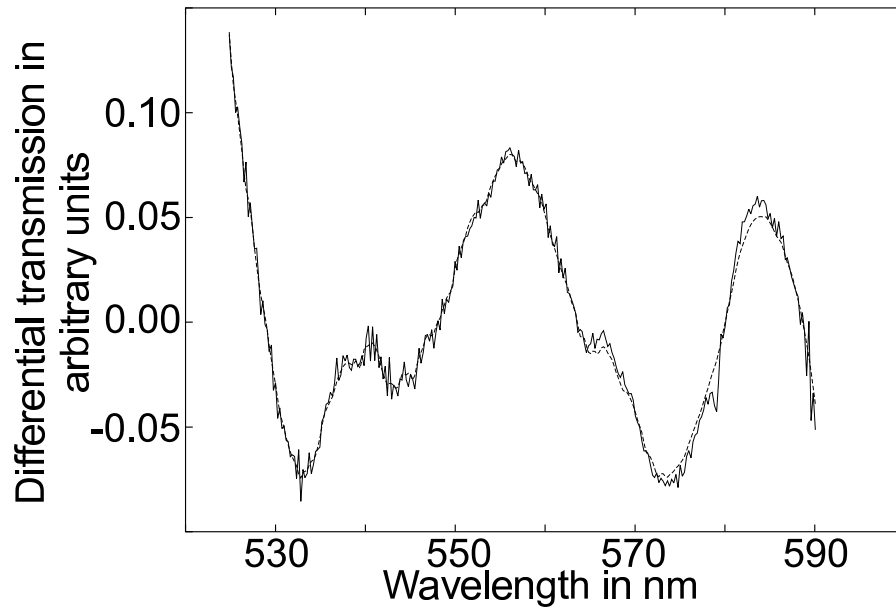


Figure 5.4: Spectral fit in the ozone fitting window at 13 km tangent height corresponding to the retrieval result in Figure 5.2. Solid line: Transmission spectra. Dotted line: Forward model fit.

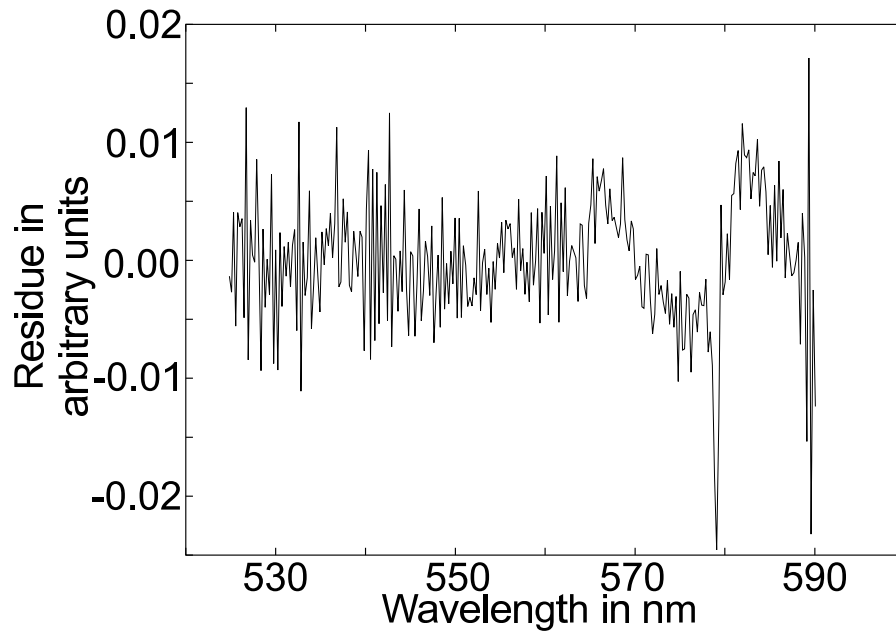


Figure 5.5: Residual of the spectral fit in Figure 5.4.

5.3 Nitrogen Dioxide

5.3.1 Background

Nitrogen oxides are important reactants in the troposphere as well as in the stratosphere. In the troposphere, the main source of NO_x [†] is the emission from natural and anthropogenic combustion processes. The principal natural source in the stratosphere is N_2O . It is emitted by biological sources on the surface. The residence time is long enough for rising up into the stratosphere, where it is photolysed to NO and N_2 via



In the stratosphere, the so-called NO_x cycles are two of the most important catalytic destruction cycles of ozone. They were first described by Crutzen [1970] and Johnston [1971]. The general reaction scheme can be written as follows, where X stands for possible classes of catalysts such as hydrogen, chlorine, bromine etc.



resulting in the net reaction



For the case of nitrogen oxides, X has to be replaced by NO . NO_2 can be removed by photolysis:



In terms of occultation measurements, the reaction of Equation 5.10 is responsible for strong horizontal gradients, which are difficult to resolve within the retrieval algorithm. Measurement errors due to the diurnal cycle of certain species will be discussed in Section 7.2.3. In the second NO_x cycle, NO_2 reacts with O_3 forming NO_3 . NO_3 is rapidly removed by photolysis. The complete cycle is



which results also in a net destruction of ozone:



[†] NO and NO_2 are often referred to as NO_x .

In the troposphere, a variety of similar reactions take place due to the presence of many additional trace gases. In addition to other gases, NO_x emissions are also responsible for acid rain.

Due to the high cross sections of NO_2 in the UV-vis wavelength range (see Appendix B), NO_2 is relatively easy to detect. Like ozone, it is nowadays a standard retrieval product of satellite measurements. Usually, it is sufficient to measure only one particular species of the NO_x family as their concentrations are closely related.

5.3.2 Retrieval Results

Like ozone, NO_2 shows significant absorption in the UV and visible wavelength range. See Appendix B for details of the cross sections. However, due to the much smaller abundance of NO_2 compared to ozone, it is useful to focus strictly on the region of maximum absorption cross sections. The spectral fitting window used in the NO_2 studies ranges from 420 to 460 nm. It matches also the sensitive detector region of channel 3, which starts at 394 nm. Furthermore, the spectra are well supplied with differential structures of NO_2 . A limiting factor is the rapidly decreasing signal-to-noise ratio towards the UV range, which is discussed in Chapter 3.

It turns out that a simultaneous fit of ozone and NO_2 is quite suitable for the spectral properties of both species. On the one hand, it is comfortable to retrieve both at the same time for standard data products. On the other hand, the spectral signals of both gases interfere significantly in the NO_2 fitting window. The information content about NO_2 is clearly smaller than that about ozone. Therefore, it is necessary to apply different regularisation parameters. So far, best results were obtained with $T_1 = 50$ and $T_2 = 50$. The subtraction polynomial is the same with an order of 3.

Figure 5.6 shows the results of the NO_2 vertical profile retrieval from the same retrieval run as in Section 5.2. Again, it is compared to corresponding results from the SAGE-II instrument. The agreement is even better than in the case of ozone. Details of the error analysis and validation can be found in Chapter 7. Figure 5.7 shows the NO_2 averaging kernels obtained within the retrieval. Like in the case of the O_3 kernels, the plot is reduced to the height layers at 10, 15, 25, 35, and 40 km. The results are quite similar to the O_3 averaging kernels. An important difference can be observed at 10 km, where the impact of the true profile has almost vanished. Standard retrievals of NO_2 are possible in the range between 13 and 40 km. The maximum information content of the measurements with respect to NO_2 is between 20 and 30 km. However, there have already been successful retrieval fittings at tangent heights below 13 km. It is an indication that

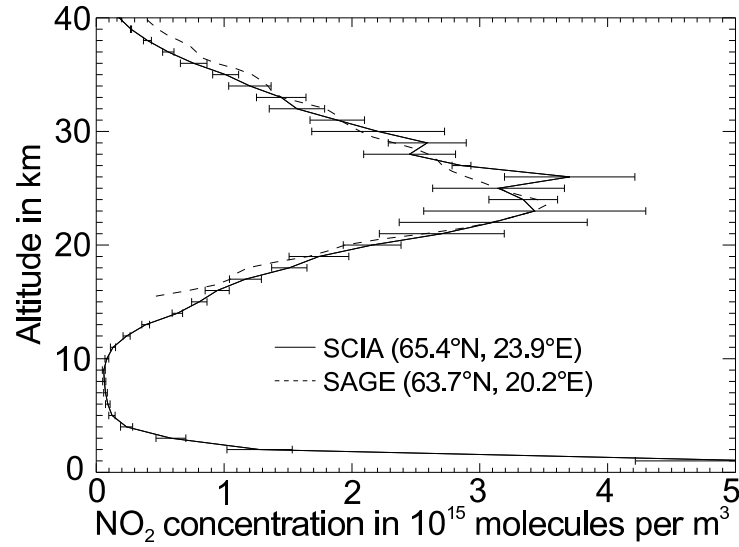


Figure 5.6: NO_2 vertical concentration profile retrieved from SCIAMACHY occultation measurements (solid line) in comparison to SAGE-II results (dashed line). The error bars indicate the theoretical precisions as estimated by the optimal estimation. Measurements were made on September 22, 2002.

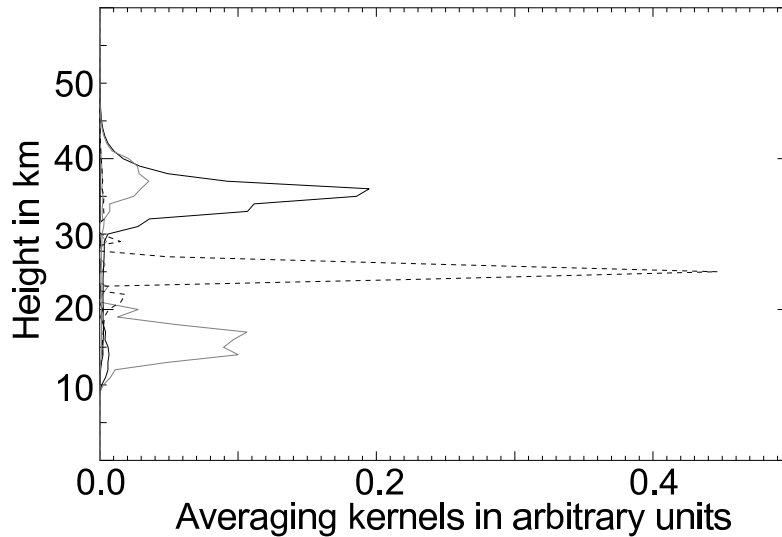


Figure 5.7: Averaging kernels for NO_2 at 10, 15, 25, 35, and 40 km covering the region of interest. The spectral range corresponds to the combined ozone/ NO_2 retrieval with fitting windows from 420 to 460 nm and 520 to 595 nm.

NO₂ measurements are possible even down to the troposphere. In Section 8.2.3, it is discussed how the evaluation can be improved in future.

In Figure 5.8, the same spectral fit as in Section 5.2 is plotted for the NO₂ fitting window and a tangent height of 13 km. Again, the measured transmission spectrum is represented by the solid line, whereas the dotted line gives the forward model fit after the last retrieval iteration. The agreement between measurement and model is remarkable as the NO₂ absorption signal suffers from a rapidly decreasing signal-to-noise ratio at low tangent heights (see Section 3.4.1). The fit residual of the spectral fit is shown in Figure 5.9. It can be seen that the relative model errors are in the order of one percent, which is already quite close to the expectations from the signal-to-noise ratio. A strong peak is located around 434 nm. The peak can be explained by the strong H_γ Fraunhofer line. The matching algorithm introduced in Section 6.2.3 was switched off for these standard retrievals in order to save computation time. In Section 7.1.1, it is shown how the Fraunhofer lines are significantly reduced, especially the H_γ line in the NO₂ fitting window.

5.4 Oxygen

5.4.1 Background

Molecular oxygen is the second most abundant gas of the atmosphere (see Section 3.1). Therefore and in contrast to all other gases in this chapter, it cannot be regarded as trace gas. It is highly reactive due to its strong electronegativity, especially the so-called odd oxygen forms O and O₃. Hence, oxygen is involved in almost all important chemical reactions in the troposphere as well as in the stratosphere. Even the metabolic reactions of animals and plants depend directly on oxygen.

From a scientific point of view, it is not very interesting to retrieve height-resolved profiles of oxygen. It is even more time-consuming to retrieve O₂ as the cross sections are dominated by hundreds of narrow lines, which have to be calculated separately. However, O₂ is a well-mixed constituent and its mixing ratio is constant through all relevant layers of the atmosphere. This makes O₂ interesting for another important application. The knowledge about the line of sight geometry (see Section 2.2.1) is an important factor for occultation measurements. Since the O₂ concentration is only related to pressure and temperature, it can be calculated with relatively high accuracy. The concentrations can be used to adjust the geometry information by repeatedly performing O₂-retrievals. It is discussed in Section 6.1. This section focusses on the retrieval aspects of O₂.

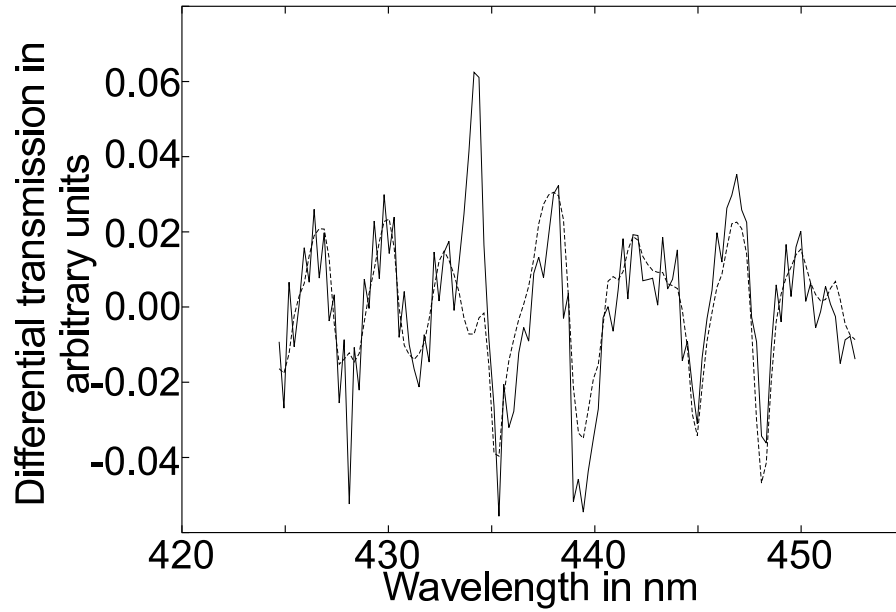


Figure 5.8: Spectral fit in the typical NO_2 fitting window at 13 km tangent height. Solid line: Transmission spectra obtained from the same measurements as in Figure 5.4. Dotted line: Forward model fit.

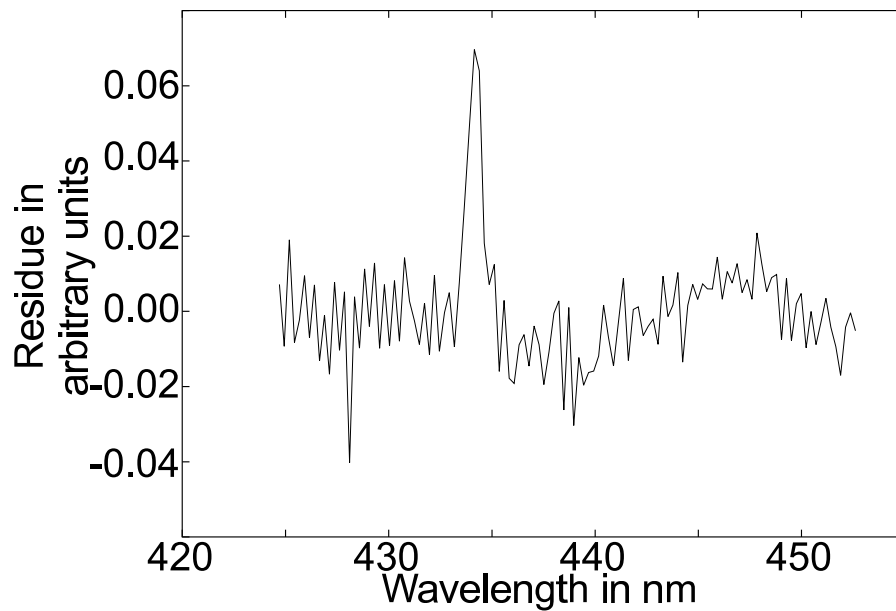


Figure 5.9: Residual of the spectral fit in Figure 5.8.

5.4.2 Retrieval Results

In the SCIAMACHY wavelength range, O_2 has only a few narrow absorption bands. The absorption bands are relatively weak compared to ozone and NO_2 . The cross sections are by several orders of magnitude lower than those of many other trace gases in the UV-vis range. However due to the large atmospheric abundance of O_2 , it is possible to extract significant spectral signals from the occultation measurements. Cross sections can be found in Appendix B. In this work, the A and B bands of O_2 have been used for vertical profile retrievals. The spectral positions are around 760 and 690 nm, respectively. They consist of many spectral lines, which have to be modeled with the line-by-line method introduced in Section 3.2.1.

In Figure 5.10, a typical spectral fit in the O_2 -B band is shown. The tangent height is about 8 km. The fit is part of a vertical profile retrieval, which was performed during the last iteration of a successful tangent height retrieval. The underlying data has been taken from a measurement of orbit 2056. It turns out that the O_2 -B band will be more appropriate for the tangent height retrieval if such extremely low tangent heights are considered. The O_2 -A band tends to be saturated at low heights, which makes spectral fits almost impossible. So far, the best results were obtained with a spectral fitting window ranging from 680 to 695 nm. A polynomial of the order of 3 was subtracted. Due to the small fitting window it is difficult to find an optimal compromise between these retrieval parameters.

The residual of the spectral fit is shown in Figure 5.11. As in the examples before, the residual is given in arbitrary units. The values, which are in the order of less than 2%, can be considered as a modeling error. It is a quite encouraging result that the spectral residual at low tangent heights is still very small. It seems that tropospheric conditions become the limiting factor for the O_2 profile retrieval. Cloud coverage and increasing water content are the most probable reasons for bad spectral fits. Furthermore, spectral inhomogeneities such as the Fraunhofer lines of the Sun can reduce the quality of the fit, especially at low tangent heights.

It is pointless to show the retrieved profiles as they are strongly regularised. The Tikhonov parameters were set to $T_1 = 10^4$ and $T_2 = 10^2$ (see Section 4.3.2). The regularisation is needed for a better performance of the tangent height retrieval. Additionally, it is not very interesting to show the well known exponential behaviour of O_2 vertical profiles.

Concerning the tangent height retrieval, it is an important task for the next future to optimise the retrieval of O_2 . Of course, a tangent height correction is particularly interesting at low heights as the precalculation of tangent heights is strongly limited by the knowledge of refractive effects.

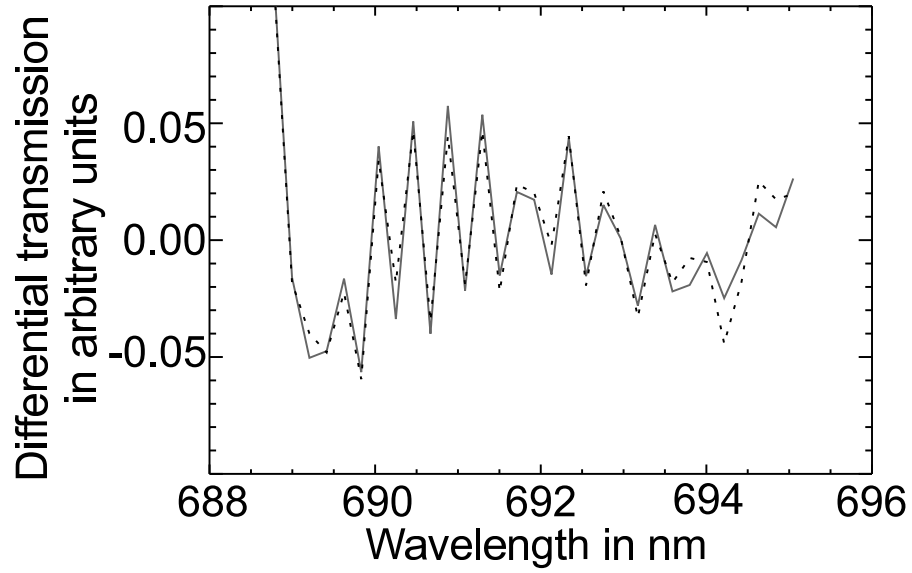


Figure 5.10: O₂ spectral fit at 8 km tangent height.

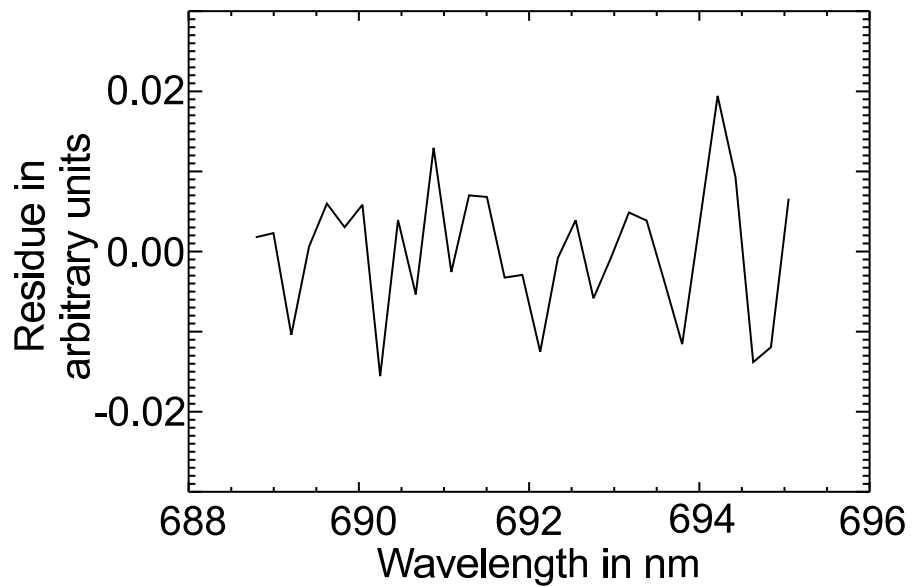


Figure 5.11: Residual to the spectral fit in Figure 5.10 in arbitrary units.

5.5 Carbon Dioxide

5.5.1 Background

Atmospheric levels of carbon dioxide (CO_2) have increased from 280 ppm in 1800 to 356 ppm in 1993. It is one of the most abundant trace gases. As a result of fossil fuel combustion, the current rate of increase is approximately 1.5 ppm per year. CO_2 is supposed to be one of the keys to the global warming. Only 15 to 20% of the total CO_2 amount resides in the atmosphere. The remainder is dissolved in the oceans. Due to the complex cycling of CO_2 in the terrestrial and ocean biosphere, it is not possible to define a meaningful lifetime. However, considering the atmosphere as an enclosed system, CO_2 is chemically inert and therefore a well-mixed gas. Significant deviations from this rule occur at higher altitudes, where CO_2 molecules are photolysed by increasing UV radiation.

For satellite measurements, CO_2 is interesting in the context of the Kyoto protocol from 1997. Most states ratified this agreement to reduce CO_2 emissions significantly in the near future. A commitment period, which is planned to start in 2008, could be supported by spaceborne measurements. A quantitative estimation of gas emissions regulated by the protocol need to be confirmed by independent measurements. So far, it is not clear if current spaceborne instruments will match these requirements. A detailed study by the ESA addresses these tasks. It can be found in [Breon, 2003]. In the context of this thesis, CO_2 was only used to confirm the results of the tangent height retrieval with O_2 (see Section 6.1). Furthermore, the CO_2 retrieval affirms the success of SCIAMACHY measurements in the IR wavelength range.

5.5.2 Retrieval Results

CO_2 is a typical infrared absorber. Like O_2 , it has to be modeled with the line-by-line method introduced in Section 3.2.1. The absorption cross sections can be found in Appendix B. Due to the frequently mentioned data processing problems, the CO_2 studies presented in this section focus only on spectral data from channel 6 of SCIAMACHY. The wavelength range between 1555 and 1585 nm turned out to be quite suitable for the spectral fit of CO_2 . Two strong CO_2 absorption peaks can be found here whereas other trace gases have only weak absorption features. The absorption cross sections of the peaks are much higher than those of O_2 . However due to much smaller concentrations, the absorption signal is even weaker than in the case of O_2 .

In Figure 5.12, a typical spectral fit of the CO_2 absorption signal is shown. The

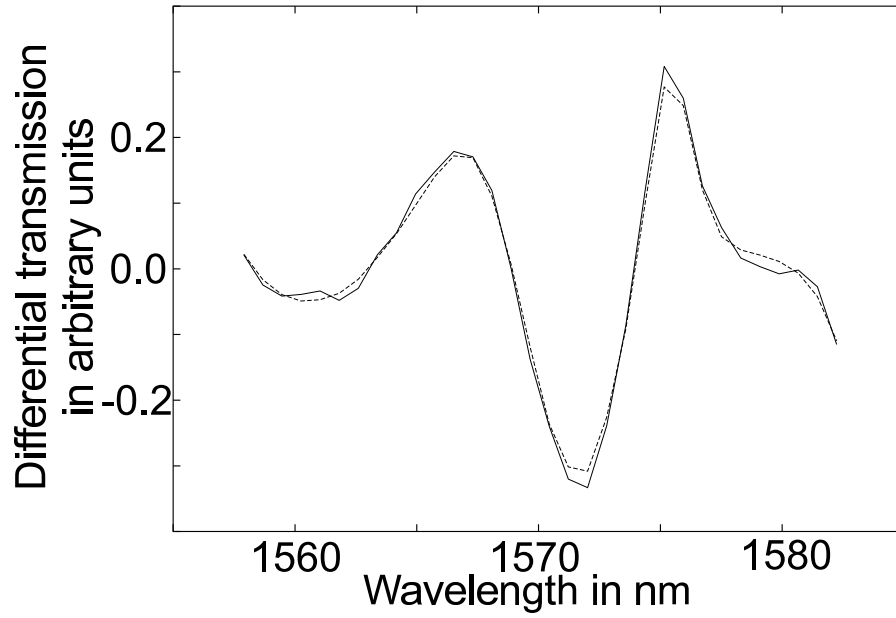


Figure 5.12: Spectral fit in the CO₂ fitting window at 6 km tangent height in arbitrary units.

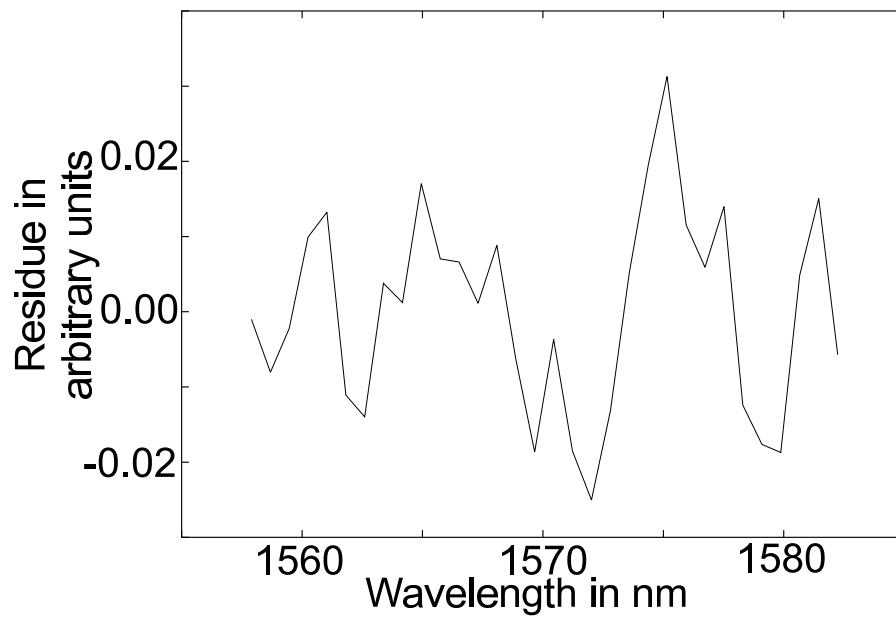


Figure 5.13: Residual of the spectral fit in Figure 5.12 in arbitrary units.

tangent height is approximately 6 km. The underlying data has been taken from measurements in orbit 2056. Together with the O₂ results from Section 5.4.2, the fit is part of the tangent height studies discussed in Section 6.1. The fit residual is shown in Figure 5.13. It can be seen that the model error is in the order of less than 3 %. The error is slightly larger than in the case of O₂, but still a very promising result. Similar to the O₂ retrieval, a strong regularisation was used for the profile retrieval. The Tikhonov parameters were set to $T_1 = 10^4$ and $T_2 = 10^2$ (see Section 4.3.2). Furthermore, a polynomial of the order of 3 was subtracted from the measured transmissions.

Further investigations on retrieval parameters such as fitting windows, subtracted polynomials, regularisations etc. are necessary to optimise the retrieval results. In the context of tangent height retrievals, the CO₂ retrievals confirmed the studies with O₂.

Chapter 6

Information on Geometry

All accuracies are limited at least by the knowledge about the line of sight geometry. In Section 2.2.1, the fundamental concept of occultation geometry is introduced. Line of sight bending and tangent height are the most important quantities that are needed for radiative transfer calculations. In principle, they can be calculated from ENVISAT's orbit parameters and some knowledge about atmospheric refraction. In practice, it turns out that the calculations are not reliable and have to be improved. To avoid errors due to spatial inhomogeneities of the solar disk (see Section 1.3), the exact pointing informations of SCIAMACHY with respect to the Sun are required. Line of sight and pointing geometry are treated in this chapter.

6.1 Tangent Heights

Originally, tangent heights were planned to be provided via the extensive geolocations of level-1 data products, which are to be received directly from ESA. However, data supply as well as data quality have been highly unreliable. In principle, it is possible to obtain tangent heights from pure orbital parameters of ENVISAT. These calculations can be implemented into evaluation algorithms using the CFI-Libraries* [Alvarez et al., 2000]. The CFI routines are capable of calculating many useful geometric quantities, especially solar zenith angles (SZA) at the top of atmosphere and tangent heights with and without atmospheric refraction (see also Section 2.2.1). They are also used by ESA in level-0 to level-1 data processing. Alternatively, refractive effects can be calculated by ray tracing routines as described by Johannes Kaiser [Kaiser, 2001], using information about the SZA at the top of atmosphere (see Section 3.2.2). Sometimes, it is useful to calculate tangent heights

*CFI stands for Customer Furnished Item

in a non-refractive atmosphere.

6.1.1 First Approach to a Tangent Height Retrieval

The idea of tangent height retrieval is based on the fact that there are gases whose volume mixing ratios are known quite accurately. This is true for O_2 , its dimer O_4 , and – with some restrictions – CO_2 . These are well-mixed constituents in the atmosphere. Thus, their concentrations are directly related to pressure and temperature via the ideal gas law. Molar concentrations of molecular oxygen C_{ox} can easily be obtained by

$$C_{ox} = \frac{p_{ox}}{R \cdot T}, \quad (6.1)$$

where T is the temperature, R the molar gas constant, and p_{ox} the partial pressure of O_2 . Molar concentrations of O_4 are obtained by

$$C_{O_4} = C_{ox}^2 \cdot F_{O_4}. \quad (6.2)$$

The conversion factor F_{O_4} depends on the physical units. Concentrations of CO_2 have to be taken from appropriate climatologies. Since CO_2 is chemically inert, it can be considered a well-mixed gas in the atmosphere. However, it is more and more photolysed within the stratosphere. The limiting factor is the knowledge of pressure and temperature profiles. For the following studies, globally averaged climatologies were used such as the US-standard climatology [NASA, 1976]. To some extent, they differ significantly from actual local profiles. However, the differences can be neglected in the context of this study.

Vertical profiles of these species are regarded as true information for the tangent height retrieval. Corresponding profiles retrieved from SCIAMACHY measurements are divided by the true profiles bearing a measure of relative deviation from the true concentrations. An estimation for a better tangent height h at height layer i for iteration step $k + 1$ is then calculated by

$$h_{i,k+1} = h_{i,k} - \frac{h_{i,k}^3}{f_{corr}} \ln \left(\text{abs} \left(\frac{C_{ox,i}^{ret}}{C_{ox,i}^{true}} \right) \right). \quad (6.3)$$

The superscripts *ret* and *true* indicate retrieval result and true information of trace gas concentration $C_{ox,i}$, respectively. f_{corr} is an empirical correction factor resulting from different parametrisation attempts. For O_2 it is of the order of 6,000. Smaller values force a faster but more instable retrieval, higher values lead to slower but stable calculations. The latter is recommended if the initial values for the tangent heights provided by ESA differ strongly from the true values. For CO_2 , Equation 6.3 has to be modified slightly:

$$h_{i,k+1} = h_{i,k} - \frac{h_{i,k}^2}{f_{corr}} \ln \left(\text{abs} \left(\frac{C_{co_2,i}^{ret}}{C_{co_2,i}^{true}} \right) \right) \quad (6.4)$$

with a correction factor f_{corr} of the order of 100. The case of O_4 has not been tested so far. The mathematical formulation has to be seen as an empirical result. Equation 6.3 and Equation 6.4 take advantage of the fact that each tangent height can be considered independently to a first approximation. It is a general feature of occultation geometry that absorption structures are mainly produced in an area around the tangent point. Therefore, it is reasonable that Equations 6.3 and 6.4 have no interdependence between the different tangent heights. For exponentially decreasing profiles such as those of the well-mixed species, the independence of the heights is clear because the extinction shows also the exponential behaviour.

For future applications of course, a more sophisticated retrieval algorithm has to be implemented as accurate calculations need many iterations at high computational costs. Nevertheless, the algorithm observed a general 2 km shift in the data provided by ESA, as will be described in Section 6.1.2.

6.1.2 Results

Tangent height retrievals for SCIAMACHY occultation measurements are performed for two reasons. First, they are needed for monitoring purposes, i.e. the Institute of Environmental Physics at the University of Bremen is involved in verifications of level-0 and level-1 data products. Secondly, tangent height retrievals will improve geolocations that are calculated properly from orbital parameters. Figure 6.1 shows a comparison of tangent heights obtained from orbital parameters and O_2/CO_2 retrievals in solid grey, solid black, and dotted lines, respectively. It can be seen that the retrieval shifted the tangent heights by 2 to 3 km throughout the measurement sequence. The CO_2 retrieval converges towards the initial tangent height information for higher altitudes. This can be explained by weak absorptions in this region leading to a lower information content. Details of trace gas retrieval results can be found in Chapter 5. So far, similar shifts of the same order of magnitude were observed in all investigated data sets.

Deficient precalculations of SCIAMACHY's pointing geometry account for the tangent height shift. This can be learned from Figure 6.2. It shows a cutout from the movement of SCIAMACHY's elevation mirror during an occultation measurement sequence (see Section 2.1.2). The time interval was chosen such that the plot focusses on the sun-follower adjustment in vertical direction. The zigzag line represents the motion of SCIAMACHY's FOV whereas the straight line shows the precalculated position of the Sun in terms of elevation angle. As can be seen, there is a difference of around 0.05° between the precalculated and the true position of the Sun as seen by SCIAMACHY's sun-follower. The difference can be observed in all occultation measurements that have been investigated so far. Figure 6.3 shows the observed difference of Figure 6.2 for successive orbits in the time between Au-

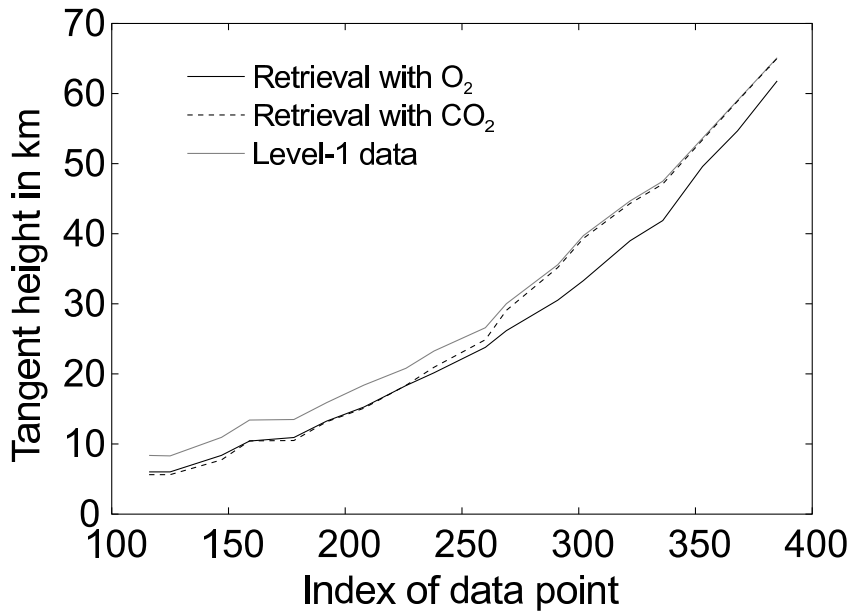


Figure 6.1: Tangent heights vs. data index number of the occultation scan in orbit 2056 on July 22, 2002. Solid grey line: level-1 tangent heights. Solid black line: O₂ retrieval. Dotted line: CO₂ retrieval.

gust and November 2002. Details of the time dependence are not understood. But it can be seen that there is an average misalignment of approximately 0.04° . In terms of SCIAMACHY's instrument geometry, it corresponds to the height of the FOV. It can be transformed into an average height difference at the tangent point by simple geometric considerations (Equation 2.6). As a result, the observed tangent height shift can be identified with the differences in the elevation angle. Other evidence for a systematic error in the engineering data of ENVISAT is given by Stiller [2003]. The data evaluation of MIPAS, which faces the opposite direction than that of SCIAMACHY, gives the same shift in tangent height with opposite sign.

6.2 Pointing on the Solar Disk

As already discussed in Chapter 1 and Chapter 3, the solar disk is not a homogeneous source of light. The impact of varying Fraunhofer structures is particularly significant. A reduction of Fraunhofer structures will be obtained if reference measurement and atmospheric measurement have the corresponding FOV position on the solar disk. A matching routine has been implemented for this task and will be discussed in this section. Since the solar disk is flattened due to refractive effects,

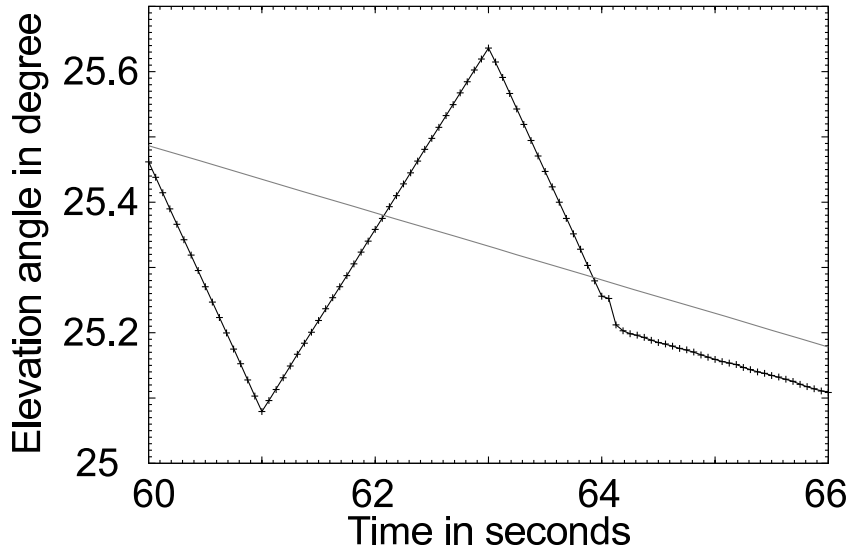


Figure 6.2: Elavation angle of SCIAMACHY's line of sight (black line) and precalculated elevation of the rising Sun (grey line) vs. time [Noel, 2003].

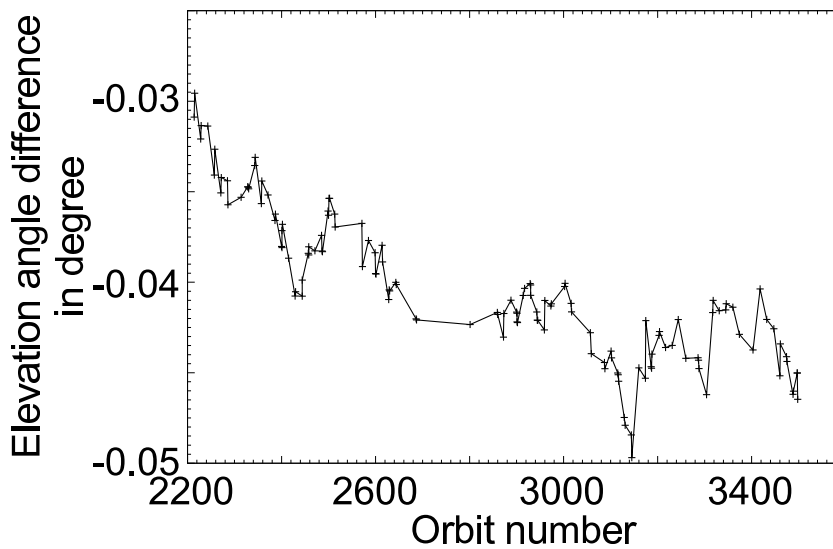


Figure 6.3: SCIAMACHY elevation misalignment vs. orbit number for the time from Aug 1 to Nov 1, 2002 [Noel, 2003].

it is not trivial to find appropriate reference measurements. These issues will also be discussed.

6.2.1 Refraction

It is understood that refraction has a strong impact on the solar disk pointing geometry. In this context, it is important to know the total bending angle α after passing the atmosphere as a function of tangent height (see Figure 2.3 and 6.4). It can be calculated via the ray trace routines [Kaiser, 2001], which are based on the successive application of Snell's law (Equation 3.21). Other numerical methods are also appropriate, e.g. based on Fermat's law of light propagation, as discussed in [DeMajistre et al., 1995]. For groundbased observations, a suitable solution was developed by Thomas and Joseph [1996].

In the context of occultation measurements, it was shown by Michael Lutomsky [Lutomsky, 2002] that a simple approximation for bending angle α is sufficient instead of sophisticated ray path models. It is even possible to assume refraction to take place only at the tangent point (see Figure 6.4). Since refraction takes place whenever there is a gradient in the density of a medium, it is mainly affected by the exponential behaviour of the vertical pressure gradient. Temperature variations also influence refraction but can be neglected to a first order approximation. According to discussions in [Garriott, 1979] and [Rozenberg, 1966], bending angle α shows the same exponential behaviour as a function of tangent height h_g . It can be written as

$$\alpha(h_g) = \sqrt{\frac{2\pi R_E}{h_0}} N_0 e^{-\frac{h_g}{h_0}}, \quad (6.5)$$

with $h_0 = 8$ km as scale height, N_0 as the refractivity at 0 km tangent height, and R_E as the Earth's radius. Refractivity N is closely related to the refraction index n_s by $N = n_s - 1$ and can easily be obtained by Equation 3.16. In [Rozenberg, 1966], an equivalent formulation can be found for $\alpha/2$, which uses empirical coefficients:

$$\alpha(h_g)/2 = 0.013 \cdot e^{-0.16 \cdot h_g}. \quad (6.6)$$

In Figure 6.5, bending angle α is plotted as a function of tangent height h_g within SCIAMACHY's wavelength range. In [Lutomsky, 2002], it is shown that differences between numerically calculated bending angles and exponential approximations can be neglected.

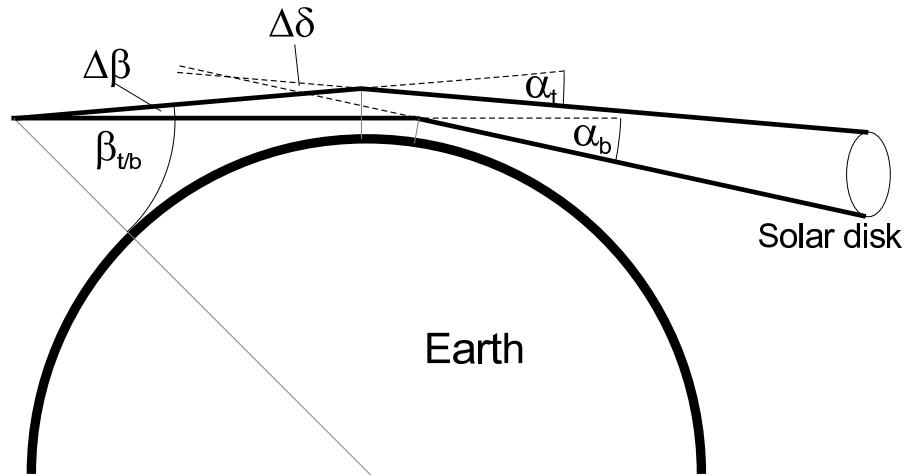


Figure 6.4: Illustration of some geometric quantities used in this section. Note that refraction is assumed to take place at the tangent point. Indices t and b denote top and bottom of the apparent solar disk, respectively.

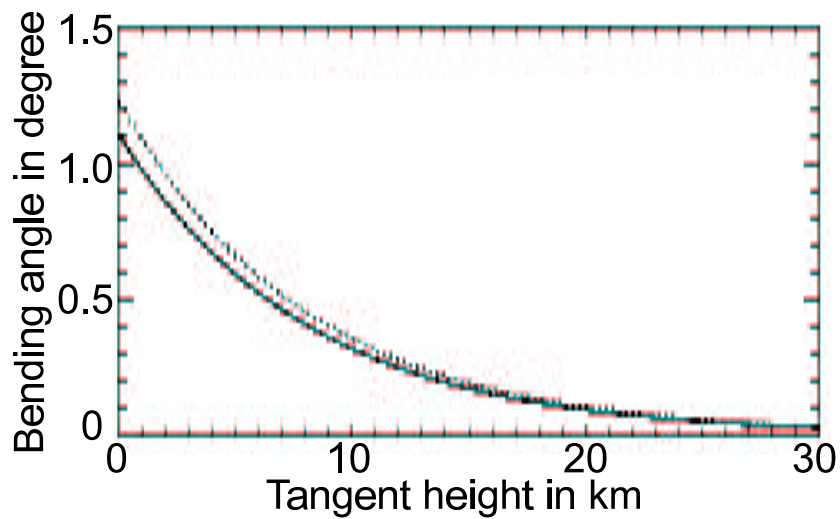


Figure 6.5: Bending angle α vs. tangent height h_g in occultation geometry for two wavelengths. Solid line: 2380 nm. Dotted line: 240 nm.

6.2.2 Sun Flattening

As a result of the tangent height dependence of bending angle α (Section 6.2.1), it is understood that the solar disk appears to be flattened. The atmosphere acts like a concave lense. Since the solar disk covers roughly 30 km of tangent height range, it is obvious from Equation 6.5 that the top and the bottom limb of the Sun have significantly different bendings through the atmosphere. Garriott [1979] gave a very simple geometric approach to calculate the sun flattening quantitatively. This approach assumes refraction to take place only at the tangent point instead of a continuous process through all height layers. Garriott introduced a so-called exit angle δ defined by

$$\delta = \alpha - \beta, \quad (6.7)$$

where β is the elevation angle of SCIAMACHY (see Section 2.2.1). The compression of the vertical axis of the solar disk r_{sun} is then obtained by

$$r_{sun} = \frac{\Delta\beta}{\Delta\delta}. \quad (6.8)$$

Differences in δ and β are with respect to the top and bottom limb of the solar disk. Some of these quantities are illustrated in Figure 6.4. $\Delta\delta$ can be identified by the apparent diameter of the Sun, which is 0.53475° .

Furthermore, the light intensity measured by the detector is diluted by the purely geometric effect of incident parallel bundles of rays diverging after passing the atmosphere. According to Dalaudier et al. [2001], the geometric dilution factor D is given by

$$D = \frac{1}{1 + d_{sat} \frac{d\alpha}{dh_g}}. \quad (6.9)$$

D depends on the distance d_{sat} between satellite and tangent point and the derivative of bending angle α with respect to tangent height h_g . Combining Equations 6.6 and 6.9, dilution factor D can be written as

$$D = \frac{1}{1 + 0.00416 \cdot d_{sat} e^{-0.16 \cdot h_g}}. \quad (6.10)$$

d_{sat} can easily be calculated by

$$d_{sat} = \sqrt{(R_E + h_{orb})^2 - (R_E + h_g)^2}, \quad (6.11)$$

where R_E denotes the Earth's radius and h_{orb} the orbit altitude of the observer.

In the left plot of Figure 6.6, the relative compression due to flattening is plotted vs. tangent height as a solid line. Tangent heights are given for top and bottom limb of the solar disk. The difference between the solid lines on the x-axis correspond

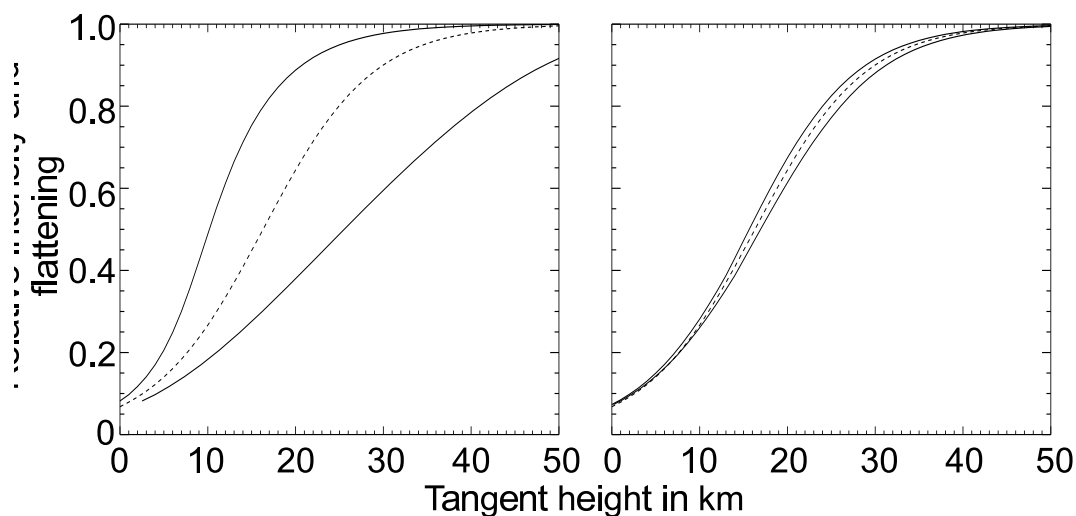


Figure 6.6: Relative flattening (solid lines) and reduction of intensity (dotted line) vs. tangent height. On the left: effects on the solar disk. On the right: effects on the vertical dimension of SCIAMACHY's FOV.

to the apparent vertical size of the solar disk in km. The dotted line represents the reduction of intensity due to the dispersal of light rays by atmospheric refraction. It can be seen that the sun flattening and the dilution show the same behaviour. Since the apparent solar disk is large compared to the height scales of Equations 6.5 and 6.6, top and bottom limb are affected differently. The compression factor r_{sun} is also an exponential function of tangent height.

For occultation retrievals it is also interesting to know how single measurements are affected by flattening and intensity reduction. For SCIAMACHY's FOV, $\Delta\delta$ in Equation 6.8 can be regarded as 'true' FOV height as in the case of the solar disk. The FOV height is 0.045° . $\Delta\beta$ is then the compressed height of the FOV. It is plotted on the right side of Figure 6.6 in solid lines. Again, the dotted line represents the dilution factor D . Figure 6.7 illustrates how occultation measurements are affected by sun flattening. Two typical occultation scans are depicted: a measurement scan through the atmosphere with sun flattening due to refraction and a reference scan above the atmosphere without refraction. As pointed out in the previous chapters, atmospheric measurements need to be assigned to an appropriate reference spectrum in order to obtain atmospheric transmissions. As can be seen, the FOV will cover a larger area of the solar disk if tangent heights are low enough. The enlargement can be calculated with Equation 6.8.

Results for the seeming FOV enlargement are given reciprocally in the right plot of Figure 6.6. In contrast to the flattening of the solar disk, differences with respect

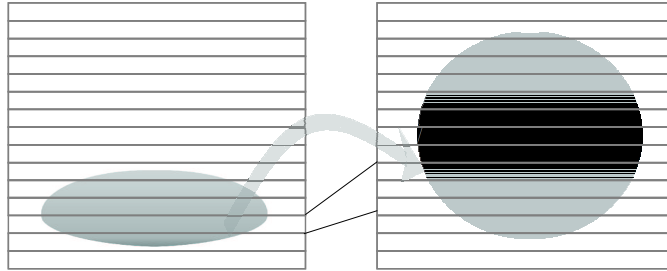


Figure 6.7: Illustration of the sun pointing problem. On the left, an atmospheric occultation scan is depicted with refractive effects. On the right: Reference scan above the atmosphere.

to top and bottom of SCIAMACHY's FOV are small and almost equal to the dilution factor D . This means in turn that the reduction of intensity is almost completely compensated by the seeming FOV enlargement. Note that this is true only for occultation targets larger than the FOV. As discussed in [Dalaudier et al., 2001], dilution factor D has to be taken into account for stellar occultation measurements.

6.2.3 Matching Algorithm

Requirements

Since the Sun is not a homogeneous source of light, an algorithm has to be implemented with regard to the discussion in Section 6.2.2. In order to obtain appropriate transmission spectra, every measurement has to be assigned to an appropriate reference measurement from above the atmosphere. However, it is almost impossible to address all effects properly that come along with atmospheric measurements. The following issues have to be taken into account by an ideal matching algorithm:

- Consecutive measurement scans cannot be aligned exactly to the solar disk. Even measurement scans above the atmosphere and without refraction have different pointing characteristics. The maximum pointing error is estimated to 0.012° or roughly one fourth of the FOV height [van Rie, 1995].
- The fraction of the solar disk covered by the FOV is significantly enlarged for tangent heights below 30 km. Although global intensities are leveled off due to a corresponding geometrical dilution, it is more difficult to find an appropriate reference spectrum with respect to changing Fraunhofer lines.
- Real occultation measurements have spectral shifts as the spectral resolution of SCIAMACHY is too low, especially with respect to Fraunhofer lines.

- Measurements close to the solar limb have a different illumination of the FOV. In general, detector signals are a function of spatial illumination. It is questionable if this effect can be covered by a sophisticated assignment to the reference scan.
- The effect of flattening is a function of tangent height, even within the small height range of the FOV. It remains an open question whether it is negligible or not.
- Spectral inhomogeneities of the solar disk are also time dependent. Most effects should be minimised by the fact that there are reference measurements after each occultation event. Nevertheless, changes on a time scale of minutes are still possible as e.g. described by Neckel and Labs [1990].

An algorithm has been developed that addresses at least the first two items. An optimal reference measurement is estimated from a sun scan above the atmosphere. Since interpolations between adjacent references are also taken into account, it is possible to find an optimal reference with respect to the exact pointing on the solar disk. Additionally, the algorithm accounts for different seeming FOV extensions arising from the sun flattening. So far, wavelength shifts are ignored in this context. As will be shown later, it might be useful to integrate the matching algorithm into the shift-and-squeeze algorithm. It has to be used anyway to overcome deficiencies in the wavelength calibration. The impact of different slit illuminations and sun flattening within the FOV have not been investigated up to now. Variations of the solar spectrum on a time scale of less than minutes are expected to remain a minor but unsolved problem.

The Algorithm

A typical occultation measurement scan consists of 16 or 32 single measurements depending on integration time and data transmission rate between SCIAMACHY and the ground segments (see Figure 6.7). First of all, atmospheric measurements are sorted out which do not match the Sun or have too weak intensities at the solar limb. The remaining data covers a more or less extended region around the centre of the solar disk. In a second step, a range of measurements above the atmosphere is identified as a *reference scan*. Usually, all scans above roughly 100 km are suitable as a reference. Since all scans have slightly different pointing characteristics, it would be meaningful to use all the information that is available from above the atmosphere. However in reality, the reference scan is reduced to one up or down scan due to computational costs. The following procedure is then repeated for every atmospheric measurement:

1. Spectral windows with strong Fraunhofer lines are chosen.
2. The reference scan is divided into small steps with respect to their elevation angle. Elevation steps between adjacent reference measurements are interpolated.
3. The following procedure is repeated for every elevation step within the reference scan:
 - (a) The spectra within the Fraunhofer windows Υ are divided by corresponding spectra of the reference scan Υ_0 .
 - (b) A polynomial p_n of the order of 3 is subtracted to reduce the transmission to its differential structure. Fraunhofer lines can now be clearly identified.
 - (c) The absolute values of the differential transmission intensities are integrated over wavelength λ :

$$S = \int_{\Lambda} d\lambda \left| \frac{\Upsilon}{\Upsilon_0} - p_n \right| \quad (6.12)$$
 - (d) Steps a to c are repeated with different effective heights for the FOV in order to account for the sun flattening.
4. The elevation step with the smallest integration sum of absolute values over the Fraunhofer windows is now considered to be the optimal reference for this measurement.
5. The whole spectrum needed by the retrieval is divided by the optimal reference, which is often an interpolation between two measurements of the reference scan.

Results of the algorithm are discussed in Chapter 7 as remaining Fraunhofer structures are closely related to a detailed error analysis.

6.2.4 Other Methods

The Geometric Approach

The matching algorithm introduced above is purely based on spectral properties of the measurements. Of course, a more obvious approach would be the geometric calculation of the pointing. Geometric calculations are performed e.g. in the

case of POAM, as described in [Glaccum et al., 1996] and more detailed in [Lumpe et al., 1997]. However, this approach needs reliable information on some geometric quantities such as the elevation angle. The SCIAMACHY data supply has not been sufficient in this respect. Furthermore, geometric calculations have limited accuracy and do not account for spectral issues, which are significant to the quality of the spectral fittings. Following the discussion in Section 6.2 and Section 8.2.2, it seems to be a very promising task to combine geometric calculations with the matching algorithm.

Spectral Fitting of Fraunhofer Lines

A third way of addressing the Fraunhofer line problem was developed at the Institute of Environmental Physics in Heidelberg, as described by Bösch [2002]. The basic idea is to perform a spectral fit of changing Fraunhofer lines. In [Bösch, 2002], two high resolution spectra were taken to define the behaviour of Fraunhofer lines towards the solar limb. The first one is an average spectrum of the whole solar disk $I_0(\lambda)$. The second one is a measurement of the solar centre $I_C(\lambda)$. The true solar spectrum $I_{true}(\lambda)$ is then replaced by an optimal estimation of both spectra:

$$I_{true} = I_0 + a(I_0 - I_C) \quad (6.13)$$

The scaling factor a is mathematically considered in the same way as any other fitting parameter in the retrieval algorithm.

The spectral fitting is certainly the most elegant way of addressing the Fraunhofer problem. However, spatially and spectrally highly resolved reference spectra are needed in order to obtain significantly better results by this method. Furthermore, the reference spectra should be taken from space without any impact of atmospheric extinction. Otherwise, the problem turns into the opposite, i.e. atmospheric absorption features must be removed elaborately. Finally, the reference spectra need to be updated regularly due to the time dependent changes of the Fraunhofer lines. So far, such extraterrestrial high resolution spectra do not exist.

Chapter 7

Error Analysis

A detailed error analysis is essential to any kind of physical measurement, especially for further applications such as data assimilation. In the case of atmospheric parameter retrieval, random errors are described by covariance matrices. It is part of the optimal estimation theory introduced in Chapter 4. So far, there are many error sources that are not treated this way. This chapter gives an overview of different errors. A first approach towards a realistic error estimation is discussed.

7.1 Spectral Errors

7.1.1 Spectral Inhomogeneities

Inhomogeneities in the solar spectra are mainly caused by Fraunhofer lines in combination with the limb darkening effect as discussed in Section 1.3 and Section 1.4. Theoretically, transmissions derived from appropriate measurements are not expected to contain any structure except atmospheric extinction signals, but in practice, Fraunhofer lines cause the main contribution to residuals of spectral fits. This section focusses on Fraunhofer structures in the wavelength range between 420 nm and 460 nm, a typical fitting window for NO_2 . This window is particularly interesting due to a strongly decreasing sensitivity towards shorter wavelengths in this region. This can be seen from the signal-to-noise investigations in Section 3.4.1. Many interesting weak absorbers such as BrO and OClO have a maximum absorption cross section in the UV-vis wavelength region. The ability to retrieve concentrations of these species depends on the reduction of disturbing spectral structures such as the Fraunhofer lines in the UV-vis wavelength range. The residual of a spectral retrieval fit is a good indicator for unexpected

spectral signals. It reflects all spectral structures that have not been modeled in the retrieval process.

Figure 7.1 shows residuals of several O₃ and NO₂ retrieval fits. They are obtained from an up scan over the solar disk. The estimated pointing on the solar disk is indicated by small icons. Two cases are distinguished for each pointing and corresponding tangent height. On the right side, no efforts were made to remove Fraunhofer lines. One extraterrestrial measurement pointing to the solar centre was taken as a reference for all atmospheric measurements. On the left, the matching algorithm described in Section 6.2.3 was applied in advance of the trace gas retrieval. Here, every measurement was assigned to an 'optimal' reference from above the atmosphere. At least one strong Fraunhofer line can be identified around 434nm in this fitting window. It is the H_γ-line. It can clearly be seen that it has been removed successfully by the matching algorithm on the left side. Looking at the residuals either at smaller tangent heights or at the solar centre, no differences can be seen between the residuals.

7.1.2 Wavelength Shifts

There are mainly two kinds of wavelength shifts. Some have real physical reasons such as Doppler shifts, pressure broadening etc. Others are artefacts caused by the instrument itself such as thermal drifts etc. In this section, only those wavelength shifts are discussed which are characteristic for occultation measurements and have not already been discussed in Chapter 3.

Doppler Shifts

Doppler shifts arise whenever there is a relative velocity of the satellite with respect to the source of light, i.e. the Sun itself in the case of solar occultation measurements. The orbit velocity v of SCIAMACHY is 7.5 km/s. The velocity vector has an angle of 30° with respect to the Sun as described in Section 2.1.1. It results in a reduction of the relative velocity by approximately $\cos 30^\circ$. Additionally, the line of sight angle η with respect to the velocity vector can be obtained geometrically by

$$\eta = 90^\circ - \arcsin\left(\frac{R_E + h_g}{R_E + h_{orb}}\right). \quad (7.1)$$

R_E is the Earth's radius, h_g and h_{orb} are tangent height and orbit altitude, respectively. The relative velocity v_{sun} is now given by

$$v_{sun} = \cos 30^\circ \cdot \cos \eta \cdot v. \quad (7.2)$$

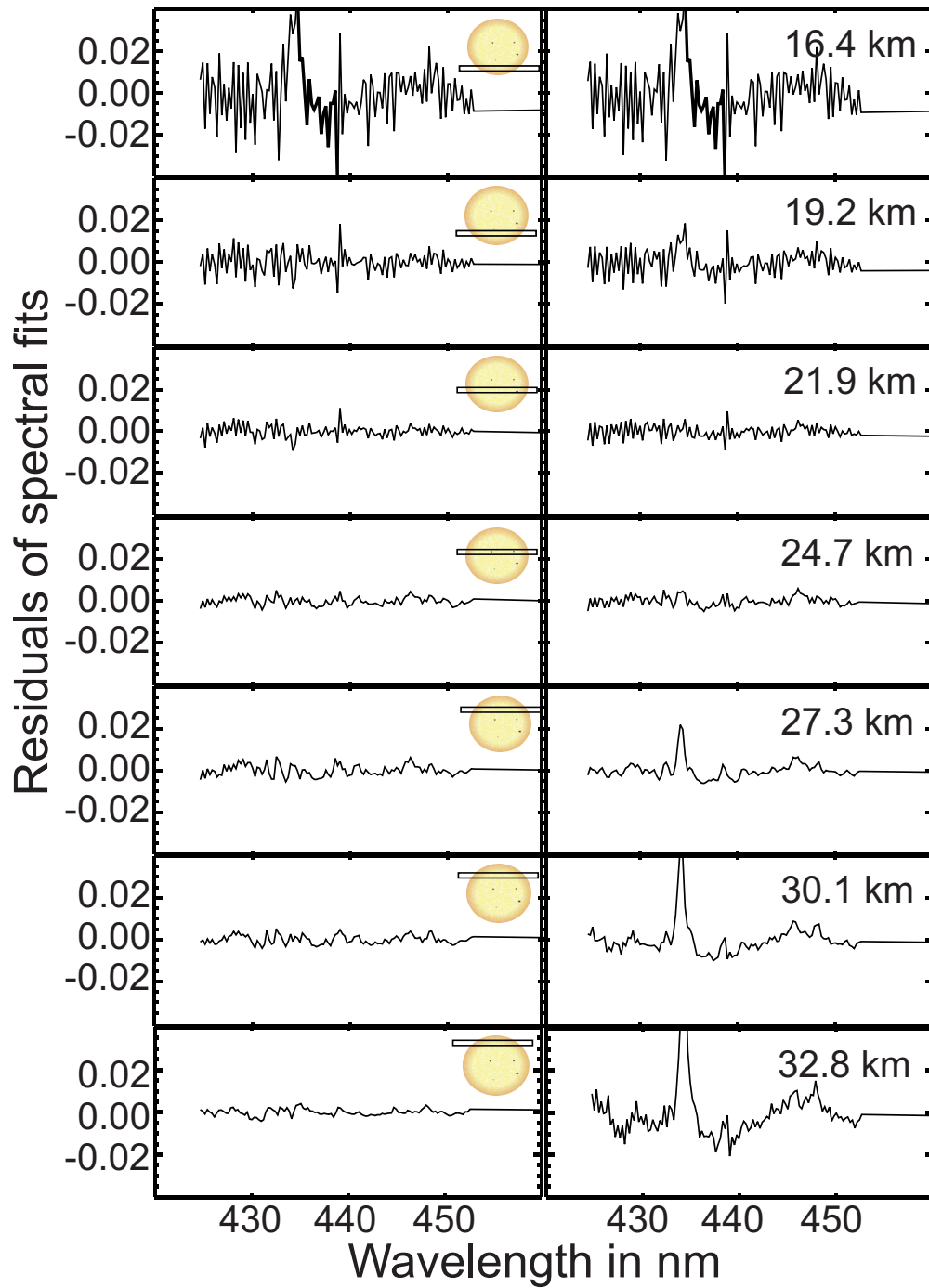


Figure 7.1: Spectral residuals of retrieval fits for consecutive measurements of an occultation up scan. Left: With solar matching algorithm. Right: Without solar matching routine.

In the cases of 0 km and 100 km tangent height, v_{sun} amounts to 5.59 km/s and 5.68 km/s, respectively. The Doppler shift $\Delta\lambda$ can be expressed by

$$\Delta\lambda = \lambda_0 \cdot \frac{v_{sun}}{c}, \quad (7.3)$$

where λ_0 denotes the original wavelength and c the speed of light. For the extreme cases above and wavelength $\lambda_0 = 400$ nm, $\Delta\lambda$ becomes $7.46 \cdot 10^{-3}$ nm and $7.58 \cdot 10^{-3}$ nm, respectively. These values are small compared to other wavelength shifts and can be removed in the course of the shift and squeeze algorithm. Also the difference between the extreme cases, which might be of interest for the calculation of transmissions, is very small and can be neglected. Furthermore, the Doppler shift is calculated for each measurement during the level-1 data processing. So it can alternatively be subtracted in advance.

Another important point is the variation of the Doppler shift due to the rotation of the Sun. The angular velocity of the Sun ω_{\odot} depends on the heliographic latitude. Its maximum can be observed at the equator with a rotational period T_{\odot} of 25 days. Also the surface velocity v_s has its maximum at the equator. v_s can be calculated from the Sun's radius $R_{\odot} = 6.69 \cdot 10^8$ m and angular velocity $\omega_{\odot} = 2\pi/T_{\odot}$ by $v_s = \omega_{\odot} \cdot R_{\odot}$. At the Sun's equator, v_s is 1.95 km/s.

Since SCIAMACHY's FOV covers a small stripe over the whole solar disk, it is possible to encounter two regions of the Sun with extreme values for v_s and opposite sign. Therefore, the relative velocities of the satellite v_{sun} can vary roughly between 3.5 km/s and 7.5 km/s within the same measurement. So far, it has not been investigated how the solar spectra are affected by it. However, since the Doppler shift appears to be small compared to other effects, it is very likely to be negligible. Furthermore, if the solar matching algorithm is applied, transmissions should be calculated correctly.

“Atmospheric” Shifts

For lower tangent heights, measured spectra appear to be shifted. The effect is not a real physical shift of the spectra such as the Doppler shift. It is more or less an artefact of real spectrometers. In [Sioris et al., 2003], it is described how atmospheric measurements may appear shifted in the context of limb measurements. In principle, it is also true for occultation measurements. Figure 7.2 illustrates schematically the influence of molecular background (Rayleigh) scattering. In the left plot, a spectral peak is depicted, which is narrow compared to the spectral pixels A, B, and C. The signals of the detector pixels are obtained approximately by integration of the curve within the pixel boxes. Obviously, detector pixel B would measure the strongest intensity. In the right plot, some molecular scattering has

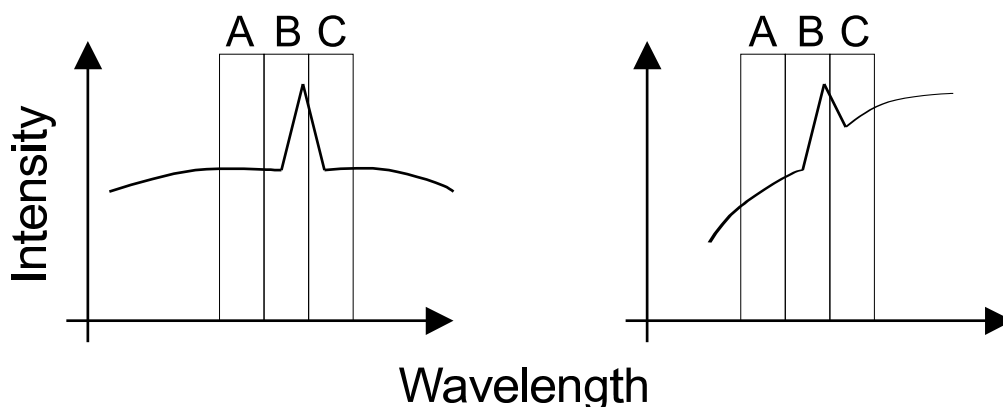


Figure 7.2: Schematic illustration of the spectral shift due to undersampling. Left: Narrow spectral peak without Rayleigh scattering. Right: The same peak with Rayleigh scattering. A, B, and C exemplify spectral pixels of a real spectrometer.

been added, which is wavelength dependent to the power of -4. Surprisingly, detector pixel C would now give the strongest signal.

In [von Savigny et al., 2002], a more technical explanation is given for wavelength shifts that are observed in the SCIAMACHY limb measurements. A spatially inhomogeneous illumination of the detector slit can also lead to the observed wavelength shifts. The detector slit is optically mapped onto the detector pixels. For SCIAMACHY, the height dimension of the FOV corresponds to the wavelength dimension of the detector pixels. Therefore, the detector response will appear to be shifted if the illumination changes significantly within the FOV height. A simple model has been developed by Visser [2002] to calculate possible wavelength shifts. According to Christian von Savigny [von Savigny et al., 2002], the agreement between model calculations and actual SCIAMACHY limb measurements is quite good. The model calculations assume an exponentially decreasing signal with increasing tangent height, which is generally true for limb measurements. In the case of occultation geometry, the tangent height dependence of the measurement signal is just the other way round, i.e. the signal is increasing with height. Additionally, the spatial illumination of the FOV is significantly affected by the appearance of the solar disk and the pointing on it.

The spectral residuals discussed in Section 7.1.1 show a lot of narrow peaks, especially for small tangent heights. When the matching algorithm is applied to measurement data, possible wavelength shifts have not been addressed. This is done later during the main retrieval routines. Therefore, the discussed effects can especially disturb the matching algorithm. Both the undersampling as well as the illumination dependent detector responses can explain the increase of structures

for small tangent heights.

Shifts in Occultation Measurements

Figure 7.3 shows how the occultation transmission spectra are affected by spec-

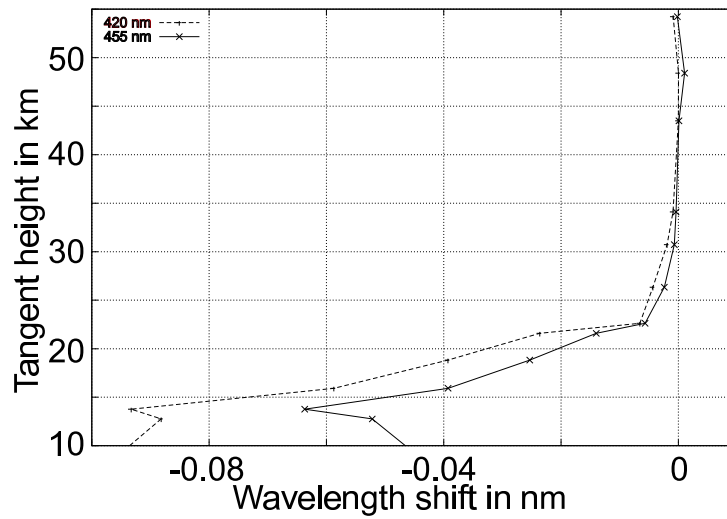


Figure 7.3: Relative spectral shift of the solar reference spectrum in nm vs. tangent height in km as estimated by the shift and squeeze algorithm. The NO_2 fitting window is represented here by its start and ending wavelength [Schlesier, 2002].

tral shifts in the NO_2 fitting window. The relative shift of the solar reference spectrum compared to atmospheric spectra is given in nm vs. tangent height in km. The spectral shift is estimated during the retrieval process by the shift and squeeze algorithm introduced in Section 4.3.3. The study has been provided by Anke Schlesier [Schlesier, 2002]. It can be seen that there is a clear increase of the spectral shift towards lower tangent heights. So far, the spectral undersampling due to differently sloped continua cannot be the reason in a simple obvious way as there are no clear changes in the slope of the spectra in this wavelength range. It is a complex task to distinguish clearly between effects that are due to the undersampling and those due to the inhomogeneous illumination of the FOV. Possible answers to this question are especially interesting for the design of future occultation instruments. It seems to be a straightforward task to improve the model of Visser [2002] with respect to the solar occultation characteristics. In the context of trace gas retrievals, it is perhaps sufficient to combine the shift and squeeze algorithm with the matching routine in order to get rid of the wavelength shifts.

7.2 Geolocation

In the following sections, geometric issues of SCIAMACHY's line of sight (LOS) are discussed. In general, spaceborne measurements have very limited spatial resolution compared to in-situ or ground based measurements due to the orbit altitude. Retrieval results must be seen as an average over a more or less extended region of the atmosphere. For data interpretation and ongoing applications, it is important to know the properties and the errors of the LOS as well as the tangent point location.

7.2.1 Tangent Point Location

Most of the information contained in a single measurement originates from the region around the tangent point. The information content of a retrieved profile is mainly composed of measurements at several tangent heights with different tangent point locations. Figure 2.5 gives already an overview of tangent point locations for a complete occultation sequence. The zooming in of Figure 2.5 is shown here again in Figure 7.4. A kilometer scale has been added to give a rough estimation of the geographic extensions of an occultation measurement. It can be seen that the measurements are located in an area comparable to that of the Federal Republic of Germany. Usually, only a minority of the measurements are used as retrieval input. Locations of typical measurements needed for standard retrievals of O_3 and NO_2 are indicated by the shaded area. Tangent points of particular importance are located around the middle of an up or down scan. Here, the signal-to-noise ratio is higher as a matter of principle. Furthermore, tangent heights around and below 17km are especially interesting from a scientific point of view. They can be recognised by the small movement disturbing the usual up and down scanning. The shading in Figure 7.4 is a little bit darker in this region. As mentioned in Section 2.1.2, it is the point of adjusting the FOV to the solar disk performed at 17.2km tangent height. It can be seen that a much smaller area is covered by the 'important' tangent points. It is comparable to the size of a smaller state within Germany or roughly 150 km by 100 km.

7.2.2 Line of Sight Geometry

Field of View Size

SCIAMACHY's field of view (FOV) and the scanning sequence were already introduced in Chapter 2. A relation between the FOV dimensions in degree and the

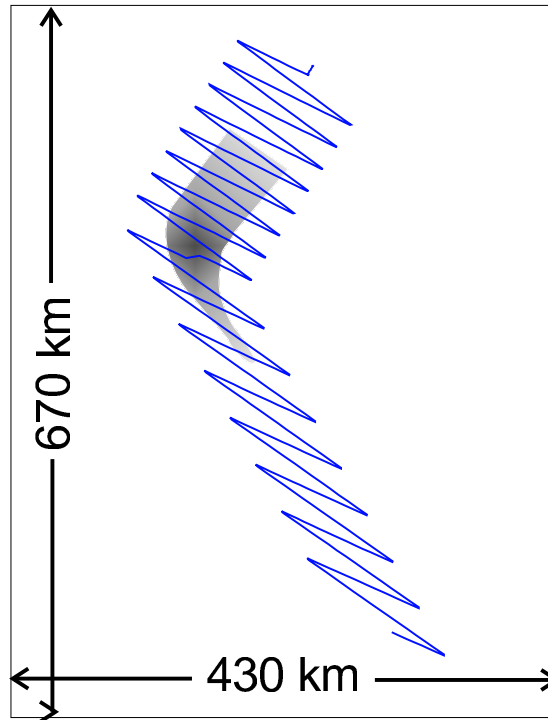


Figure 7.4: Geolocation of tangent points of a complete occultation sequence (state 47). The shaded area highlights those tangent points that are sufficient for a standard O_3 and NO_2 retrieval.

extension of a corresponding airspace around the tangent point in km can be easily obtained from Figure 2.3:

$$FOV_{km} \approx FOV_{deg} \cdot \frac{\pi}{180^\circ} \cdot \sqrt{(h_{orb} + R_E)^2 - (h_g + R_E)^2}. \quad (7.4)$$

R_E is the Earth's radius, h_{orb} and h_g are orbit altitude and tangent height, respectively. The FOV height (0.045°) corresponds to 2.43–2.59 km at the tangent point depending on the tangent height. The lower value is for a maximum height of 100 km and the higher value for a minimum height of 0 km. For the FOV width (0.7°), values of 37.8 to 40.2 km are obtained, respectively. Additionally, the measured air parcels are smeared due to the scanning movement and the elevation rate of the Sun.

However, the vertical FOV is only partly illuminated by the solar disk, which is 0.53° . Therefore, the effective width at the tangent point is reduced to 28.6 and 30.4 km, respectively. For pointing positions close to the solar limb, the effective width is further reduced.

Pointing Mode

Most SCIAMACHY solar occultation measurements are performed in the scanning mode. However, some are performed in the pointing mode, where the FOV is locked to the brightest point on the solar disk and follows it to the top of atmosphere. Also the lunar occultation measurements are performed this way. One measurement usually takes 62.5 ms. The elevation rate of the Sun as seen from the satellite depends slightly on the season and is approximately 0.05° per second. This means, that the FOV moves by 0.003° during one integration time. That is more than one order of magnitude smaller than the FOV height. In other words, SCIAMACHY's FOV has to be moved by less than one tenth of its height during one integration time to follow the Sun, which corresponds to approximately 0.2 km at the tangent point. In channels 6 and 7 the pixel exposure time (PET) is only 31.25 ms resulting in a smaller elevation movement during the PET.

Due to ENVISAT's orbit properties, there is also a small azimuth rate of the rising Sun. It is approximately 0.012° per second and is negligible in any event.

Scanning Mode

As shown above, elevation and azimuth rates of the rising Sun are small and can be neglected. However, the scanning movement of SCIAMACHY is with $0.33^\circ/\text{s}$ more than six times faster than the Sun's elevation rate. In terms of tangent height, the scanning leads to an effective FOV enlargement of roughly 1.3 km. It has to be distinguished between up scans and down scans. Since the scanning movement is added to the basic elevation rate, the enlargement amounts to 1.1 km for a down scan and 1.5 km for an up scan. For channels 6 and 7, the PET is only 31.25 ms. In this case, the FOV enlargement is reduced to 0.55 and 0.75 km, respectively.

The forward model of the retrieval algorithm discussed in Chapter 3 implies the possibility of performing an integration over a given height extension in the radiative transfer calculations. In the case of solar occultation, there are no significant differences in the retrieval results.

7.2.3 Horizontal Inhomogeneities

A single occultation measurement contains only information from the airspace along the line of sight. This can be described mathematically by the optical depth τ defined in Equation 3.20. The special case of occultation geometry yields Equation 3.23 for τ . The radiative transfer model introduced in Chapter 3 assumes a horizontally homogeneous atmosphere, i.e. trace gas concentrations are assumed

to be constant within a spherical shell. In Figure 7.5, it can be seen that this

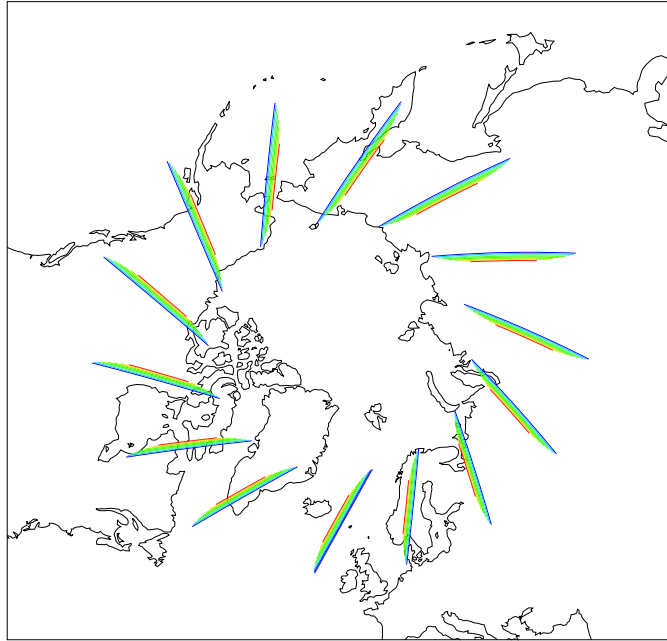


Figure 7.5: Lines of sights through the atmosphere from first to second point of intersection with the top of atmosphere. Each orbit of one day is represented by a bundle of consecutive measurements.

assumption can only be a rough approximation. A one day measurement scheme with 14 orbits is shown. Each orbit is represented by bundles of consecutive lines of sight as they typically occur during an occultation scan. The lines are plotted from the first to the second point of intersection with the top of atmosphere, which is defined to be 100 km high.

Horizontal inhomogeneities can be separated into two classes. First, they can occur at the terminator between day and night due to increasing or decreasing photochemical reaction rates. Especially, solar occultation measurements are affected by the diurnal cycles of photoactive species. Secondly, large scale dynamic activities can produce strong horizontal gradients of trace gas concentrations e.g. at the polar vortex. Claudia Emde investigated possible impacts of horizontal inhomogeneities on the optical depth τ . A detailed discussion can be found in [Emde, 2001]. Some important results are presented in this section. Investigations about the impact of horizontal inhomogeneities on retrieval results still need to be carried out.

Photochemistry

The following investigations on photochemistry are based on calculations performed with the photochemistry model BRAPHO* (BRemen Atmospheric PHOtochemical model). This model is capable of simulating atmospheric chemistry with respect to solar zenith angles. In [Emde, 2001], NO₂ and BrO concentrations were investigated considering solar zenith angles that occur in the solar occultation geometry (see Figure 7.5).

NO₂ reaction cycles are discussed in Section 5.3. Equation 5.10 illustrates that the equilibrium of NO and NO₂ is significantly different for day and night. At night, NO production is reduced and NO₂ concentrations are approximately doubled. At the terminator between day and night, an occultation measurement encounters horizontally different concentration profiles. BrO concentrations are relatively small at night as bromine is mainly bound in the reservoir gases BrONO₂, HOBr and BrCl. In the daytime, the bromine is then released in photochemical reactions resulting in much higher BrO concentrations and strong horizontal gradients at the terminator.

Errors arising from the horizontal gradients are plotted in Figure 7.6. For both species, the optical depth τ has been calculated with and without taking horizontal variations into account. Calculations without variations were performed for different solar zenith angles at the tangent point. It turned out that the more accurate model differs by up to 40 % from that calculated for a SZA of 90° at the tangent point. The errors increase rapidly for tangent heights below 30 km. In the case of NO₂, the errors can be minimised assuming a SZA of 93° instead of 90° for the simple model. For BrO, a SZA of 90° is the best approximation.

Dynamics

Horizontal gradients of trace gas concentrations can also be generated by dynamic processes in the atmosphere. One of the best-known events is the so-called polar vortex, which occurs during winter time at the poles. It is caused by winds that are bent by the Coriolis force. Details about the dynamic properties of the atmosphere can be found in [Eichmann, 2001]. Consequences of dynamic inhomogeneities in terms of occultations measurements are quite similar to the impact of the photochemistry.

Dynamic events do not occur regularly and are much more difficult to model. Therefore, an estimation of their impact can only be given in terms of statistical statements. In [Emde, 2001], deviations of optical depth τ were investigated as

*A detailed description of the model can be found in [Sinnhuber et al., 1999, Trentmann, 1997]

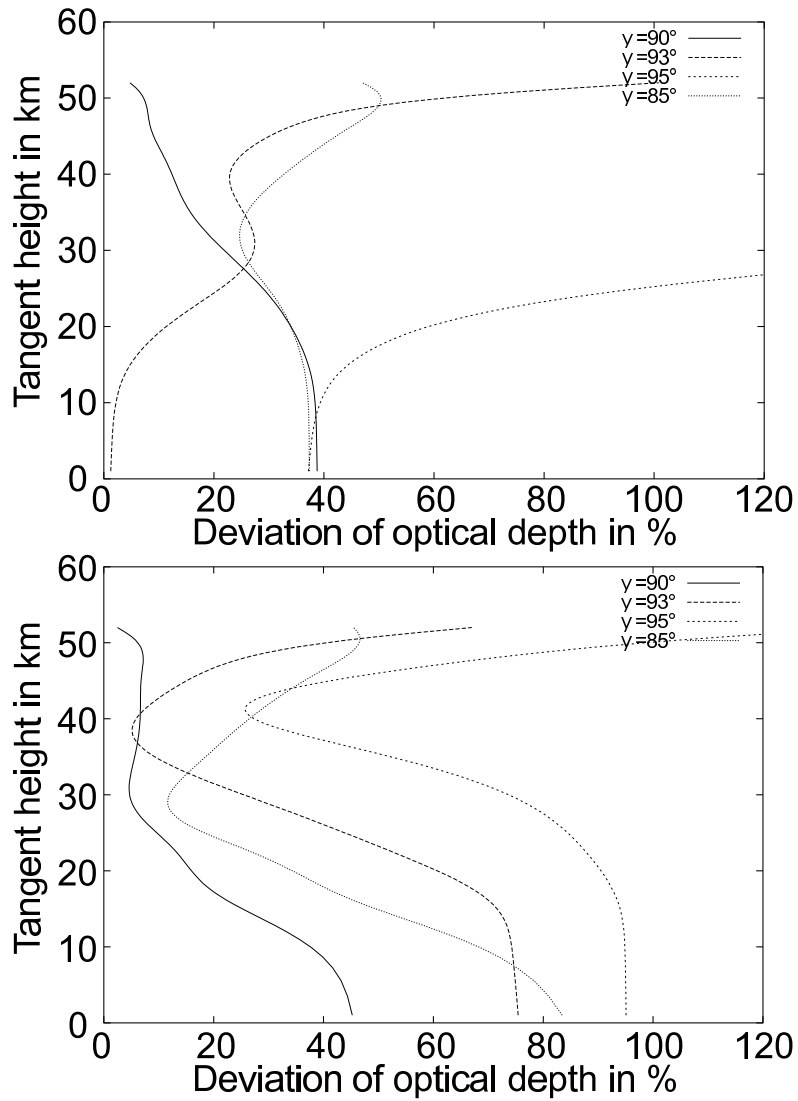


Figure 7.6: Relative errors of optical depth due to horizontal concentration gradients as function of tangent height for several solar zenith angles ψ . Top: NO₂. Bottom: BrO [Emde, 2001].

discussed above. On average, the deviations are 5 % and 3 % in the troposphere and the stratosphere, respectively. The standard deviation is in the same order of magnitude, i.e. the impact of dynamically induced inhomogeneities varies between 'no impact' and 'significant impact'.

In the future, more sophisticated a priori models will perhaps address this problem. Especially, the combination with data assimilation models discussed in Section 8.1 is very interesting in this context.

7.3 Retrieval Errors

7.3.1 Statistical Errors

The optimal estimation method as introduced in Chapter 4 yields a simple but powerful tool for the estimation of theoretical retrieval precisions. The statistical analysis of the retrieval results is comprised in the covariance matrix $\hat{\mathbf{S}}$ as defined in Equation 4.7. The diagonal elements of $\hat{\mathbf{S}}$ represent the theoretical precision of the retrieved vertical profiles with respect to each layer of the applied height grid. The theoretical precisions are the optimal estimation between measurement errors and the covariances of the a priori profile. The off-diagonal elements represent cross correlations between different height layers or even between different atmospheric parameters of the result vector $\hat{\mathbf{x}}$. These correlations are already defined by the a priori covariance matrix \mathbf{S}_a . However, in the retrieval practice only the off-diagonal elements close to the diagonal are relevant as they are defined by the correlation length h_c in Equation 4.27. Nevertheless, correlations between different species due to chemical reactions are a matter of fact, which might be interesting in combination with the data assimilation (see Section 8.1).

Measurement errors are given by the signal-to-noise ratios of the detector pixels, which are represented by the diagonal elements of the measurement covariance matrix \mathbf{S}_y . The signal-to-noise ratio (SNR) is discussed in Section 3.4.1. The SNR depends strongly on tangent height and wavelength. Therefore, it is theoretically necessary to keep \mathbf{S}_y up to date in each retrieval run. However, since the SNR is relatively high in most cases, the effect of a variable SNR on the retrieval result is small. So far, only constant SNR values between 500 and 1000 have been applied in the retrieval. Again, the off-diagonal elements representing cross correlations between the detector pixels might be provided with some physical meaning. In this study, the cross correlations are neglected and the off-diagonal elements are set to 0. Furthermore, the Twomey-Tikhonov regularisation (see Section 4.3.2) introduces additional entries to the diagonal and the nearby off-diagonal elements of $\hat{\mathbf{S}}$.

In Figure 5.2 and 5.6, the diagonal elements of the covariance matrix $\hat{\mathbf{S}}$ are represented by the error bars. The smallest relative errors are achieved at tangent heights between 20 and 30 km as predicted by theoretical studies [Rozanov, 2001]. However, the absolute values of the relative errors differ strongly from those of the theoretical studies. In some cases, the difference is approximately one order of magnitude. The different behaviour of 'real' statistical errors and the corresponding loss of information content can be explained by the following restrictions of a real data retrieval.

- Height grid does not coincide with tangent heights
- The subtraction of a low order polynomial
- A small number of measurements contributing to the retrieval
- Small fitting windows

The restrictions are mainly due to the need of stable retrieval processing and reduction of computation time. The errors show some agreement with the statistical results of the first validations, which are presented in Section 7.3.2.

7.3.2 Validation Results

Validation with SAGE-II

The most appropriate way to prove the reliability of complex retrieval algorithms is an extended validation campaign. In the course of the ENVISAT project, many validation campaigns are planned and executed around the world. In situ measurements from balloons, air planes, ships, and onground observations are suitable as well as results from other spaceborne instruments as introduced in Section 2.3. The availability of appropriate validation measurements for the SCIAMACHY occultation results is strongly limited due to the relatively poor global coverage. Good coincidences are quite rare. The first validation results for solar occultation measurements are comparisons with the SAGE-II instrument and balloon sonde measurements over Sodankylä in Finland. There were already some successful comparisons of the first ozone and NO₂ profiles shortly after the launch of ENVISAT with results of the SAGE-III and the POAM-III instruments [Meyer et al., 2004]. Additionally, the HALOE instrument will be used for further validations. SAGE-II POAM-III and HALOE have been extensively validated for their ozone and NO₂ profiles [Brühl et al., 1996, Cunnold et al., 1989, 1991, Gordley et al., 1996, Randall et al., 2003, 2002]. In this section, statistical results of the first ozone and

NO₂ validations are presented. The studies were performed in cooperation with Astrid Bracher [Bracher, 2003].

In Figure 7.7, two plots are shown concerning the statistical evaluation of com-

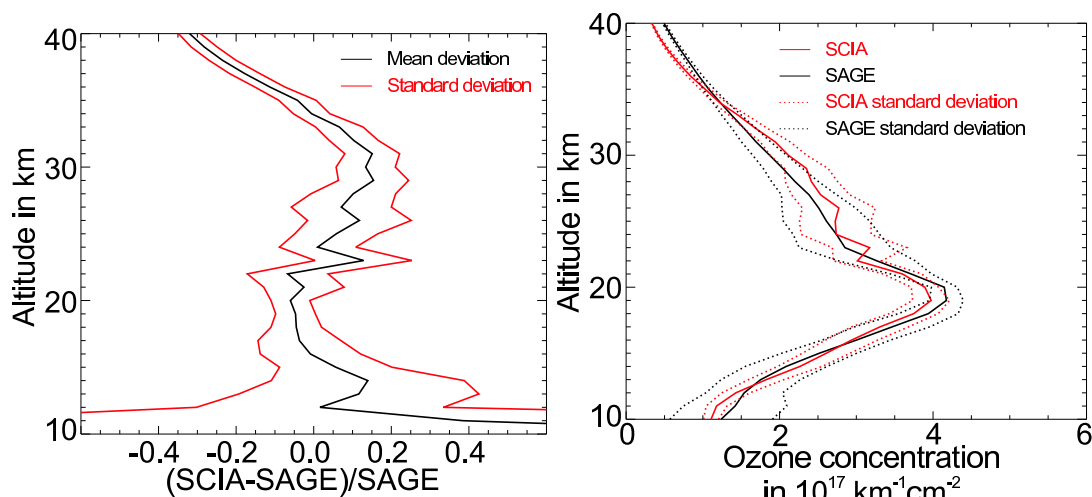


Figure 7.7: Left: Height profile of the mean deviations of ozone concentrations obtained from SCIAMACHY and SAGE measurements. Right: Average vertical ozone profiles of both instruments.[Bracher, 2003]

parisons between SCIAMACHY and SAGE-II ozone retrieval results. The validation is based on 25 single measurements. The distance between the matched occultation events is between 40 to 500 km, all between September 17th and September 22nd 2002. On the left, a height profile of the mean deviations of the retrieved ozone profiles is shown. On the right, the average profiles are compared. The mean deviation is well below 15% for the lower stratosphere and the agreement between the average ozone profiles is quite good. There is a trend towards positive differences with increasing height that cannot be explained at the moment. The statistical variations are of the order of 10%.

The corresponding results for NO₂ are presented in Figure 7.8. The results are quite similar to the ozone results. However, the tendency towards larger concentrations obtained from SCIAMACHY is constant throughout upper troposphere and lower stratosphere. The bias amounts to approximately 10%. The statistical variations are on the same order of magnitude.

The first validation results show that standard retrieval products of O₃ and NO₂ are now in good shape for further applications. Some improvements concerning the tangent height range, fitting windows etc. will certainly be possible as discussed in Section 8.2.

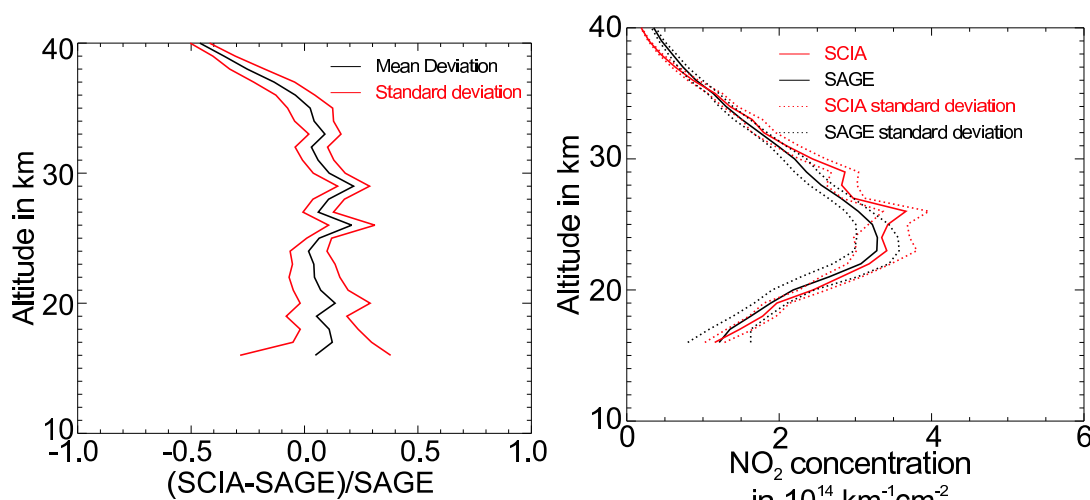


Figure 7.8: Left: Height profile of the mean deviations of NO_2 concentrations obtained from SCIAMACHY and SAGE measurements. Right: Average vertical NO_2 profiles of both instruments.[Bracher, 2003]

Comparisons with In-Situ Measurements

Some balloon-borne measurements of ozone have been compared to corresponding solar occultation measurements with SCIAMACHY. The in-situ measurements were performed by Kyrö [2002] over Sodankylä, Finland. The total number of measurements that have been compared is not sufficient for an appropriate statistical evaluation. Nevertheless, the comparisons yield some further validation of the retrieval quality.

Figure 7.9 shows all coincidences between SCIAMACHY and ozone sondes that have been evaluated so far. The overall agreement is quite good. It can be seen that the ozone sondes are much more sensitive for small scale variabilities and local differences. Nevertheless, in-situ measurements are the most accurate source of validation data.

7.3.3 Error Budget

Table 7.1 gives an overview of errors that have been discussed throughout this thesis. These errors are supposed to be the most important ones with respect to retrieval accuracy and quality. In some cases, the impact on the retrieval results can only be estimated qualitatively as detailed studies are still missing. All estimations refer to the standard retrievals of O_3 and NO_2 described in Chapter 5.

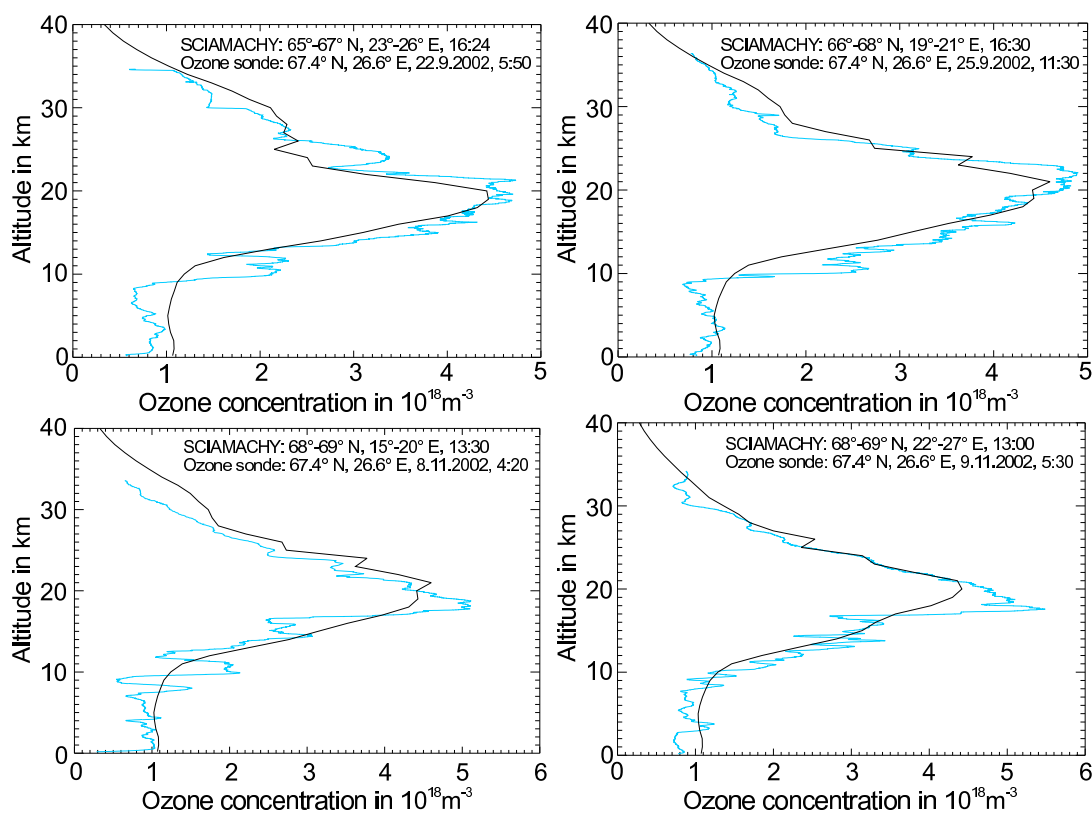


Figure 7.9: Comparisons of different balloon-borne in-situ measurements of ozone with corresponding SCIAMACHY solar occultation measurements. The ozone sonde measurements were carried out by Kyrö [2002] over Sodankylä, Finland.

Concerning the accuracy of the retrieved profiles, the deviations obtained from the validation results are the most meaningful. The deviations show a small statistical behaviour and some bias, which is height dependent in the case of ozone and around 10 % for NO_2 . The statistical deviations of the fast varying structures are less than 10 %.

The statistical errors obtained by the optimal estimation are significantly smaller as the theoretical precisions only account for the signal-to-noise ratio, the information content of the measurements, and the uncertainty of the a priori. Another important error source with mainly statistical behaviour are dynamically induced inhomogeneities of the atmosphere. At worst, they are approximately 10 %, which is on the same order as the statistical errors from the optimal estimation. The error propagation according to Gauß predicts an overall statistical error of approximately 14 % for all relevant errors with statistical behaviour.

Most of the errors given here are bias errors. As can be seen in Table 7.1, they

are negligible with the exception of the photochemically induced inhomogeneities. Furthermore, many errors will not be relevant if a polynomial is subtracted from the measurement data. Although many errors cannot be compared directly, they seem to describe consistently the limitations of the standard O₃ and NO₂ profile retrievals.

Error Description	Value	Type
Deviations from validation results		
O ₃	~ 10 %	random/bias
NO ₂	~ 15 %	random/bias
Error due to instrument noise	0.025–1 % [†]	random
Statistical errors (optimal estimation)		
O ₃	~ 5 %	random
NO ₂	≤ 10 %	random
Horizontal Inhomogeneities		
photochemical (NO ₂)	10–40 % [‡]	bias
dynamic	0–10 % [‡]	random
Uncertainties of cross-sections	≤ 3 %	random
Diffuse radiation	≪ 0.1 % [†]	bias
Increased aerosol loading (enhanced diffuse light)	≪ 1 % [†]	bias
Neglect of FOV height extension	< 2 % [†]	bias
Inhomogeneous illumination of detector	~ 1 % [§]	spectral
Wavelength shifts	~ 1 % [§]	spectral
Undersampling	~ 1 % [§]	spectral
Model errors obtained from spectral residuals		
with matching algorithm	~ 1 % [§]	bias
without matching algorithm	1–6 %	bias
Sun spots	0–10 % [¶]	bias
Global limb darkening (due to pointing errors)	~ 7 % [¶]	bias
Geometry errors		
Tangent height uncertainty		
with height retrieval	< 1 km	random
without height retrieval	1–3 km	random/bias
Height resolution	3–5 km	
Maximum pointing error	0.012°	random

Table 7.1: Error budget.

[†] Appropriate fitting window assumed, depending on tangent height and wavelength, see Section 3.4 and Section 3.3

[‡] Error on optical depth, impact on profile accuracies has not been investigated, see also Section 7.2.3

[§] Interdependencies possible, see Section 7.1

[¶] Error on measured irradiance depending on wavelength and pointing on the solar disk; not relevant if a polynomial is subtracted, see also Section 1.4

Chapter 8

Conclusion and Outlook

8.1 Applications

The scientific impact of solar occultation measurements is limited by its relatively poor global coverage. However, solar occultation measurements have a high signal-to-noise ratio and the theoretical precisions are very promising. Especially, weak absorbers at low tangent heights remain a challenging task. These virtues of the solar occultation measurements will become even more valuable if the results are combined with powerful simulation tools for atmospheric chemistry. Namely, the data assimilation yields benefits for atmospheric modeling and measurement. On the one hand, it can be used to perform some “intelligent interpolation” for the rare occultation events using knowledge about the chemical equilibriums of the considered trace gases. On the other hand, the chemical models take advantage of highly accurate data input to adjust the models with respect to trace gas concentrations. In [Fisher and Lary, 1995], it is described how data assimilation was used for the first time in the context of atmospheric chemistry. Nowadays, complex four dimensional assimilation schemes are applied and are also planned to be used for ENVISAT data, as described by Elbern and Schmidt [2001], Elbern and Klasen [2000].

In a simple linear approximation, the optimal estimation of the state vector \mathbf{x} can be expressed by the combination of measurement data and model predictions:

$$\mathbf{x} = \mathbf{x}_0 + \mathbf{G}(\mathbf{y} - \mathbf{K}(\mathbf{x}_0)). \quad (8.1)$$

\mathbf{y} , \mathbf{K} , and \mathbf{x}_0 are the measurement vector, the linearised forward model operator, and the a priori vector, respectively, as they are introduced in Chapter 4. The so-called gain matrix \mathbf{G} , which is a mathematical description of the compromise

between model and measurement, is given by

$$\mathbf{G} = \mathbf{BK}^T(\mathbf{KBK}^T + \mathbf{S}_y)^{-1}. \quad (8.2)$$

Equation 8.2 is more or less a weighting of measurement covariances \mathbf{S}_y and the covariances of the model prediction \mathbf{B} . They are linked by the forward model operator \mathbf{K} . Note that the a priori vector \mathbf{x}_0 is now a more sophisticated model prediction rather than average values from appropriate climatologies. If the measurement does not match exactly the spatial model grid, the gain matrix \mathbf{G} has to be modified. Using the knowledge of chemical models, it is possible to estimate the impact of measured species on the chemical equilibrium in a certain range around the measurement point. Therefore, this method can be used to interpolate the occultation measurements spatially. The method corresponds to a “direct insertion” of measurement information. In this simple form, some serious shortcomings may occur. It is e.g. possible that the chemical model “rejects” the measurement information due to the constraints of chemical equilibrium with species that are not measured.

A more sophisticated approach, which accounts for some of the shortcomings, is the so-called “4DVAR data assimilation”. 4DVAR stands for four dimensional variational, i.e. the evolution in time is considered together with all measurements in a given time range. The best estimation of the state vector \mathbf{x} is a trade off for all measurements and the model predictions in a least squares sense. A vital element of the 4DVAR method is the minimisation of the cost function \mathcal{J} , which is also called “objective function” or “penalty function”. \mathcal{J} accounts for all deviations between model predictions and measurements:

$$\mathcal{J}(\mathbf{x}) = 1/2(\mathbf{x} - \mathbf{x}_0)^T \mathbf{B}^{-1}(\mathbf{x} - \mathbf{x}_0) + 1/2 \sum (\mathbf{HA}(\mathbf{x}) - \mathbf{y})^T \mathbf{S}_y^{-1}(\mathbf{HA}(\mathbf{x}) - \mathbf{y}). \quad (8.3)$$

As introduced in Chapter 4, $\mathbf{A}(\mathbf{x})$ is the non-linearised forward model. The operator \mathbf{H} accounts for possible interpolations from measurement locations to the model grid. This approach takes into account one model run over a given time range and the sum of all relevant measurements. The goal is to find such initial conditions for the model run that most suitably match the measurement results. On the one hand, the 4DVAR method is a further improvement for the best estimation of the current state vector \mathbf{x} . On the other hand, the most suitable model run can also provide the most reliable predictions for future states. Therefore, the 4DVAR method has improved e.g. the weather forecasting horizon.

Solar occultation measurements are planned to be provided within the SACADA* project. As a result of this work, NO_2 and O_3 data products are considered to be ready for use in the data assimilation.

*Synoptical Analysis of Chemical constituents by Advanced satellite Data Assimilation

8.2 Open Questions

A retrieval program for occultation measurements has been developed at the Institute of Environmental Physics. It is capable of retrieving vertical profiles of several species. New correction algorithms were implemented that account for tangent height shifts and Fraunhofer structures. Nevertheless, there is still room for improvement concerning accuracies, profiles of weak absorbers, retrievals for extreme tangent heights etc. This section gives an overview of open questions that have not yet been investigated or understood. Furthermore, it is intended to outline some realistic projects that can be developed on the basis of the existing algorithms.

8.2.1 Information from Scanning

This section is a proposal for retrieving additional information from occultation measurement scans. SCIAMACHY performs usually occultation scans rather than pointing on the solar disk. In Figure 8.1, the resulting “image” of the solar disk

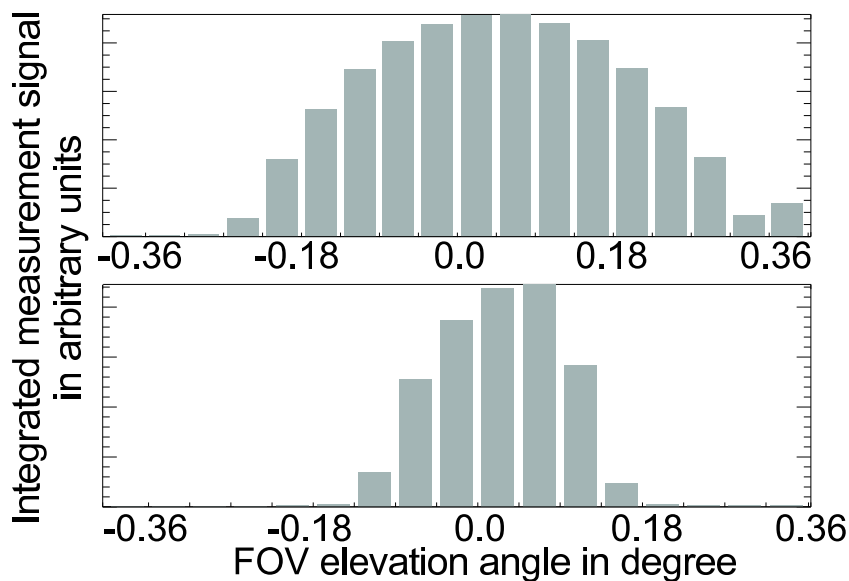


Figure 8.1: Bar plot of a solar disk image obtained by two different occultation scans at 100 km (top) and 20 km (bottom), respectively. Integrated intensities of detector counts are plotted in arbitrary units vs. relative elevation angle in degree.

is shown for tangent heights of 100 and 20 km, respectively. Intensities of the visible spectral range have been integrated and are plotted vs. relative elevation

scan angle. Each bar corresponds to a single occultation measurement. It can clearly be seen how the solar disk is flattened due to atmospheric refraction. The intensity shape can easily be fitted by a low order polynomial. The polynomial is then a function of global intensity depending on the elevation angle. It can be used to identify the solar limb. The inflection points of the polynomial are a good approximation for the solar limb.

Solar Disk Pointing

One major issue discussed in this thesis is the calculation of transmissions, which are the primary input quantity used in the retrieval process. In Section 6.2 and Section 7.1, it turned out that the information about the pointing on the solar disk is of significance for the retrieval results. The estimation of the solar limb in terms of elevation angle (see above) can be used to calculate a first guess of the pointing. In Section 6.2, an algorithm was introduced for minimising the Fraunhofer structures in the transmission spectra. A good first guess would reduce the computational costs. Therefore, a much faster retrieval algorithm is possible.

One of the most precise measurement quantities is the time of the measurement. Therefore, measurement times are very useful as a reference variable. Also the elevation angle is well known as a function of time. One occultation measurement sequence contains roughly ten useful up and down scans. Each scan yields one top and one bottom solar limb given in elevation angles at different points in time. A time series can be obtained for the top and the bottom of the solar limb, which is similar to Figure 2.2. The elevation angle of the top and bottom solar limb can now be fitted as function of time. Using this function, it is possible to calculate the solar limb for each point in time as it is needed for a good first guess calculation of the pointing on the solar disk.

Bending Angle

Another important task discussed in Section 6.2 is the bending angle of the line of sight due to atmospheric refraction. According to Equation 6.5 and Equation 6.6, the bending angle α is an exponential function of tangent height. Especially for small tangent heights, the exponential behaviour has a strong impact on the solar pointing characteristics. According to the discussion above, the height of the solar disk in terms of elevation angle $\Delta\beta$ can easily be obtained, where $\Delta\beta$ is the difference between the elevation angles of the top and bottom solar limb. From Equation 6.7, it can be deduced that $\Delta\beta$ is also given by the difference of the

corresponding bending angles $\Delta\alpha$:

$$\Delta\beta = \Delta\delta - \Delta\alpha \quad (8.4)$$

According to Section 6.2.2, $\Delta\delta$ can be identified with the apparent solar diameter, which is 0.53475° . As explained above, elevation angle β – and hence also $\Delta\beta$ – can easily be obtained as a function of time. Since $\Delta\delta$ is a constant, the differences of bending angle α with respect to the solar limb can now be expressed as a function of time. Of course, it will even be possible to calculate α directly as a function of time if one absolute value of α is known. This is the case for higher altitudes, where atmospheric refraction is negligible. Here, bending angle α is 0. Actually, the top solar limb is in the range of almost no refraction for a relatively long time during an occultation measurement scan.

A better knowledge of bending angle α will further improve the first guess for the line of sight pointing. As discussed in Section 6.2.2, it is important for the minimisation of Fraunhofer structures to estimate the seeming FOV extension. Using Equation 6.8, the seeming FOV extension can be calculated from bending angle α .

Azimuth Tracking

A complete discussion of the sun tracking must also include the pointing in the horizontal direction. Usually, the tracking in the azimuth direction is trouble-free as the azimuthal movement of the rising Sun is small and roughly constant during the measurement sequence. It can easily be calculated in advance. Furthermore, small deviations from an ideal azimuthal pointing are automatically balanced by the fact that the horizontal FOV covers an area that is significantly larger than the apparent diameter of the solar disk.

Nevertheless, the ENVISAT data processing turned out to be unreliable. Similar to the deviations in the elevation angle that are illustrated in Figure 6.3, a misalignment in the azimuth direction is observed. Figure 8.2 shows the azimuth misalignment in degree vs. occultation measurement time in seconds. As described in Section 2.1.2, the azimuth mirror moves first on the basis of a precalculated azimuth pointing. After approximately half a minute, the sun-follower tracks the solar disk in the azimuth direction. At this point, the FOV is assumed to be correctly aligned with the solar disk in the horizontal direction. The point of azimuth sun tracking can clearly be identified in Figure 8.2. A general deviation from the precalculated azimuth pointing of approximately 0.1° was also observed in many other cases. This value is slightly too large to be balanced out by the horizontal FOV extension. In the case of a correct alignment, the FOV covers the solar disk, which has an apparent diameter of 0.53° , and some additional “blue sky” of

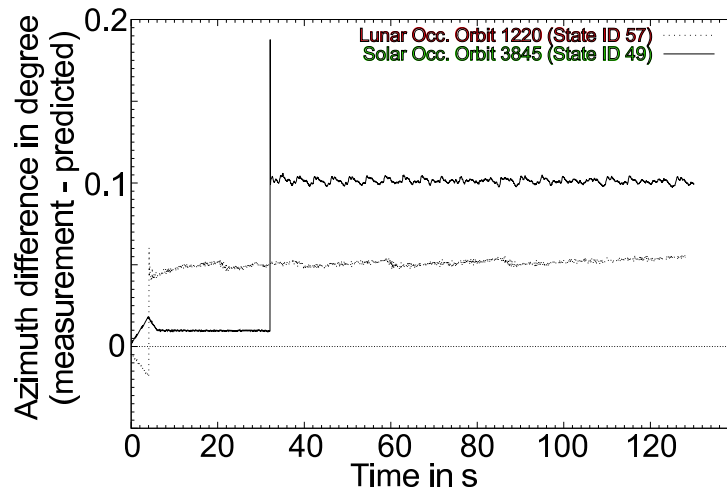


Figure 8.2: Azimuth misalignment of SCIAMACHY vs. occultation measurement time.[Noel, 2003].

$1/2(0.7^\circ - 0.53^\circ)$ on each side of the Sun. Therefore, the solar disk is probably not matched completely during the first phase of an occultation sequence. However, the missing piece of the Sun is small and it is difficult to investigate the impact on the measured spectra. Unfortunately, it cannot be ruled out that the residual of the spectral fittings is partly caused by the azimuth misalignment.

8.2.2 Accuracy of Profile Retrieval

Some efforts have already been made to improve the quality of solar occultation profile retrieval. It is shown in Chapter 6, that the retrieval results are significantly improved by the tangent height retrieval and the matching algorithm. Nevertheless, retrieval accuracy can additionally be optimised as discussed in Chapter 7.

Extended Shift and Squeeze

In Section 7.1, it is said that it is still difficult to remove the Fraunhofer structures for measurements close to the solar limb at low tangent heights. One possible reason are wavelength shifts as discussed in Section 7.1.2. Usually, the shift and squeeze algorithm helps to overcome any kind of wavelength shifts. However, in the case of the solar matching algorithm, the shift and squeeze is very likely to fail. Currently it is applied to the spectral data before the shift and squeeze is performed in the course of the actual retrieval process. Therefore, if the wavelength shifts are

strong, as in the case of low tangent heights, the solar matching routine will not be able to work properly.

A possible solution to this problem might be attained performing shift and squeeze and solar matching at the same time. Eventually, the solar matching routine is mainly a “shifting” algorithm as well. Of course, the shifting is a spatial parameter rather than a wavelength parameter. However, this makes no difference mathematically. Both algorithms can be combined theoretically.

Weak absorbers

The performance of the retrieval algorithm is also important for the possible retrieval of weak absorbers. In this context, weak absorber means that either the absorption cross sections are relatively weak or that the concentrations of the species are comparably small. Usually, it is the combination of both properties that reduces the spectral signals such that they are hard to evaluate.

Especially in the UV wavelength region, species such as BrO and OClO seem to meet the theoretical limits of the solar occultation measurements. Here, the signal-to-noise ratio, which marks the theoretical limit, is decreasing rapidly towards smaller wavelengths, as discussed in Section 3.4.1. Furthermore, the Fraunhofer lines are stronger at shorter wavelengths. Comparing the results of the signal-to-noise studies to the cross sections of weak absorbers in Appendix B, it is clear that a successful evaluation must compromise about tangent heights and fitting windows. A promising approach is the integration of directly adjacent measurements or measurements that coincide around the same tangent height due to the scanning. Mathematically, it means that the interesting absorption signals are added up whereas the signal-to-noise ratio is increased. Combining two measurements for evaluation will roughly enhance the signal-to-noise ratio by a factor of approximately $\sqrt{2}$.

In the IR wavelength range, trace gas retrieval is expected to be easier. The signal-to-noise ratio is fairly high and disturbing Fraunhofer lines are weaker than in the UV and visible range.

Photoactive Species

In Section 7.2.3, the impact of horizontally inhomogeneous trace gas concentrations is discussed. So far, only the optical depths have been investigated. A detailed study about the impact on retrieval results is still missing. In principle, solar occultation measurements contain enough information to account for horizontally varying species. The standard retrieval of NO₂, which is a relatively strong absorb-

ing species, does not need the information of all measurements performed during a measurement sequence. So the NO_2 retrieval might be extended using a more sophisticated model with two or more a priori profiles. Since the diurnal cycles of photoactive species can be modeled quite accurately, it is no problem to provide the forward model with more detailed a priori knowledge. Unfortunately, such changes will result in elaborate programming work.

Weaker photoactive absorbers such as BrO are much more difficult to address with respect to their horizontal inhomogeneities. As mentioned above, it is not clear if they can be detected at all. It is possible that all the information content of the measurements are needed to get at least one reasonable profile rather than several horizontally varying profiles.

8.2.3 Extreme Tangent Heights

Upper Stratosphere and Mesosphere

“Extreme height” means the height ranges below 15 km or above 45 km. In the upper stratosphere and lower mesosphere, the absorption signals decrease rapidly with height, mainly due to the general decrease of air density. Currently, there are two main tasks in this region: the detection of noctilucent clouds (NLC) and the retrieval of mesospheric ozone. NLCs have already been detected by SCIAMACHY in the limb viewing geometry as described by Christian von Savigny [von Savigny et al., 2003]. In the limb viewing geometry, the backscatter signal of the clouds is used for detection. However in occultation geometry, a successful detection depends on the extinction by the clouds. The extinction signal must be greater than the noise, which has not yet been investigated. The signal itself is expected to be a broadband extinction without any differential structures. Also the extinction of mesospheric ozone is too weak in the Chappuis bands. Therefore, a retrieval of mesospheric ozone has to focus on the strong UV absorption bands, which partly have only weak differential structures. So it is understood that the retrieval strategy has to be changed. An approximate way to fit non-differential structures, is the fitting of absolute transmission values. In terms of the current retrieval algorithms, this means that the subtraction of a low order polynomial from the transmission spectra must be omitted. Unfortunately, it is nearly impossible to obtain the necessary absolute transmissions due to the scanning. Although the circular shape of the solar disk is completely unaffected in this height range, it is still not possible to create a perfect matching between atmospheric and reference measurements. Since SCIAMACHY’s field of view covers an area greater than the apparent diameter of the Sun, every small deviation from the estimated pointing position results in significant changes of the pretended absolute transmission. It

is illustrated in Figure 6.7. Nevertheless, it might be possible to take advantage of the general wavelength dependence of extinction, i.e. the slope of the transmission spectra. The slope is not affected by the pointing problems. However, to adapt these spectral features to the retrieval algorithm, further development of the retrieval algorithms is needed.

Troposphere and Lower Stratosphere

In this height range, difficulties turn into the opposite. The number of relevant absorbers with overlapping extinction characteristics is much higher and the spectral signals are very strong. In some cases such as the O₂-A band, the absorption runs even into saturation for small heights. Additionally, highly variable atmospheric extinction leads to apparent wavelength shifts, as discussed in Section 7.1.2. Finally, transmission spectra at low tangent heights show very strong Fraunhofer structures. The following tasks have to be taken into account in order to optimise the retrieval results in this height range.

- Spectral fitting windows have to be optimised with respect to the extinction signals. Saturation must be avoided. Overlapping species have to be separated or fitted at the same time.
- The solar matching algorithm introduced in Section 6.2.3 has to be improved. Retrieval of weak absorbers might be significantly disturbed by the remaining Fraunhofer structures. A first step is the discussion in Section 8.2.2.
- Errors for photoactive species discussed in Section 7.2.3 are much stronger at low tangent heights. In order to obtain reasonable results, it is necessary to extend the retrieval algorithm. See also Section 8.2.2.
- Even strong absorbers have weak absorption properties in the extreme height ranges as their concentrations drop drastically compared to the profile maximum. So the discussion of weak absorbers in Section 8.2.2 has also to be taken into account.

8.2.4 Retrieval of Temperature and Pressure

Using Oxygen Retrieval

Mathematically, temperature and pressure can be considered as atmospheric parameters such as trace gas concentrations and aerosol properties. As shown in Chapter 3, they are usually needed within the forward model to calculate trace

gas extinctions. Theoretically, the retrieval can be performed the other way round. Assuming well known trace gas profiles, temperature and pressure can be retrieved. The O₂-retrieval, as it is discussed in Section 6.1, is such an ambivalent example. Here, the retrieval was used to improve the information on the tangent heights assuming the O₂ concentration, pressure and temperature profiles to be well known. If the information about the line of sight were perfect, the O₂-retrieval could be used for a retrieval of pressure and temperature. Equation 6.1 is then used in the opposite direction.

Using Rayleigh Scattering

The molecular scattering is proportional to λ^{-4} . In a wavelength window with negligible trace gas absorption, the molecular scattering is the dominant extinction process. The slope of the transmission spectra is mainly formed by the Rayleigh scattering. As mentioned in Section 8.2.3, it is no problem to compare the slope of transmission spectra at different tangent heights. With some a priori knowledge about the pressure and temperature profile and the resulting molecular density, it is then possible to retrieve exact values for molecular concentrations. Via the ideal gas law, it is a retrieval of pressure and/or temperature.

Using the Bending Angle

In Section 8.2.1, it is shown how the bending angle α can be obtained as a function of measurement time. On the other hand, the bending angle depends directly on the molecular density, which is in turn a function of pressure and temperature. It is possible to construct a forward model that combines pressure and temperature profiles with α as a function of height. This model can be used for a retrieval of both parameters.

8.3 Outlook

8.3.1 Scanning or Pointing?

It was explained in Chapter 2 how the two different measurement strategies work in occultation geometry. Some of the occultation instruments mentioned in Section 2.3 use the scanning method and some are using the pointing method. SCIAMACHY is capable of performing in either mode though the nominal occultation modes are mainly scanning modes. It is very difficult to give a clear answer to the

initial question. From my point of view, there is only one thing that is safe to say: The retrieval algorithms depend strongly on the applied measurement strategy.

At first sight, there should be no difference as the calculation of atmospheric transmissions and their further evaluation are the basic part in both cases. However, it is shown in this thesis that the impact of remaining Fraunhofer lines cannot be neglected. Pointing and scanning mode both suffer from this problem, but in different ways. The Fraunhofer problem and its solution in the scanning mode are widely discussed in Section 6.2 and Section 7.1. The pointing mode is less affected by the Fraunhofer problem. Nevertheless, it is still significant as it is impossible to point always onto the centre of the solar disk. Due to the sun flattening and vertically increasing extinction in the atmosphere, the brightest point of the solar disk does not coincide with the solar centre. The problem of tracking the flattened Sun is discussed for the POAM instrument in [Glaccum et al., 1996] and more detailed in [Lumpe et al., 1997], which has very similar FOV characteristics compared to SCIAMACHY. As a result of these considerations, it is clear that different pointing algorithms have to be implemented for the different measurement strategies.

Another difference between scanning and pointing mode turns out to be a virtue for the pointing mode. As discussed in Section 8.2.3, it is nearly impossible to obtain absolute transmission values from atmospheric measurements in the scanning mode, even for higher altitudes. In principle, the pointing mode is not free of this problem. However, at tangent heights above 40 km, the brightest point of the Sun coincides very well with the solar centre. Furthermore, the error due to a possible misalignment is very slowly changing. Only at low tangent heights, the misalignment increases more rapidly.

A clear advantage of the scanning mode is the possibility to determine the solar limb in terms of elevation angle, as described in Section 8.2.1. Unfortunately, the potential of this additional information content has not been investigated so far. Depending on the results in the near future, the decision between pointing and scanning has to be considered carefully. In my opinion, the scanning mode offers more interesting and challenging tasks – at least for the near future with SCIAMACHY.

8.3.2 Occultation vs. Limb

Since occultation measurements have only poor spatial and temporal coverage, it if such measurements will keep competitive compared to other viewing geometries is a displeasing but legitimate asking. First, one should have a look at the supposed advantages of occultation measurements:

- Atmospheric parameter retrieval with high vertical resolution
- Retrieval of trace gas concentrations with high precision
- Wide height ranges possible including the troposphere and the mesosphere
- Low computational costs due to a fairly simple radiative transfer model
- Lunar and stellar occultation are possible on the night side

It is clear that the nadir viewing geometry cannot be compared with the benefits of occultation measurements as the nadir measurements cover completely different tasks. However, the limb geometry aims at similar scientific questions. One can even say that the occultation measurements are a special case of the limb geometry. Nevertheless, occultation measurements are superior to the limb geometry theoretically in any point of the list above. Unfortunately, further efforts have to be made in order to cover all the promised advantages, as discussed throughout this chapter. Furthermore, the low computational costs will soon become a minor argument if the current increase of computing facilities continues as in the last decades. On the other hand, it is described in Section 8.1 how occultation can also turn into a powerful tool with full global coverage using the data assimilation approach. This will be investigated in the near future.

Of course, the main motivation for atmospheric measurements is still to investigate global change of atmospheric constituents and the anthropogenic impact. Nevertheless, the various spaceborne measurement techniques are a challenging and interesting science on their own.

8.4 Summary

The focus of this thesis is the evaluation of the first solar occultation measurements performed by SCIAMACHY onboard ENVISAT in the UV-vis-NIR wavelength range. Vertical trace gas concentration profiles have been retrieved from atmospheric measurement spectra, fitting the differential structures of extinction signals. An introduction is given about the foundations of the occultation geometry. The underlying studies are separated into theoretical investigations about the sensitivity of the instrument with respect to atmospheric constituents and trace gas retrievals from the first real measurement data.

It is shown that the spectrometer works as expected in occultation geometry. Spectral data have a high signal-to-noise ratio except for the UV wavelength range at low altitudes. First standard data products of ozone and nitrogen dioxide vertical profiles in the stratosphere and upper troposphere have been produced with

errors in the order of 10 and 15 %, respectively. The inversion algorithm is based on the optimal estimation method or, alternatively, on the eigenvector decomposition method. Correction algorithms have been implemented concerning the tangent height of the line of sight and the pointing on the solar disk. The radiative transfer model is based on the Lambert-Beer law of extinction. The retrieval algorithm assumes the measured spectra to consist only of transmitted light rather than scattered light. Theoretical studies have been performed to demonstrate that this assumption is true. An estimation of different error sources is discussed as well.

Data pre-processing as performed by ESA such as the calculation of geolocation and tangent heights turned out to be unreliable. A general tangent height shift of approximately 2 km was observed in many data sets. An algorithm has been implemented to correct the tangent heights. It is based on the retrieval of oxygen, which is a well-mixed gas in the atmosphere. Its retrieval results can be used to adjust the measurement heights. In this context, it is shown that oxygen and carbon dioxide can be retrieved using the line-by-line method for spectral fitting of absorption structures.

Another important task for solar occultation measurements is the exact pointing on the solar disk. Only atmospheric transmissions, which are obtained from divisions by extraterrestrial reference measurements, have been used so far. Nevertheless, spatially varying Fraunhofer lines remain part of the differential spectra as the shape and the depth of Fraunhofer lines are a function of the pointing on the solar disk. Retrieval of weak absorbers can be seriously affected due to their relatively small spectral signals. An algorithm has been implemented to minimise the remaining Fraunhofer structures. It is shown that the impact of Fraunhofer lines will be reduced if atmospheric measurements are assigned to appropriate extraterrestrial reference measurements.

Nevertheless, the accuracy of the retrieval results has not yet reached its theoretical limits. Residuals of spectral fittings obtained by the retrieval process are greater by one order of magnitude than expected from signal-to-noise considerations. Especially, measurements at low tangent heights show spectral artefacts, mainly related to Fraunhofer structures. Different reasons such as wavelength shifts, undersampling, and inhomogeneous illumination of the detector are discussed and possible solutions for the future are suggested. Validation studies with results of the SAGE-II and POAM-III occultation instruments as well as balloon sonde measurements show deviations of approximately 10 % and 15 % for ozone and NO₂, respectively.

8.5 Deutsche Zusammenfassung

Der Schwerpunkt dieser Arbeit liegt in der Auswertung der ersten Sonnen-Okkultations-Messungen des satellitengetragenen Fernerkundungs-Sensors SCIAMACHY. SCIAMACHY misst Strahlung im UV-vis-NIR Wellenlängen-Bereich. Es wurden vertikale Profile von Spurengas-Konzentrationen aus gemessenen atmosphärischen Spektren ermittelt, indem die differentiellen Strukturen der Extinktions-Signale spektral angepasst wurden. Es wird eine Einführung gegeben zu den Grundlagen der Okkultations-Geometrie. Es wird gezeigt, dass das Spektrometer in Okkultations-Geometrie wie geplant funktioniert. Erste Standard-Datenprodukte von Ozon- und Stickstoffdioxid-Vertikalprofilen wurden erstellt für die Stratosphäre und die obere Troposphäre. Der Inversionsalgorithmus basiert auf der Optimal-Estimation-Methode. Es wurden zusätzlich Algorithmen implementiert zur Korrektur der Tangentenhöhen und der Blickrichtung auf der Sonnenscheibe. Das Strahlungstransfermodell basiert auf dem Extinktionsgesetz von Lambert-Beer. Für die Auswertung wird davon ausgegangen, dass die gemessenen Spektren nur transmittiertes Licht enthalten und keine mehrfach gestreuten Anteile. Theoretische Studien wurden durchgeführt, um dies zu belegen. Eine Abschätzung verschiedener Fehlerquellen wird ebenso diskutiert.

Die präprozessierten Daten der ESA stellten sich als unzuverlässig heraus, insbesondere die Berechnung der Tangentenhöhen der Sichtlinien. Eine allgemeine Verschiebung der Höhen von etwa 2 km wurde in einer Vielzahl von Datenpaketen beobachtet. Um die Tangentenhöhen zu korrigieren, wurde ein Algorithmus implementiert, der auf der Auswertung von Sauerstoff-Vertikalprofilen aufbaut. Sauerstoff ist ein gut durchmisches Gas der Atmosphäre, daher können die ermittelten Profile genutzt werden, um die Tangentenhöhen abzugleichen. In diesem Zusammenhang konnte auch gezeigt werden, dass O_2 und CO_2 in hinreichender Genauigkeit ausgewertet werden können.

Ein anderer wichtiger Aspekt für Sonnen-Okkultations-Messungen ist die genaue Blickrichtung bezüglich der Sonnenscheibe. Zwar werden nur Transmissions-Spektren zur Auswertung benutzt, dennoch bleiben räumlich variable Fraunhofer-Linien in den differentiellen Spektren übrig, wodurch die Auswertung schwacher Absorber beeinträchtigt werden kann. Ein Algorithmus zur Beseitigung dieser Strukturen wurde implementiert und es konnte gezeigt werden, dass der Einfluss deutlich reduziert werden kann, wenn die atmosphärischen Messungen zu einer passenden Referenz-Messung oberhalb der Atmosphäre zugeordnet werden.

Validations-Studien wurden durchgeführt mit den Resultaten anderer satellitengetragener Okkultationsinstrumente sowie Messungen von Ballon-Sonden. Es ergaben sich hier Abweichungen von etwa 10 % bzw. 15 % für O_3 und NO_2 .

Appendix A

Fraunhofer Lines

This section gives an overview of all important Fraunhofer lines within the SCIAMACHY spectrum. Fraunhofer lines can lead to significant fitting errors in the solar occultation retrieval process (see Section 7.1.1). Table A.1 has been compiled by Marco Vountas [Vountas, 1998]. The table is based on several solar atlases described in [Vuorilehto and Korpela, 1994]. An introduction to the physics of Fraunhofer lines can be found in Chapter 1.

λ [nm]	Name						
237.5200	CoI	238.2030	FeII	238.8650	FeII	239.5250	FeI
240.4660	FeII	242.5640	ML*	246.2650	FeI	247.2910	FeI
247.9770	FeI	248.3430	FeI	249.3280	FeI	256.6910	FeII
257.6120	MnII	257.7910	MgI	258.5900	FeI	259.3720	FeII
259.9395	ML*	260.7090	FeII	261.1890	FeII	261.3850	FeII
263.0070	MgI	266.6010	CrII	267.9060	FeI	268.9200	CrII
268.9830	ML*	272.0900	FeI	272.7550	FeII	273.9560	FeII
274.2400	SL [†]	274.9320	SL [†]	276.1730	SL [†]	277.9840	SL [†]
279.5400	MgII	280.2300	MgII	285.2130	MgI	287.5300	FeI
288.1580	SiI	288.3720	SL [†]	292.9020	FeI	293.6910	FeI
293.9300	MnII	294.7890	FeI	294.9210	FeII	295.3930	FeI
295.7360	FeI	296.6910	FeI	297.3130	FeI	297.3230	FeI
298.3590	FeI	299.4430	FeI	299.4500	FeI	300.8130	FeI
300.9560	FeI	302.0490	FeI	302.0630	FeI	302.1070	FeI
302.5866	FeI	303.7396	FeI	304.0430	FeI	304.7614	FeI
305.9094	FeI	306.6501	ML*	306.7262	ML*	308.2168	All

continued on the next page

*ML: Many lines

[†]SL: Some lines

<i>Fraunhofer lines continued</i>							
λ [nm]	Name	λ [nm]	Name	λ [nm]	Name	λ [nm]	Name
308.3749	FeI	309.1071	MgI	309.2851	ML*	309.6902	MgI
309.9896	FeI	310.0325	FeI	313.4116	FeI	314.3760	ML*
315.7031	FeI	315.8886	CaII	317.9342	CaII	318.0720	SL [†]
319.0899	SL [†]	328.6772	FeI	332.2949	TiII	332.6777	TiII
333.2150	SL [†]	333.6689	MgI	334.9447	TiII	336.1193	TiII
338.0585	NiI	339.2978	NiI	341.4779	NiI	344.0626	FeI
344.1019	FeI	346.5880	FeI	347.5757	FeI	349.0594	FeI
349.2975	FeI	349.7843	FeI	351.5825	NiI	352.4536	NiI
353.3203	FeI	356.5396	FeI	356.6383	NiI	357.0134	FeI
358.1209	FeI	360.8869	FeI	361.8777	FgI	361.9400	NiI
363.1475	SL [†]	364.7851	FeI	368.7466	FeI	370.5577	FeI
371.9947	FeI	372.7634	FeI	373.4370	H	373.7141	FeI
374.9494	FeI	375.0150	H	375.8245	FeI	376.3803	FeI
376.7204	FeI	377.0630	H	379.7900	H	379.9558	FeI
380.6718	MnI	381.5851	FeI	382.0436	FeI	382.5891	FeI
382.7832	FeI	383.2310	MgI	383.5390	H	383.8302	MgI
384.9977	FeI	385.6381	FeI	385.9992	FeI	387.2510	FeI
387.8027	FeI	387.8580	FeI	388.6294	FeI	390.5532	SiI
392.2923	FeI	393.3682	CaIIK	394.4016	AlI	396.1535	AlI
396.8492	CaIIH	400.5354	FeI	403.0753	MnI	403.3072	MnI
404.5825	FeI	406.3605	FeI	407.1749	FeI	407.7724	SrI
410.1748	H _{δ}	413.2067	FeI	414.3878	FeI	421.5539	SrII
422.6740	CaI	423.5949	FeI	425.0085	FeI	425.0750	MgII
425.4346	CrI	426.0486	FeI	427.1164	FeI	427.1774	FeI
432.5775	FeI	434.0475	H _{γ}	438.3557	FeI	441.5135	FeI
458.1450	SL [†]	470.3003	MgI	486.1342	H _{β}	489.1502	FeI
491.8998	FeI	492.0514	FeI	495.7610	FeI	507.8981	FeI
507.9965	FeI	516.7508	SL [†]	517.2698	MgI	518.3619	MgI
522.6870	FeI	522.7192	FeI	537.1501	FeI	544.6924	FeI
552.8418	MgI	558.6771	FeI	560.2969	FeI	561.5658	FeI
585.8459	CaI	588.9973	NaI	589.5940	NaI	612.2226	CaI
616.2180	CaI	623.0736	FeI	630.1508	FeI	640.0009	FeI
646.2570	CaI	656.2808	H _{α}	741.1162	FeI	746.2342	CrI
778.0568	FeI	783.2208	FeI	791.8383	SiI	793.7150	FeI
799.8953	FeI	838.7782	FeI	849.8062	CaII	854.2144	CaII
866.2170	CaII	868.8642	FeI	873.6040	MgI	877.2884	AlI
879.3350	FeI	880.6775	MgI	882.4234	FeI	886.6943	FeI
889.2738	SiI	892.7392	CaII	902.4380	FeI	902.4700	FeI

continued on the next page

<i>Fraunhofer lines continued</i>							
λ [nm]	Name	λ [nm]	Name	λ [nm]	Name	λ [nm]	Name
925.5790	MgI	925.8280	FeI	931.8220	FeI	943.8730	MgI
946.2940	FeI	988.9050	FeI	1058.5137	SiI	1060.3426	SiI
1066.0990	SiI	1072.7420	SiI	1074.8390	SiI	1078.4570	SiI
1078.6850	SiI	1081.1140	MgI	1082.7140	SiI	1084.3880	SiI
1097.9340	SiI	1098.2100	SiI	1111.9810	FeI	1140.3800	NaI
1142.2380	FeI	1159.1410	SiI	1159.3650	FeI	1160.7590	FeI
1174.8280	Cl	1175.3420	Cl	1182.8240	MgI	1188.4130	FeI
1203.4810	SiI	1227.4050	SiI	1239.3554	SiI	1239.9225	SiI
1268.2620	NaI	1282.1614	H	1310.5644	SiI	1312.7028	AlI
1315.4381	AlI	1329.7483	MnI	1332.2711	MnI	1332.9281	SiI
1451.6169	Fe	1475.3810	FeI	1487.6060	NiI	1504.4358	MgI
1556.2046	SiI	1572.7894	FeI	1632.0775	FeI	1644.9316	FeI
1668.5326	SiI	1672.3527	AlI	1697.4557	FeI	1711.3295	MgI
1945.8319	CaI	1948.9682	FeI	1949.8689	SiI	1978.2198	CaI
1982.0427	CaI	1985.8527	CaI	1986.7642	CaI	1992.2620	CaI
1993.4376	SiI	1993.9185	CaI	1996.7293	CaI	2030.1930	SiI
2030.7496	SiI	2034.9441	SiI	2038.3994	SiI	2267.1984	SiI

Table A.1: Positions of important Fraunhofer lines

Appendix B

Cross Sections

Trace gas cross sections are fundamental to any radiative transfer calculation. Their spectral behaviour determines mainly the position and size of appropriate fitting windows in the retrieval process. Cross sections of relevant trace gases are plotted here in different wavelength regions, that are addressed by SCIAMACHY. They have been plotted by Johannes Kaiser [Kaiser, 2001].

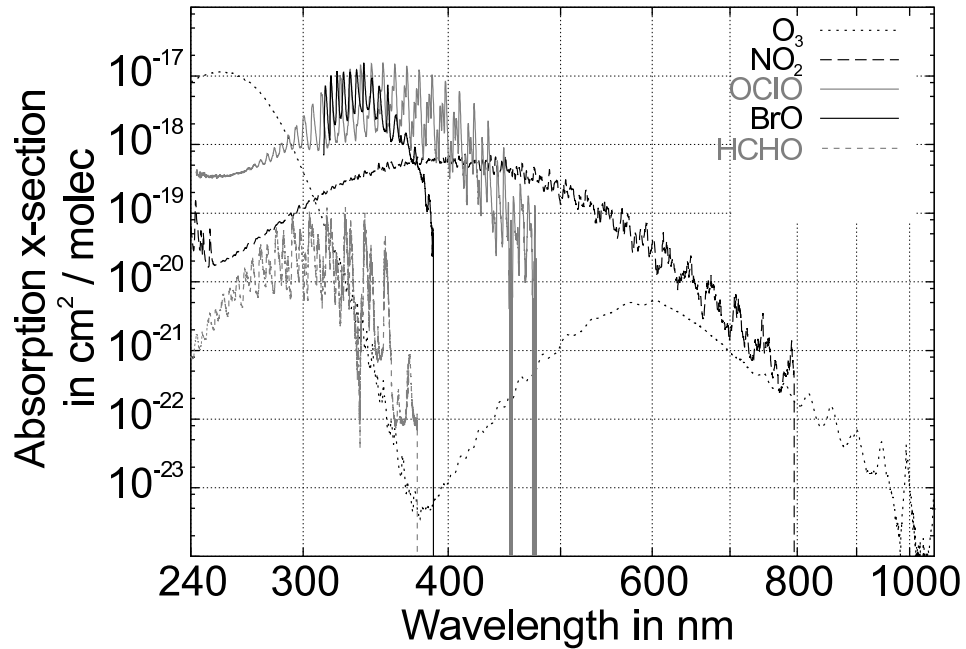


Figure B.1: Cross sections of several trace gases in the UV-vis spectral range.

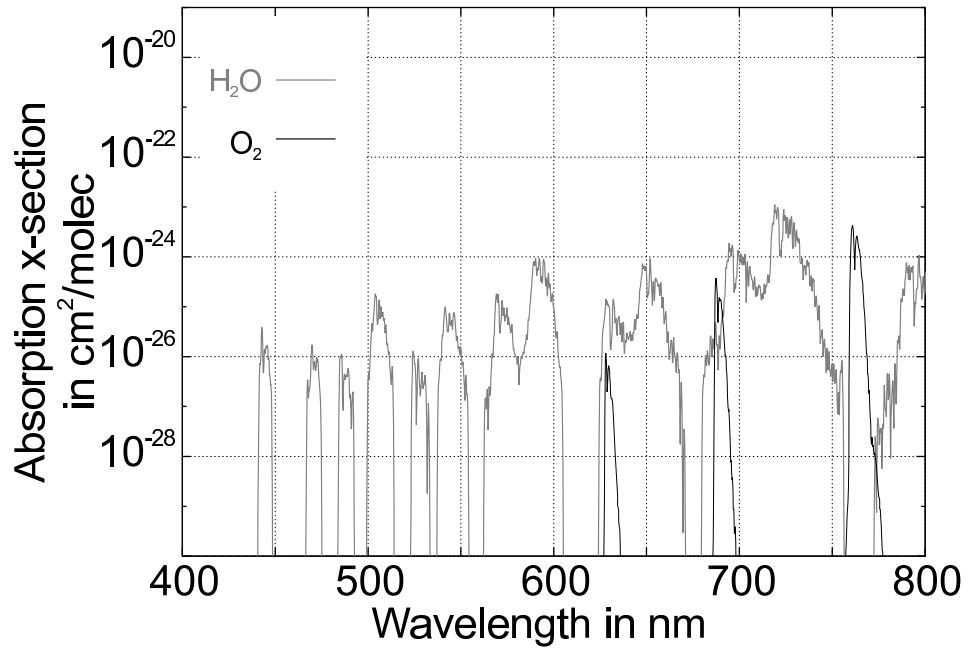


Figure B.2: Cross sections of several trace gases in the visible spectral range.

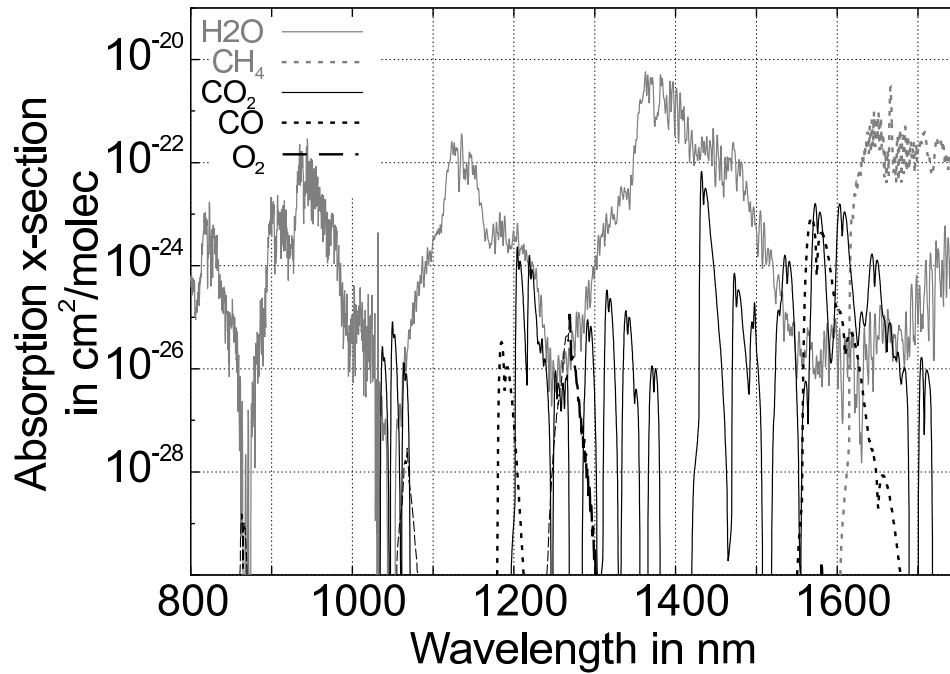


Figure B.3: Cross sections of several trace gases in the NIR spectral range.

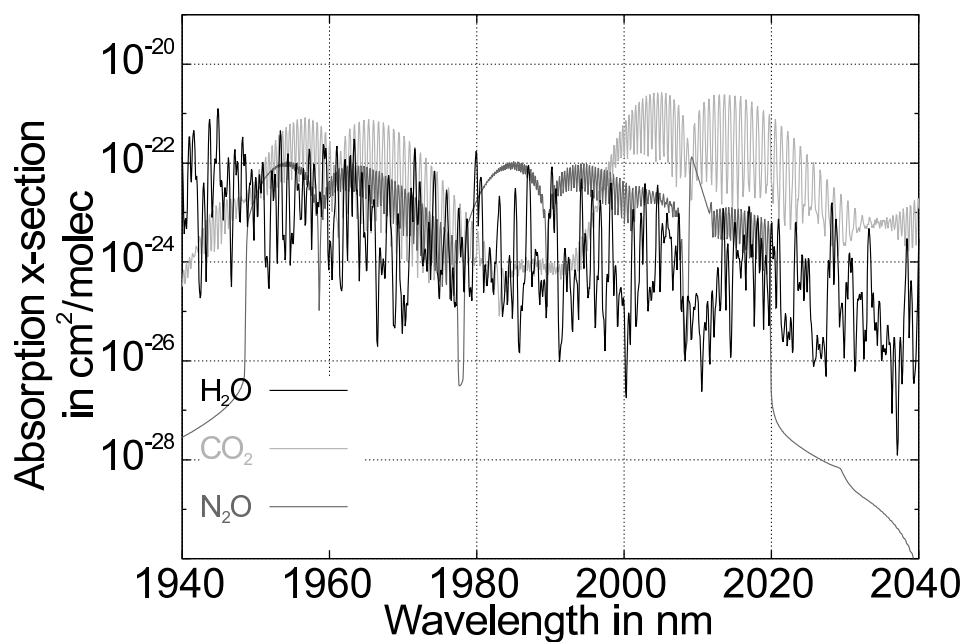


Figure B.4: Cross sections of several trace gases in the spectral range of SCIAMACHY channel 7.

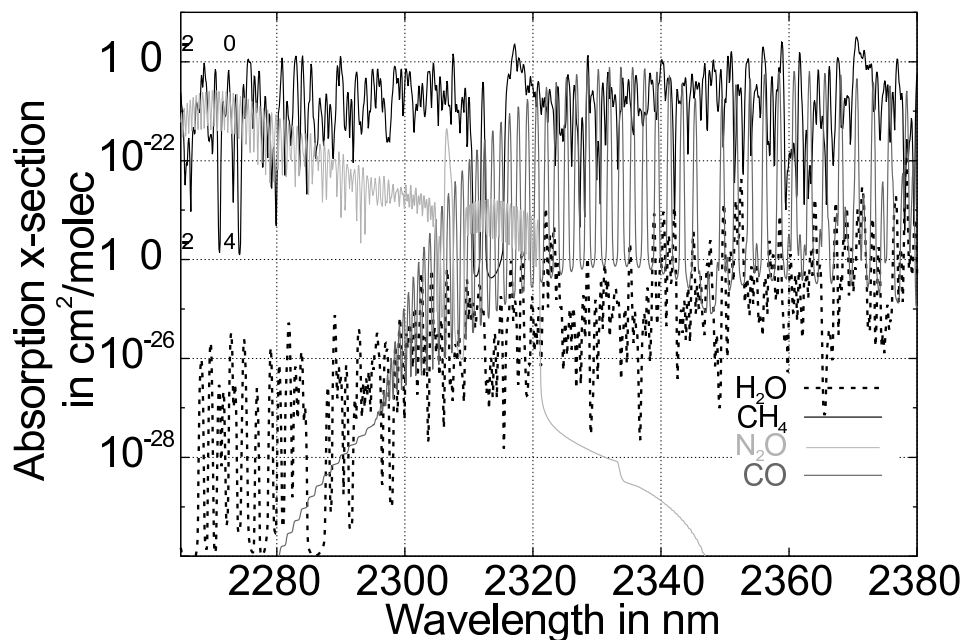


Figure B.5: Cross sections of several trace gases in the spectral range of SCIAMACHY channel 8.

Appendix C

Orbit Numbers

ENVISAT's orbit numbers are often used instead of exact date and hour. One orbit takes approximately 100 min, one day has a bit more than 14 orbits on an average. The first orbit took place directly after launch on 1st March 2002 around 3 a.m. Orbit 30.000 will be at the end of November 2007. The following table is a quick reference for finding corresponding dates and orbit numbers.

Date	Orbit	Date	Orbit	Date	Orbit
2002/03/01	0	2002/03/08	100	2002/03/15	200
2002/03/22	300	2002/03/29	400	2002/04/05	500
2002/04/12	600	2002/04/19	700	2002/04/26	800
2002/05/03	900	2002/05/10	1000	2002/05/17	1100
2002/05/24	1200	2002/05/31	1300	2002/06/07	1400
2002/06/14	1500	2002/06/21	1600	2002/06/27	1700
2002/07/04	1800	2002/07/11	1900	2002/07/18	2000
2002/07/25	2100	2002/08/01	2200	2002/08/08	2300
2002/08/15	2400	2002/08/22	2500	2002/08/29	2600
2002/09/05	2700	2002/09/12	2800	2002/09/19	2900
2002/09/26	3000	2002/10/03	3100	2002/10/10	3200
2002/10/17	3300	2002/10/24	3400	2002/10/31	3500
2002/11/07	3600	2002/11/14	3700	2002/11/21	3800
2002/11/28	3900	2002/12/05	4000	2002/12/12	4100
2002/12/19	4200	2002/12/26	4300	2003/01/02	4400
2003/01/09	4500	2003/01/16	4600	2003/01/23	4700
2003/01/30	4800	2003/02/06	4900	2003/02/13	5000
2003/02/20	5100	2003/02/27	5200	2003/03/06	5300
2003/03/13	5400	2003/03/20	5500	2003/03/27	5600
2003/04/03	5700	2003/04/10	5800	2003/04/17	5900

continued on the next page

Date	Orbit	Date	Orbit	Date	Orbit
2003/04/24	6000	2003/05/01	6100	2003/05/08	6200
2003/05/15	6300	2003/05/22	6400	2003/05/29	6500
2003/06/05	6600	2003/06/12	6700	2003/06/19	6800
2003/06/26	6900	2003/07/03	7000	2003/07/10	7100
2003/07/17	7200	2003/07/24	7300	2003/07/31	7400
2003/08/07	7500	2003/08/14	7600	2003/08/21	7700
2003/08/28	7800	2003/09/04	7900	2003/09/11	8000
2003/09/18	8100	2003/09/25	8200	2003/10/02	8300
2003/10/09	8400	2003/10/16	8500	2003/10/23	8600
2003/10/30	8700	2003/11/06	8800	2003/11/12	8900
2003/11/19	9000	2003/11/26	9100	2003/12/03	9200
2003/12/10	9300	2003/12/17	9400	2003/12/24	9500
2003/12/31	9600	2004/01/07	9700	2004/01/14	9800
2004/01/21	9900	2004/01/28	10000	2004/02/04	10100
2004/02/11	10200	2004/02/18	10300	2004/02/25	10400
2004/03/03	10500	2004/03/10	10600	2004/03/17	10700
2004/03/24	10800	2004/03/31	10900	2004/04/07	11000
2004/04/14	11100	2004/04/21	11200	2004/04/28	11300
2004/05/05	11400	2004/05/12	11500	2004/05/19	11600
2004/05/26	11700	2004/06/02	11800	2004/06/09	11900
2004/06/16	12000	2004/06/23	12100	2004/06/30	12200
2004/07/07	12300	2004/07/14	12400	2004/07/21	12500
2004/07/28	12600	2004/08/04	12700	2004/08/11	12800
2004/08/18	12900	2004/08/25	13000	2004/09/01	13100
2004/09/08	13200	2004/09/15	13300	2004/09/22	13400
2004/09/29	13500	2004/10/06	13600	2004/10/13	13700
2004/10/20	13800	2004/10/27	13900	2004/11/03	14000
2004/11/10	14100	2004/11/17	14200	2004/11/24	14300
2004/12/01	14400	2004/12/08	14500	2004/12/15	14600
2004/12/22	14700	2004/12/29	14800	2005/01/05	14900
2005/01/12	15000	2005/01/19	15100	2005/01/26	15200
2005/02/02	15300	2005/02/09	15400	2005/02/16	15500
2005/02/23	15600	2005/03/02	15700	2005/03/09	15800
2005/03/16	15900	2005/03/23	16000	2005/03/29	16100
2005/04/05	16200	2005/04/12	16300	2005/04/19	16400
2005/04/26	16500	2005/05/03	16600	2005/05/10	16700
2005/05/17	16800	2005/05/24	16900	2005/05/31	17000
2005/06/07	17100	2005/06/14	17200	2005/06/21	17300
2005/06/28	17400	2005/07/05	17500	2005/07/12	17600
<i>continued on the next page</i>					

Date	Orbit	Date	Orbit	Date	Orbit
2005/07/19	17700	2005/07/26	17800	2005/08/02	17900
2005/08/09	18000	2005/08/16	18100	2005/08/23	18200
2005/08/30	18300	2005/09/06	18400	2005/09/13	18500
2005/09/20	18600	2005/09/27	18700	2005/10/04	18800
2005/10/11	18900	2005/10/18	19000	2005/10/25	19100
2005/11/01	19200	2005/11/08	19300	2005/11/15	19400
2005/11/22	19500	2005/11/29	19600	2005/12/06	19700
2005/12/13	19800	2005/12/20	19900	2005/12/27	20000
2006/01/03	20100	2006/01/10	20200	2006/01/17	20300
2006/01/24	20400	2006/01/31	20500	2006/02/07	20600
2006/02/14	20700	2006/02/21	20800	2006/02/28	20900
2006/03/07	21000	2006/03/14	21100	2006/03/21	21200
2006/03/28	21300	2006/04/04	21400	2006/04/11	21500
2006/04/18	21600	2006/04/25	21700	2006/05/02	21800
2006/05/09	21900	2006/05/16	22000	2006/05/23	22100
2006/05/30	22200	2006/06/06	22300	2006/06/13	22400
2006/06/20	22500	2006/06/27	22600	2006/07/04	22700
2006/07/11	22800	2006/07/18	22900	2006/07/25	23000
2006/08/01	23100	2006/08/08	23200	2006/08/14	23300
2006/08/21	23400	2006/08/28	23500	2006/09/04	23600
2006/09/11	23700	2006/09/18	23800	2006/09/25	23900
2006/10/02	24000	2006/10/09	24100	2006/10/16	24200
2006/10/23	24300	2006/10/30	24400	2006/11/06	24500
2006/11/13	24600	2006/11/20	24700	2006/11/27	24800
2006/12/04	24900	2006/12/11	25000	2006/12/18	25100
2006/12/25	25200	2007/01/01	25300	2007/01/08	25400
2007/01/15	25500	2007/01/22	25600	2007/01/29	25700
2007/02/05	25800	2007/02/12	25900	2007/02/19	26000
2007/02/26	26100	2007/03/05	26200	2007/03/12	26300
2007/03/19	26400	2007/03/26	26500	2007/04/02	26600
2007/04/09	26700	2007/04/16	26800	2007/04/23	26900
2007/04/30	27000	2007/05/07	27100	2007/05/14	27200
2007/05/21	27300	2007/05/28	27400	2007/06/04	27500
2007/06/11	27600	2007/06/18	27700	2007/06/25	27800
2007/07/02	27900	2007/07/09	28000	2007/07/16	28100
2007/07/23	28200	2007/07/30	28300	2007/08/06	28400
2007/08/13	28500	2007/08/20	28600	2007/08/27	28700
2007/09/03	28800	2007/09/10	28900	2007/09/17	29000
2007/09/24	29100	2007/10/01	29200	2007/10/08	29300
<i>continued on the next page</i>					

Date	Orbit	Date	Orbit	Date	Orbit
2007/10/15	29400	2007/10/22	29500	2007/10/29	29600
2007/11/05	29700	2007/11/12	29800	2007/11/19	29900
2007/11/26	30000				

Table C.1: Orbit numbers and corresponding dates.

Appendix D

Solar Zenith Angle vs. Tangent Height

In occultation geometry, SZA at top of atmosphere and tangent height are uniquely defined by each other for every measurement. The GOMETRAN/SCIATRAN retrieval program is capable of reading geometry information from different input files. In the case of an ideal data supply, all important information is provided within the level-1 data files. Sometimes, it is necessary to provide a priori information about tangent heights or SZA. Table D.1 shows corresponding tangent heights and SZAs within the possible height range. The SZAs have been calculated for the case of a non-refractive atmosphere with Equation 2.4 and for a refractive atmosphere with the ray trace routines [Kaiser, 2001], which are part of the retrieval algorithm. Here and throughout the thesis, the refraction is calculated assuming a standard atmosphere [NASA, 1976] with average temperature and pressure profiles. Furthermore, the top of atmosphere is always assumed to be at 100 km.

Tangent height	SZA		Tangent height	SZA	
	refractive	non-refractive		refractive	non-refractive
1.0	100.035	99.951	2.0	99.984	99.907
3.0	99.933	99.863	4.0	99.882	99.818
5.0	99.830	99.773	6.0	99.778	99.726
7.0	99.726	99.679	8.0	99.673	99.632
9.0	99.620	99.583	10.0	99.567	99.534
11.0	99.514	99.484	12.0	99.460	99.435
13.0	99.406	99.384	14.0	99.352	99.333
15.0	99.297	99.281	16.0	99.242	99.228
17.0	99.187	99.175	18.0	99.131	99.121

continued on the next page

Tangent height	SZA		Tangent height	SZA	
	refractive	non-refractive		refractive	non-refractive
19.0	99.075	99.066	20.0	99.019	99.011
21.0	98.962	98.956	22.0	98.905	98.900
23.0	98.848	98.843	24.0	98.790	98.786
25.0	98.732	98.728	26.0	98.673	98.670
27.0	98.614	98.612	28.0	98.555	98.553
29.0	98.495	98.493	30.0	98.435	98.433
31.0	98.375	98.373	32.0	98.314	98.312
33.0	98.252	98.251	34.0	98.190	98.189
35.0	98.128	98.127	36.0	98.065	98.064
37.0	98.002	98.001	38.0	97.938	97.937
39.0	97.873	97.873	40.0	97.808	97.808
41.0	97.743	97.743	42.0	97.677	97.677
43.0	97.610	97.610	44.0	97.543	97.543
45.0	97.476	97.475	46.0	97.407	97.407
47.0	97.338	97.338	48.0	97.269	97.268
49.0	97.198	97.198	50.0	97.127	97.127
51.0	97.055	97.055	52.0	96.983	96.983
53.0	96.910	96.910	54.0	96.836	96.836
55.0	96.761	96.761	56.0	96.685	96.685
57.0	96.609	96.609	58.0	96.531	96.531
59.0	96.453	96.453	60.0	96.374	96.374
61.0	96.294	96.294	62.0	96.212	96.212
63.0	96.130	96.130	64.0	96.047	96.046
65.0	95.962	95.962	66.0	95.876	95.876
67.0	95.789	95.789	68.0	95.700	95.700
69.0	95.611	95.611	70.0	95.519	95.519
71.0	95.426	95.426	72.0	95.332	95.332
73.0	95.236	95.236	74.0	95.138	95.138
75.0	95.038	95.038	76.0	94.936	94.936
77.0	94.832	94.832	78.0	94.726	94.726
79.0	94.617	94.617	80.0	94.506	94.506
81.0	94.392	94.392	82.0	94.275	94.275
83.0	94.154	94.154	84.0	94.030	94.030
85.0	93.902	93.902	86.0	93.770	93.770
87.0	93.632	93.632	88.0	93.490	93.490
89.0	93.341	93.341	90.0	93.186	93.186
91.0	93.022	93.022	92.0	92.849	92.849
93.0	92.665	92.665	94.0	92.468	92.468

continued on the next page

Tangent height	SZA		Tangent height	SZA	
	refractive	non-refractive		refractive	non-refractive
95.0	92.253	92.252	96.0	92.015	92.015
97.0	91.745	91.745	98.0	91.425	91.425
99.0	91.007	91.007	100.0	90.000	90.000

Table D.1: Solar zenith angles and corresponding tangent heights calculated with and without refraction. The SZA is calculated with respect to the first intersection of SCIAMACHY's LOS with the top of atmosphere (100 km).

Appendix E

Retrieval Algorithm

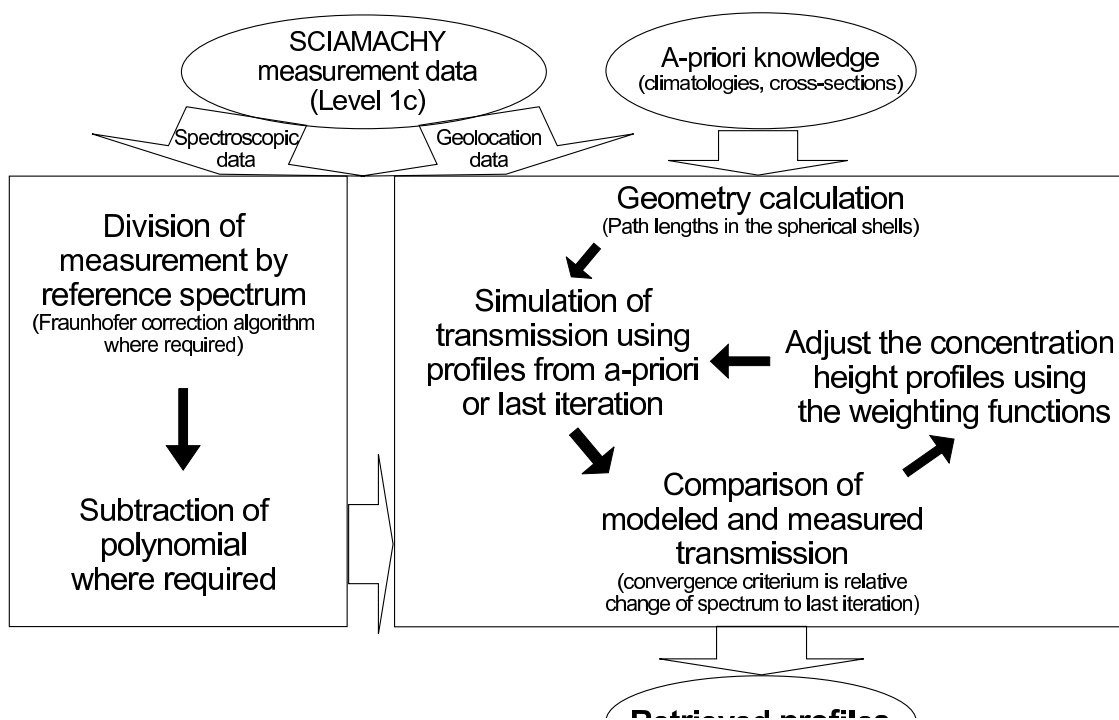


Figure E.1: Schematic view of the GOMETRAN retrieval algorithm for SCIAMACHY solar occultation data. The theoretical background is introduced in Chapter 3 and Chapter 4.

Glossary

- ACE** Atmospheric Chemistry Experiment, see Section 2.3.1
- AM/AMF** Air Mass Factor denoting the total air mass passed by radiation or single light rays
- A priori** Presumed knowledge about atmospheric states, see Section 3.1
- Averaging kernel** Derivation of retrieved state with respect to the unknown true state, see Section 4.1 and some results in Chapter 5
- BRAPHO** BRemen Atmospheric PHOtochemical model
- CFC** Chloro-Fluoro-Carbons
- CFI-Library** Customer Furnished Item, programming tools for calculation of orbital parameters and pointing geometry of ENVISAT
- Covariance Matrix** Mathematical description of error interdependencies arising from measurement errors and a priori uncertainties, see Section 4.1 and Section 7.3.1
- DOAS** Differential Optical Absorption Spectroscopy, similar to the occultation retrieval algorithm, see Chapter 3 and Chapter 4
- Ecliptic** Plane defined by the Earth's rotation around the Sun
- ENVISAT** ENVIRONMENTAL SATellite, carrier of SCIAMACHY
- ESA** European Space Agency
- Forward model** Algorithms for simulation of radiation intensities, see Chapter 3
- FOV** Field of View, see Section 2.1.2
- Fraunhofer lines** Absorption lines in the solar spectrum arising from interactions in the Sun's photosphere, see Section 1.3

- FWHM** Full Width Half Maximum, used for the spectral characterisation of detector slits, see Section 2.1.2
- GOMETRAN** Radiative transfer model designed for the purposes of atmospheric trace gas retrievals, see Chapter 3 and Chapter 4
- GOMOS** Global Ozone Monitoring by Occultation of Stars, see Section 2.3.2
- HALOE** HALogen Occultation Experiment, see Section 2.3.3
- HITRAN** High resolution TRANsmission molecular absorption database, providing optical properties of molecular absorption, see Section 3.2.1
- IFOV** Instantaneous Field Of View, see FOV
- ILAS** Improved Limb Atmospheric Spectrometer, see Section 2.3.4
- IR** InfraRed, spectral region with relatively low photon energies beyond long wave visible light
- ISS** Instrument Simulation Software, tool for simulation of measurement noise effects, see Section 3.4.1
- Keydata** Collective term for instrument related data needed for calibration issues
- LEO** Low Earth Orbiting satellites, category of satellites with orbits of up to 1000 km, see Section 2.1.1
- Level-0** Level-0 data products contain only uncalibrated detector and pixel information
- Level-1** Level-1 data products contain spectral data with different calibrations and geolocation information
- Level-2** Level-2 data products contain information about atmospheric parameters obtained from retrievals of Level-1 data
- Limb** Satellite viewing geometry for detection of scattered light, see Section 2.2.2
- Limb darkening** Wavelength dependent decrease of radiation towards the solar limb, see Section 1.4.1
- LOS** Line Of Sight, might be a curved line in a refractive atmosphere, see Section 2.2.1
- LOWTRAN** LOW resolution atmospheric TRANsmission database, providing profiles and optical properties of aerosols, see Section 3.2.1

- MAESTRO** Measurement of Aerosol Extinction in the Stratosphere and Troposphere Retrieved by Occultation, see Section 2.3.1
- MIPAS** Michelson Interferometer for Passive Atmospheric Sounding, infrared detector onboard ENVISAT
- Nadir** Satellite viewing geometry for detection of scattered light pointing directly downwards, see Chapter 2.2.2
- NIR** Near InfraRed, spectral region with less photon energies than in the visible range
- NLC** NoctiLucent Clouds, see PMC
- Noctilucent clouds** See PMC
- ORA** Occultation RAdiometer, see Section 2.3.5
- PET** Pixel Exposure Time, see Section 2.1.2
- PMC** Polar Mesospheric Clouds, typical cloud formation around 85 km altitude
- POAM** Polar Ozone and Aerosol Measurement instrument, see Section 2.3.6
- Polar Vortex** Strong atmospheric eddy occurring periodically at the poles during winter time
- Regularisation** Method to smooth the retrieved profiles, see Section 4.3.2
- Residual** Spectral features that are not addressed by the retrieval fit, see Chapter 5 for some examples
- RTM** Radiative Transfer Model, see Chapter 3 for the occultation RTM
- SAGE** Stratospheric Gas and Aerosol Experiment, see Section 2.3.7
- SCIAMACHY** SCanning Imaging Absorption spectroMeter for Atmospheric CHartography, see Chapter 2
- SCIATRAN** Newer version of GOMETRAN
- Shift and Squeeze** Method to balance wavelength calibration errors, see Section 4.3.3
- Slit function** Mathematical description of the spectral resolution of a detector system, see Section 2.1.2
- SNR** Signal-to-Noise Ratio, see Section 3.4.1

SRON Space Research Organisation Netherlands

SZA Solar Zenith Angle, see Section 2.2 and Appendix D

Tangent Point/Height Closest point of the line of sight to the Earth's surface and its altitude, respectively, see Section 2.2.1

Tikhonov-Twomey See Regularisation

TOA Top of Atmosphere, geometric definition

Undersampling Undersampling occurs when the spectral resolution of a spectrometer is too small compared to the width of absorption lines.

UTC Coordinated Universal Time, useful for worldwide comparisons

UV Ultraviolet, spectral region with relatively high photon energies beyond short wave visible light

Vis Visible, short for the visible spectral range with wavelengths roughly between 400 and 800 nm

VMR Volume Mixing Ratio, common unit to quantify the amount of certain species

Weighting function First derivative of radiation intensity with respect to the trace gas concentration at a certain height layer, see Section 4.3.1

Bibliography

- B. Ahlers and M. Dobber. OPTEC5: Slit function calibration of the SCIAMACHY PFM. Technical report, TNO TPD, Netherlands, December 2000.
- L. J. Alvarez, E. Lopez, M. Sanchez, and J. A. Gonzales. ENVISAT-1 Mission CFI Software – General Software User Manual, vers. 4.6. provided by GMV/ESA, 2000.
- G. P. Anderson, S. A. Clough, F. X. Kneizys, J. H. Chetwynd, and E. P. Shettle. AFGL atmospheric constituent profiles (0–120 km). Technical Report AFGL-TR-86-0110, Phillips Laboratory, AD A 175173, 1986.
- E. Arijs, D. Nevejans, D. Fussen, P. Frederick, E. van Ransbeeck, F. W. Taylor, S. B. Calcutt, S. T. Werrett, C. L. Hepplewhite, T. M. Pritchard, I. Burchell, and C. D. Rodgers. The ORA occultation radiometer on EURECA: instrument description and preliminary results. *Advances in Space Research*, 16:33–36, 1995.
- W. Balzer, S. Slijkhuis, and M. Bollner. SCIAMACHY level 0 to 1b processing input/output data definition. Technical report, Deutsches Zentrum für Luft- und Raumfahrt e.V., Oberpfaffenhofen, 2000.
- J. L. Bertaux, G. Megie, T. Widemann, E. Chassefiere and R. Pellinen, E. Kyrölä, S. Korpela, and P. Simon. Monitoring of ozone trend by stellar occultations: The GOMOS instrument. *Advances in Space Research*, 11(3):237–242, 1991.
- K. Bogumil, J. Orphal, and J. P. Burrows. Reference spectra of atmospheric relevant trace gases measured with the SCIAMACHY PFM satellite spectrometer. In *URF Sciences Exactes et Naturelle*, BP 1039, 51687 Reims Cedex, France, 1999.
- Harmut Bösch. *Studies of the Stratospheric Nitrogen and Iodine Chemistry by Balloon-Borne DOAS Measurements and Model Calculations*. PhD thesis, Universität Heidelberg, 2002.
- Heinrich Bovensmann, John P. Burrows, Michael Buchwitz, J. Frerick, Stefan Noel, Vladimir V. Rozanov, K. V. Chance, and A. P. H. Goede. SCIAMACHY: Mission

- objectives and measurement modes. *Journal of the Atmospheric Sciences*, 56(2): 127–150, January 1999.
- Astrid Bracher. Institute of Environmental Physics, Bremen, private communication, 2003.
- Guy P. Brasseur, John J. Orlando, and Geoffrey S. Tyndall, editors. *Atmospheric Chemistry and Global Change*. Oxford University Press, Oxford, 1999.
- Francois-Marie Breon. The potential of spaceborne remote sensing to contribute to the quantification of anthropogenic emissions in the frame of the kyoto protocol. Technical report, European Space Agency, May 2003. ESA Study 15427/01/NL/MM.
- C. Brühl and P. J. Crutzen. The MPI two-dimensional atmospheric model - trace gas profiles. private communication, 1991.
- C. Brühl, S. R. Drayson, J. M. III Russell, P. J. Crutzen, J. M. McInerney, P. N. Purcell, H. Claude, H. Gernandt, T. J. McGee, T. S. McDermid, and M. R. Gunson. Halogen occultation experiment ozone channel validation. *Journal of Geophysical Research*, 101:10217–10240, 1996.
- J. P. Burrows, A. Dehn, B. Deters, S. Himmelmann, A. Richter, S. Voigt, and J. Orphal. Atmospheric remote-sensing reference data from GOME: 1. temperature-dependent absorption cross sections of NO₂ in the 231–794 nm range. *Journal of Quantitative Spectroscopy and Radiative Transfer*, 60:1025–1031, 1998.
- John P. Burrows et al. A european proposal for atmospheric remote sensing from the ESA polar platform. Max-Planck-Institut für Chemie, Mainz, Germany, 1988. Available from the Max-Planck-Institut.
- S. Chandrasekhar. *Radiative Transfer*. Dover Publications Inc., New York, 1960.
- S. Chapman. A theory of upper atmospheric ozone. *Mem. R. Meteorol. Soc.*, 3: 103–125, 1930.
- P. J. Crutzen. The influence of nitrogen oxides on the atmospheric ozone content. *Quarterly Journal of the Royal Meteorological Society*, 103:320–327, 1970.
- D. M. Cunnold, W. P. Chu, R. A. Barnes, M. P. McCormick, and R. E. Veiga. Validation of SAGE II ozone measurements. *Journal of Geophysical Research*, 94:8447–8460, 1989.
- D. M. Cunnold, J. M. Zawodny, W. P. Chu, J. P. Pommereau, F. Goutail, J. Lenoble, M. P. McCormick, R. E. Veiga, D. Murcray, N. Iwagami, K. Shibasaki, P. C. Simon, and W. Peetermans. Validation of SAGE II NO₂ measurements. *Journal of Geophysical Research*, 96(D7):12913–12925, 1991.

- Francis Dalaudier, Valery Kan, and Alexandre S. Gurvich. Chromatic refraction with global ozone monitoring by occultation of stars. i. description and scintillation correction. *Applied Optics*, 40(6):866–877, February 2001.
- Johan de Vries, Ronald van der A, and Sander Slijkhuis. Instrument simulation software, vers. 4.1. provided by SRON, Netherlands, 1997.
- D. Deirmendjian. *Electromagnetic scattering on spherical polydispersions*. American Elsevier Pub. Co., New York, 1969.
- R. DeMajistre, D. E. Anderson, S. Lloyd, P K. Swaminathan, and S. Zasadil. Effects of refraction on photochemical calculations. *Journal of Geophysical Research*, 100(D9):18817–18822, September 1995.
- Wolfgang Demtröder. *Experimentalphysik 2 – Elektrizität und Optik*. Springer Verlag, Berlin, 1995.
- Wolfgang Demtröder. *Experimentalphysik 4 – Kern-, Teilchen- und Astrophysik*. Springer Verlag, Berlin, 1998.
- B. Edlen. The refractive index of air. *Metrologia*, 2:71–80, 1966.
- Kai-Uwe Eichmann. *Ozonverteilungen der Nordhemisphäre gemessen mit GOME: Einfluss von Dynamik und Chemie in der Stratosphäre*. PhD thesis, Universität Bremen, 2001.
- H. Elbern and D. Klasen. Analysis of global synoptic chemical constituent maps by 4D variational assimilation of satellite data. SP-461, Gothenburg, 2000.
- H. Elbern and H. Schmidt. Ozone episode analysis by four-dimensional variational chemistry data assimilation. *Journal of Geophysical Research*, 106(D4):3569–3590, 2001.
- Claudia Emde. Der einfluss atmosphärischer inhomogenitäten auf satellitengelegene okkultationsmessungen. Master's thesis, Universität Bremen, 2001.
- J. C. Farman, B. G. Gardner, and J. D. Franklin. Large losses of total ozone in antarctica reveal seasonal ClO_x and NO_x interaction. *Nature*, 315:207–210, 1985.
- M. Fisher and D. J. Lary. Lagrangian four dimensional variational data assimilation of chemical species. *Quarterly Journal of The Royal Meteorological Society*, 121(527):1681–1704, October 1995.

- Didier Fussen, Etienne Arijs, Fabienne Leclere, Dennis Nevejans, and Christine Bingen. Tomography of the earth's atmosphere by the spaceborne occultation radiometer ORA: Spatial inversion algorithm. *Journal of Geophysical Research*, 102(D4):4357–4365, February 1997.
- R. R. Gamache, R. L. Hawkins, and L. S. Rothman. Total internal partition sums in the temperature range 70–3000 K: Atmospheric linear molecules. *Journal of Molecular Spectroscopy*, 142:205–219, 1990.
- Owen K. Garriott. Visual observations from space. *Journal of the Optical Society of America*, 69(8):1064–1068, August 1979.
- W. Glaccum, R. L. Lucke, R. M. Bevilacqua, E. P. Shettle, J. S. Hornstein, D. T. Chen, J. D. Lumpe, S. S. Krigman, D. J. Debrestian, M. D. Fromm, F. Dalaudier, E. Chassefiere, C. Deniel, C. E. Randall, D. W. Rusch, J. J. Olivero, C. Brogniez, J. Lenoble, and R. Kremer. The polar ozone and aerosol measurement instrument. *Journal of Geophysical Research*, 101(D9):14479–14487, June 1996.
- R. M. Goody. *Atmospheric Radiation: 1. Theoretical Basis*. Clarendon Press, Oxford, 1964.
- L. L. Gordley, J. M. III Russell, L. J. Mickley, J. E. Frederick, J. H. Park, K. A. Stone, G. M. Beaver, J. M. McInerney, L. E. Deaver, G. C. Toon, F. J. Murcray, R. D. Blatherwick, M. R. Gunson, J. P. D. Abbatt, R. L. Mauldin III, G. H. Mount, B. Sen, and J. F. Blavier. Validation of nitric oxide and nitrogen dioxide measurements made by the halogen occultation experiment for the UARS platform. *Journal of Geophysical Research*, 101(D6):10241–10266, 1996.
- J. K. Hargreaves. *The Solar-terrestrial Environment*. Cambridge University Press, Cambridge, 1992.
- D. F. Heath, A. J. Krueger, A. Roeder, and B. D. Henderson. The solar backscatter ultraviolet and total ozone mapping spectrometer (SBUV/TOMS) for nimbus g. *Optical Engineering*, 14:323–331, 1975.
- Ricarda Hoogen, Vladimir Rozanov, and John P. Burrows. Ozone profiles from GOME satellite data: Algorithm description and first validation. *Journal of Geophysical Research*, 104(D7):8263–8280, 1999.
- R. W. M. Hoogeveen, R. J. van der A, and A. P. H. Goede. Extended wavelength InGaAs infrared (1.0–2.4 mm) detector arrays on SCIAMACHY for space-based spectrometry of the earth atmosphere. *Infrared Physics and Technology*, 42: 1–16, 2001.

- H. S. Johnston. Reduction of stratospheric ozone by nitrogen oxide catalysts from supersonic transport exhaust. *Science*, 173:517–522, 1971.
- Johannes Kaiser. *Atmospheric Parameter Retrieval from UV-Visible-NIR Limb Scattering Measurements*. PhD thesis, Universität Bremen, 2001. ISBN 3-89722-830-3, Logos Verlag Berlin.
- Johannes W. Kaiser, Vladimir V. Rozanov, and John P. Burrows. Theoretical precisions for SCIAMACHY limb retrieval. *Advances in Space Research*, 29(11):1837–1842, 2002.
- L. V. King. On the complex anisotropic molecule in relation to the dispersion and scattering of light. *Proceedings of the Royal Society London*, A 104:333–357, 1923.
- F. X. Kneizys, E. P. Shettle, L. W. Abreu, J. J. Chetwynd, G. P. Anderson, W. O. Gallery, J. E. A. Selby, and S. A. Clough. Users guide to LOWTRAN 7. Technical Report AFGL-TR-88-0177, Air Force Geophysical Laboratory, Bedford, Massachusetts, 1988.
- R. L. Kurucz, I. Furenlid, J. Brault, and L. Testerman. Solar flux atlas from 296 to 1300 nm. Technical report, National Solar Observatory, New York, 1984.
- Akihiko Kuze, Makoto Suzuki, Kunio Nakamura, Jun Tanii, and Yasuhiro Sasano. Design and performance of ILAS-II echelle grating spectrometer for ClONO₂ measurement. San Diego, California, 1998. SPIE—The International Society for Optical Engineering.
- Esko Kyrö. Balloon sonde measurements over Sodankylä. Published in the NADIR database at the Norwegian Institute for Air Research (NILU), 2002.
- R. L. Lucke, D. R. Korwan, R. M. Bevilacqua, J. S. Hornstein, E. P. Shettle, D. T. Chen, M. Daehler, J. D. Lumpe, M. D. Fromm, D. Debrestian, B. Neff, M. Squire, G. König-Langlo, and J. Davies. The polar ozone and aerosol measurement (POAM) III instrument and early validation results. *Journal of Geophysical Research*, 104(D15):18785–18799, August 1999.
- J. D. Lumpe, R. M. Bevilacqua, K. W. Hoppel, S.S. Krigman, D.L. Kriebel, D. J. Debrestian, C. E. Randall, D.W. Rusch, C. Brogniez, R. Ramanathan, E. P. Shettle, J. J. Olivero, J. Lenoble, and P. Pruvost. POAM II retrieval algorithm and error analysis. *Journal of Geophysical Research*, 102(D19):23593–23614, October 1997.
- Michael Lutomsky. Einfluss atmosphärischer brechungseffekte auf die messung der sonnenstrahlung in okkultationsgeometrie mit dem satellitengestützten spektrometer SCIAMACHY. Master's thesis, Universität Bremen, 2002.

- P. Lützow-Wentzky and D. Demuth. Measurement data definition and format description for SCIAMACHY. Technical report, Astrium GmbH, Friedrichshafen, Germany, 2001.
- L. E. Mauldin, N. H. Zaun, M. P. McCormick, J. J. Guy, and W. R. Vaughn. Stratospheric aerosol and gas experiment II instrument: A functional description. *Optical Engineering*, pages 24–307, 1985.
- M. P. McCormick et al. SAGE III algorithm theoretical basis document: Solar and lunar algorithm, 2002. LaRC 475-00-108, Version 2.1.
- M. P. McCormick, P. Hamill, T. J. Pepin, W. P. Chu, T. J. Swissler, and L. R. McMaster. Satellite studies of the stratospheric aerosol. *Bulletin of the American Meteorological Society*, 60:1038–1046, 1979.
- J. Meyer, A. C. Schlesier, A. Rozanov, H. Bovensmann, and J. P. Burrows. Towards O₃ and NO₂ vertical profile retrieval from SCIAMACHY solar occultation measurements: First results. *Advances in Space Research*, 34:744–748, 2004.
- G. Mie. Beiträge zur Optik trüber Medien, speziell kolloidaler Metallösungen. *Annalen der Physik*, 25:377–445, 1908.
- NASA. U.S. standard atmosphere supplements. Technical report, U.S. Government Printing, Washington, D.C., 1976.
- Heinz Neckel and Dietrich Labs. Variations of 'wavelengths' and 'bisector indices' of 70 solar spectral lines between 33000 and 3960 Å in kitt peak FTS spectra. *Solar Physics*, 126:207–266, 1990.
- Stefan Noel. Institute of Environmental Physics, Bremen, private communication, 2003.
- C. E. Randall, J. D. Lumpe, R. M. Bevilacqua, K. W. Hoppel, E. P. Shettle, D. W. Rusch, L. L. Gordley, K. Kreher, K. Pfeilsticker, H. Boesch, G. Toon, F. Goutail, and J.-P. Pommereau. Validation of polar ozone and aerosol measurements (POAM) III NO₂ measurements. *Journal of Geophysical Research*, 107:4432, 2002.
- C. E. Randall, D. W. Rusch, R. M. Bevilacqua, K. W. Hoppel, J. D. Lumpe, E. Shettle, E. Thompson, L. Deaver, J. Zawodny, et al. Validation of POAM III ozone: Comparisons with ozonesonde and satellite data. *Journal of Geophysical Research*, June 2003.
- Andreas Richter. *Absorptionsspektroskopische Messungen stratosphärischer Spurengase über Bremen, 53° N*. PhD thesis, Universität Bremen, 1997. ISBN 3-89712-058-5, Cuvillier Verlag Göttingen.

- Günther La Roche. *Solargeneratoren für die Raumfahrt*. Vieweg Verlag, Braunschweig, Germany, 1997.
- Clive D. Rodgers. Retrieval of atmospheric temperature and composition from remote measurements of thermal radiation. *Reviews of Geophysics and Space Physics*, 4:609–624, 1976.
- Clive D. Rodgers. Characterization and error analysis of profiles retrieved from remote sounding measurements. *Journal of Geophysical Research*, pages 5587–5595, 1990.
- Clive D. Rodgers. *Inverse Methods for Atmospheric Sounding: Theory and Practice*. World Scientific, Singapore, 1999.
- L. S. Rothman, A. Barbe, D. Chris Benner, et al. The HITRAN molecular spectroscopic database and HAWKS (HITRAN atmospheric workstation). *Journal of Quantitative Spectroscopy and Radiative Transfer*, 60(5):665–710, 1998.
- Alexei Rozanov. *Modeling of the radiative transfer through a spherical planetary atmosphere: Application to the atmospheric trace gases retrieval from occultation- and limb-measurements in UV-Vis-NIR*. PhD thesis, Universität Bremen, 2001. ISBN 3-8325-0138-X, Logos Verlag Berlin.
- Alexei Rozanov, Vladimir Rozanov, and John P. Burrows. A numerical radiative transfer model for a spherical planetary atmosphere: Combined differential-integral approach involving the picard iterative approximation. *Journal of Quantitative Spectroscopy and Radiative Transfer*, 69:491–512, 2001.
- Alexei Rozanov, Vladimir V. Rozanov, and John P. Burrows. Combined differential-integral approach for the radiation field computation in a spherical shell atmosphere: Non-limb geometry. *Journal of Geophysical Research*, 105 (D18):22937–22942, September 2000.
- Vladimir V. Rozanov, Michael Buchwitz, Kai-Uwe Eichmann, Rüdiger de Beek, and John P. Burrows. SCIATRAN - a new radiative transfer model for geophysical applications in the 240–2400 nm spectral region: The pseudo-spherical version. *Advances in Space Research*, 29(11):1831–1835, 2002.
- Vladimir V. Rozanov, D. Diebel, R. J. D. Spurr, and J. P. Burrows. GOMETRAN: A radiative transfer model for the satellite project GOME, the plane-parallel version. *Journal of Geophysical Research*, 102(16):16683–16695, 1997.
- Georgii Vladimirovich Rozenberg. *Twilight: A Study in Atmospheric Optics*. Plenum Press, New York, 1966.

- J. M. Russel, L. L. Gordley, Jae H. Park, S. R. Drayson, W. D. Hesketh, R. J. Cicerone, A. F. Tuck, J. E. Frederick, J. E. Harries, and P. J. Crutzen. The halogen occultation experiment. *Journal of Geophysical Research*, 98(D6):10777–10797, June 1993.
- Yasuhiro Sasano, Makoto Suzuki, Tatsuya Yokota, and Hiroshi Kanzawa. Improved limb atmospheric spectrometer (ILAS) project: ILAS instrument, performance and validation plan. Paris, France, 1995. Europt Series.
- Anke Schlesier. Institute of Environmental Physics, Bremen, private communication, 2002.
- John H. Seinfeld and Spyros N. Pandis. *Atmospheric Chemistry and Physics*. John Wiley & Sons, Inc., New York, 1998.
- C. E. Shannon. *The mathematical theory of communication*. University of Illinois Press, Urbana, 1949.
- B.-M. Sinnhuber, R. Müller, H. Bovensmann, V. Eyring, U. Klein, J. Langer, J. Trentmann, J. Burrows, and K. Künzi. Interpretation of mid-stratospheric arctic ozone measurements using a photochemical box-model. *Journal of Atmospheric Chemistry*, 34:281–290, 1999.
- Christopher E. Sioris, Craig S. Haley, Chris A. McLinden, Christian von Savigny, Ian C. McDade, Wayne F. J. Evans, Jack C. McConnell, and Edward J. Llewellyn. Stratospheric profiles of nitrogen dioxide observed by OSIRIS on the odin satellite. *Journal of Geophysical Research*, 108(D7):4215, 2003.
- Jochen Skupin. Institute of Environmental Physics, Bremen, private communication, 2003.
- S. Slijkhuis and W. Balzer. Envisat-1 – SCIAMACHY level 0 to 1c processing – algorithm theoretical basis document. Technical report, Deutsches Zentrum für Luft- und Raumfahrt e.V., Oberpfaffenhofen, 2000.
- S. Slijkhuis, W. Balzer, and M. Bollner. SCIAMACHY – level 0 to 1b processing – detailed processing model/parameter data list. Technical report, Deutsches Zentrum für Luft- und Raumfahrt e.V., Oberpfaffenhofen, 1997.
- Susan Solomon. Stratospheric ozone depletion: A review of concepts and history. *Reviews of Geophysics*, 37(3):275–316, August 1999.
- Philip T. Spickler, D. Chris Benner, and James M. Russell. Solar center-to-limb infrared intensity from the halogen occultation experiment. *Solar Physics*, 165: 23–39, 1996.

- Gabrielle Stiller. IMK Forschungszentrum, Karlsruhe, private communication, 2003.
- Michael E. Thomas and Richard I. Joseph. Astronomical refraction. *Johns Hopkins Apl Technical Digest*, 17(3):279–284, 1996.
- A.-N. Tikhonov. On the solution of incorrectly stated problems and a method of regularization. *Dokl Acad. Nauk SSSR*, 151(501), 1963.
- Jörg Trentmann. Entwicklung eines photochemischen Atmosphärenmodells. Master's thesis, Universität Bremen, 1997.
- S. Twomey. On the numerical solution of fredholm integral equation of the first kind by the inversion of the linear system produced by quadrature. *J. Ass. Comput. Mach.*, 10(97), 1963.
- G. J. R. M. J. van Rie. Solar calibration of earth observation instruments in general and applied to SCIAMACHY. Technical report, Delft University of Technology, Netherlands, 1995.
- H. Visser. SCIAMACHY: Impact of non-uniform intensity across the slit on spectral shift in limb observations, 2002. Internal report.
- C. von Savigny, A. Kokhanovsky, H. Bovensmann, K.-U. Eichmann, J. Kaiser, S. Noel, A. V. Rozanov, J. Skupin, and J. P. Burrows. NLC detection and particle size determination: First results from SCIAMACHY on ENVISAT. *Advances in Space Research, revised*, 2003.
- Christian von Savigny, Alexei Rozanov, Heinrich Bovensmann, and John P. Burrows. Semi-quantitative estimate of spectral shifts in SCIAMACHY limb observations, 2002. Internal Report.
- Marco Vountas. *Die Modellierung und Parametrisierung des Ring Effektes*. PhD thesis, Universität Bremen, 1998. ISBN 3-8265-4649-0, Shaker Verlag Aachen.
- A. Vuorilehto and S. Korpela. Study of the sun and moon as radiation calibration targets. Technical report, Space Systems Finland Ltd., Espoo, Finland, 1994.
- I. Walkty, W. Eliuk, B. Whitehead, J. Peterson, T. Doherty, G. Rumbold, and R. Shelly. SCISAT-1 ACE mission. Nov 7–9 2000.
- A. M. Yaglom and I. M. Yaglom. *Probability and information*. Reidel, Dordrecht, 1983.